

DISSERTATION

REGULATION OF ACTIN CAPPING PROTEIN  
DURING CLATHRIN-MEDIATED ENDOCYTOSIS

Submitted by

Andrew Lamb

Department of Biochemistry and Molecular Biology

In partial fulfillment of the requirements

For the Degree of Doctor of Philosophy

Colorado State University

Fort Collins, Colorado

Fall 2022

Doctoral Committee:

Advisor: Santiago Di Pietro

Diego Krapf  
Steven Markus  
Olve Peersen

Copyright by Andrew K. Lamb 2022

All Rights Reserved

## ABSTRACT

### REGULATION OF ACTIN CAPPING PROTEIN DURING CLATHRIN-MEDIATED ENDOCYTOSIS

Clathrin-mediated endocytosis (CME) is a major endocytic pathway that is essential in all eukaryotic cells. In the budding yeast *S. cerevisiae*, polymerization of actin into a branched network is critical to provide the force necessary for membrane invagination during CME. Polymerization of this branched actin network is a highly regulated process, reliant on a multitude of endocytic factors for proper formation. A key regulator is actin capping protein (CP), which binds to the barbed end of actin filaments with high affinity to prevent the loss or addition of actin subunits. While regulation of CP by proteins containing a capping protein-interacting (CPI) motif has been demonstrated in higher eukaryotes, it has not been described in yeast or during endocytosis. Here, we identify and dissect the roles of three CPI motif-containing endocytic factors, Aim21, Bsp1 and Twf1, in CP regulation. Aim21 was the first CPI motif we identified, and the first CPI motif described in yeast. Together with its binding partner Tda2, Aim21 binds to CP through its CPI motif with nanomolar affinity. We demonstrate that Tda2 functions as a dimerization engine for Aim21, bringing two molecules of Aim21 together to form a hetero-tetrameric complex that we term the Tda2-Aim21 complex. Formation of the Tda2-Aim21 complex is essential for a strong interaction with CP, as Aim21 alone binds to CP with more than a 10 fold weaker affinity. Mutating the CPI motif of Aim21 in the yeast genome leads to a recruitment defect in CP and an over-accumulation of F-actin at CME sites, suggesting Aim21 aids in the recruitment of CP to endocytic sites. The little-studied endocytic factor, Bsp1, displays the same phenotype when its CPI motif is mutated in yeast. In addition, the Bsp1 and Aim21 CPI motifs allosterically inhibit the capping function of CP during *in vitro* actin polymerization assays. When mutations to both the Aim21 and Bsp1 CPI motifs are combined in

yeast, CP localization to CME sites is severely reduced, demonstrating that Aim21 and Bsp1 have redundant functions during yeast CME in recruiting a transiently active CP to cortical actin patches. In contrast, the well-conserved actin disassembly factor, twinfilin (Twf1), is not important for recruitment of CP, but is itself reliant on its interaction with CP to localize to CME sites. While the CPI motifs of Aim21 and Bsp1 inhibit the capping function of CP, the Twf1 CPI motif has no effect, despite binding to CP with nanomolar affinity. Mutation of the Twf1 CPI motif results in an accumulation of CP and F-actin at endocytic sites, suggesting that it functions downstream of CP recruitment to recycle CP and actin network components. Together, these findings shed light on how CPI motifs regulate CP in a step-wise manner during yeast endocytosis.

## TABLE OF CONTENTS

ABSTRACT .....	ii
LIST OF TABLES .....	v
LIST OF FIGURES .....	vi
CHAPTER 1: INTRODUCTION .....	1
1.1 Clathrin-mediated Endocytosis .....	1
1.2 Actin Polymerization During Clathrin-mediated Endocytosis .....	7
1.3 Actin Capping Protein .....	18
1.4 Overview of Dissertation .....	27
CHAPTER 2: TDA2 FUNCTIONS AS A DIMERIZATION ENGINE FOR AIM21 TO REGULATE ACTIN CAPPING PROTEIN DURING CME .....	28
2.1 Summary .....	28
2.2 Introduction .....	29
2.3 Results .....	31
2.4 Discussion .....	61
2.5 Materials and Methods .....	67
CHAPTER 3: CPI MOTIFS REGULATE ACTIN CAPPING PROTEIN DURING YEAST ENDOCYTOSIS .....	74
3.1 Summary .....	74
3.2 Introduction .....	74
3.3 Results .....	77
3.4 Discussion .....	109
3.5 Materials and Methods .....	110
REFERENCES .....	116

## LIST OF TABLES

Table 1.1.....	10
----------------	----

## LIST OF FIGURES

Figure 1.1.....	4
Figure 1.2.....	17
Figure 1.3.....	20
Figure 2.1.....	32
Figure 2.2.....	34
Figure 2.3.....	36
Figure 2.4.....	38
Figure 2.5.....	41
Figure 2.6.....	42
Figure 2.7.....	43
Figure 2.8.....	45
Figure 2.9.....	48
Figure 2.10.....	51
Figure 2.11.....	52
Figure 2.12.....	55
Figure 2.13.....	58
Figure 2.14.....	60
Figure 2.15.....	63
Figure 3.1.....	79
Figure 3.2.....	81
Figure 3.3.....	84
Figure 3.4.....	87
Figure 3.5.....	90
Figure 3.6.....	91
Figure 3.7.....	94
Figure 3.8.....	98
Figure 3.9.....	100
Figure 3.10.....	103
Figure 3.11.....	105
Figure 3.12.....	107

# CHAPTER 1

## INTRODUCTION

### 1.1 Clathrin-mediated Endocytosis

#### 1.1.1 *Membrane Trafficking and endocytosis*

Membranes, consisting of a mixture of lipids and proteins, allow for compartmentalization within a cell. At the cell periphery, the plasma membrane provides a barrier between the extracellular environment and the cytoplasm within the cell. In the cytoplasm, membrane-enclosed compartments, or organelles, allow for regions with a distinct chemistry from the surrounding cytosol. The presence of organelles is a defining characteristic of eukaryotic cells and allows for functionally distinct regions within the cell. Membranes are defined by the types of lipids they are composed of, and the proteins embedded within them. A prevailing characteristic of membranes is that they are dynamic, changing in both lipid and protein composition in response to the needs of a cell. To bring about these changes, the cell utilizes membrane trafficking pathways.

Membrane trafficking can be divided into two basic pathways, the secretory pathway, and the endocytic pathway. The secretory pathway begins at the endoplasmic reticulum (ER), the organelle where lipid synthesis occurs and where newly translated membrane proteins reside, and leads outwards toward the Golgi apparatus and plasma membrane. The ultimate step of the secretory pathway is exocytosis, the process by which a secretory vesicle, or exosome, fuses with the plasma membrane, releasing its content into the extracellular space. Countering the secretory pathway is the endocytic pathway. Endocytosis, the first step in the endocytic pathway, is the process by which a portion of the plasma membrane is invaginated and pinched off as a vesicle, or endosome, inside of the cell. Following endocytosis, endosome content is trafficked inward through the endocytic pathway, ultimately ending in degradation of

the content in the lysosome, or escaping this fate and being recycled back to the plasma membrane.

While there are numerous forms of endocytosis, the best studied form is clathrin-mediated endocytosis (CME). CME is essential in all eukaryotic cells and is a main endocytic pathway for endocytosis of transmembrane receptors. It is critical for processes such as nutrient uptake, cell signaling and remodeling of the plasma membrane. In total there are nearly 60 proteins, or endocytic factors, that work to collect cargo along the plasma membrane, invaginate the surrounding membrane and pinch off the invagination as a vesicle within the cell. While the function of many endocytic factors is known, there remain many factors whose function has not yet been elucidated. In the Di Pietro lab, we are primarily concerned with discovering how endocytic factors are functioning at the molecular level.

### 1.1.2 CME protein machinery

In the 1960s, electron microscopy images of mosquito oocytes depicted protein-rich invaginations, or pits, along the inner leaflet of the oocyte plasma membrane [1]. In addition, proteinaceous coats were seen on vesicles within the oocytes. Nearly 10 years later, these basket-like proteinaceous coats were shown to be largely constructed from a major protein constituent, later termed clathrin [2]. The namesake of CME, clathrin was subsequently shown to be capable of polymerizing into a cage-like structure of characteristic pentagonal and hexagonal polymers [3]. These findings among others, led to the theory that polymerization of clathrin into a cage-like structure drove membrane invagination during a process what would ultimately be termed clathrin-mediated endocytosis.

Since these early findings, much of the research on CME has shifted to utilizing the budding yeast, *saccharomyces cerevisiae*, as a model system. In combination with advances in microscopic techniques such as live-cell imaging, the tractability of yeast genetics has allowed for an accelerated rate of CME-related discoveries in an *in vivo* system. Numerous genetic

screens in yeast have been utilized to identify novel endocytic factors [4-7]. In addition to clathrin, nearly 60 endocytic factors have been demonstrated to directly participate in yeast CME. The majority of these factors are conserved from yeast to mammals, and have conserved functions. Live-cell fluorescence microscopy has demonstrated that these proteins assemble dynamically at punctate endocytic sites, or endocytic patches, in a highly choreographed temporal manner [8]. This highly organized nature of protein recruitment has allowed endocytic factors to be broken into phases, or modules, based on when they are recruited to endocytic sites [9]. These modules, and examples of the endocytic factors that function during them, are depicted in **Figure 1.1**, and described in brief below.

During the initial phase of endocytosis, the coat module assembles at the plasma membrane. This module consists of coat proteins, such as the aforementioned clathrin, as well as adaptor proteins, which provide a link between transmembrane cargo proteins and coat proteins. While the subsequent steps are remarkably reproducible in length, this initial phase of CME can be variable in time, lasting between 60 and 120s [10]. Given the variable length of this phase, proteins of the coat module are often divided into early, middle and late coat proteins based on their time of arrival at endocytic patches. A defining characteristic of this phase is that the membrane is immobile and does not invaginate during assembly of coat module proteins. This immobile phase is initiated by adaptor proteins binding to sorting signals on the cytosolic side of transmembrane cargo proteins. The sorting signals are typically short peptide motifs or a region covalently bound to ubiquitin [11]. Adaptors, in turn, aid in the recruitment of additional early coat proteins, including clathrin. Many of these early coat proteins act as scaffold proteins, allowing for interaction and recruitment of additional coat proteins, including middle and late coat proteins [12, 13]. This period between early coat protein arrival and the arrival of late coat proteins is often referred to as “maturation” of the endocytic coat.

While clathrin is the namesake of CME, yeast CME is reliant on polymerization of actin to drive membrane invagination [14]. When yeast cells are treated with latrunculin A, a G-actin

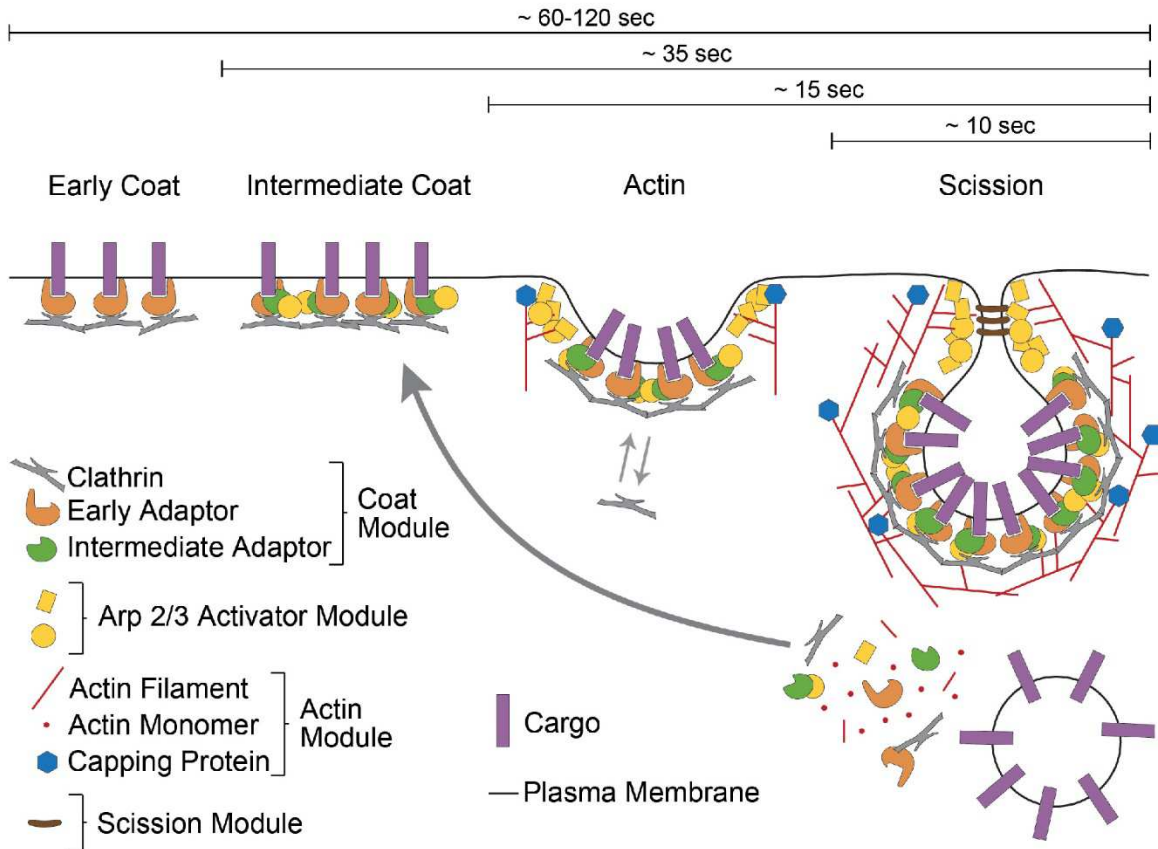


**Figure 1.1: Clathrin-mediated endocytosis machinery modules.** Proteins of the coat module arrive first at the CME site, in a phase of CME with a variable lifetime. Coat proteins include adaptor proteins, clathrin and scaffolding proteins. Factors of the Arp2/3 activation module arrive coincident with intermediate coat proteins, and reside at CME sites for ~35 seconds. Actin polymerization is initiated by the Arp2/3 activation module upon arrival of the Arp2/3 complex and actin regulators, and actin polymerization ensues for ~15 seconds, driving membrane invagination. Proteins of the scission module arrive last, working to pinch off the invagination as a vesicle inside of the cell. Following vesicle formation, endocytic proteins are recycled for further use at alternate endocytic sites.

sequestering agent, membrane invagination fails to occur, and endocytosis is stalled [8]. In particular, a branched actin network, nucleated by the Arp2/3 complex, provides the force necessary for membrane invagination [15]. The seven subunit Arp2/3 complex binds to the side of an existing actin filaments at a characteristic 70° angle to nucleate a new filament. However, for full activity, the Arp2/3 complex must also interact with a cofactor called a nucleation promoting factor (NPF). Prior to the arrival of the Arp2/3 complex and the onset of actin polymerization, major regulators of the Arp2/3 complex are recruited to endocytic patches ~20 seconds prior to the onset of actin polymerization. The major protein of this Arp2/3 activator module is Las17, the yeast homolog of Wiskott-Aldrich syndrome protein (WASP), the most potent activator of the Arp2/3 complex [16]. As actin polymerization has yet to occur, the membrane remains immobile.

Following the recruitment of the Arp2/3 activators, the actin module proteins, consisting of over 30 actin regulatory proteins, arrive at the endocytic patch. These proteins work together to nucleate a dense meshwork of short actin filaments, and subsequently turnover the network following membrane invagination and scission. This burst of actin polymerization is coincident with a change from an immobile membrane to a mobile, invaginating membrane. Proteins of the actin module have a highly reproducible recruitment pattern, residing at the plasma membrane for all of ~20 seconds. The proteins involved in the actin module will be discussed at greater depth in section 1.3 of this introductory chapter.

Shortly after actin-driven invagination of the plasma membrane, the resulting tubular invagination must be pinched off by scission module proteins to form a vesicle inside of the cell. This is accomplished primarily through the amphiphysins, Rvs161 and Rvs167, as well as the GTPase dynamin homolog Vps1. The amphiphysins function as heterodimers and contain BAR domains which facilitate interaction with curved membranes at the neck of the invagination [17-19]. The amphiphysins are thought to hold the tubule shape of the membrane as actin polymerization drives the membrane invagination. Knocking out either Rvs161 or Rvs167 from

yeast cells results in aberrant patch behavior, including retraction phenotypes where an invagination is unproductive [9, 20]. While the phenotype seen in Vps1-null cells is mild compared with amphiphysin-null cells, it has nevertheless been shown to be important for productive CME [20, 21].

In total, the process of CME takes between 60-120 seconds and results in a vesicle of ~50 nm in diameter [22]. Following scission of the invagination, a coated endosome, with endocytic coat proteins still bound from the initial phases of endocytosis, is present. To allow the endosome to be trafficked further along the endocytic pathway and recycle the coat proteins for use in additional rounds of CME, the endosome must be uncoated. This process is largely accomplished through phosphorylation of coat proteins [23]. The conserved kinases Prk1 and Ark1 are critical for this process, and largely redundant in function [24-26]. They function through phosphorylation of coat proteins, which disrupt the interactions between coat proteins. Conversely, synaptojanins, which are lipid phosphatases, work to disrupt the interaction between coat proteins and the plasma membrane [27, 28]. For the recycling of clathrin, the auxilin-like protein Swa2 are of particular importance [29]. Following uncoating, the endosome is free to fuse with an early endosome and continue down the endocytic pathway.

### 1.1.3 CME: yeast vs. mammals

While *S. cerevisiae* has become a powerful model for the study of CME largely due to the similarities it holds with mammalian CME, there are some key differences that should be noted. One key difference is the relative importance of actin polymerization during CME. In yeast, actin polymerization is necessary for membrane invagination to occur [8, 14, 15]. In part, the high turgor pressure in yeast due to the presence of a cell wall that pushes outward on the plasma membrane is believed to necessitate the high-force producing polymerization of actin to drive membrane invagination [30, 31]. However, in mammalian cells the link between actin and CME has been far more controversial. While early findings pointed to actin having a minimal roll in

mammalian CME, that narrative is beginning to shift. Numerous studies have demonstrated the assembly of actin at CME sites in mammalian cells [32-34]. More recently, actin has been shown to play a role in mammalian CME at structures termed “clathrin plaques”, a subset of CME sites present in certain mammalian cell types that are larger than traditional CME sites [35]. Similarly, while clathrin has been shown to be vital for mammalian CME, it is not essential for CME in yeast. In mammalian cells, depletion of clathrin leads to a complete arrest in CME [36, 37]. In yeast cells, clathrin-null cells still have productive CME, although the efficiency is reduced [9, 38]. The current view is that in yeast, clathrin plays more of an organizational role as a scaffold protein, while in mammalian cells, clathrin is playing a larger structural roll in formation of the invagination.

## **1.2 Actin Polymerization During Clathrin-mediated Endocytosis**

### *1.2.1 Actin networks in yeast*

Actin is a well-conserved ~42 kDa protein that exists in monomeric (G-actin) or filamentous (F-actin) form. Its capable of binding to either ATP or ADP, thus being present in a “T” or “D” state. While multiple isoforms of actin exist in mammalian cells, *S. cerevisiae* has a single essential gene, *ACT1*, which encodes actin [39]. G-actin polymerizes into a polarized, double-helical filament, with a fast-growing barbed (plus) end and a slow-growing pointed (minus) end. Upon polymerization of G-actin into a filament, ATP-bound actin is hydrolyzed into an ADP-bound state, resulting in newer F-actin being enriched in ATP and older filaments being enriched in ADP. Polymerization of actin networks are critical for processes including cell motility, cell structure, cellular transport and cytokinesis. While each structure consists of a network of F-actin at its core, the structure of these networks varies greatly due to the many regulatory proteins that aid in their construction.

In budding yeast there are three types of F-actin structures: (1) cortical actin patches, (2) actin cables and (3) actin rings. Cortical actin patches have been well established as sites of CME. These networks are characterized by a dense meshwork of interconnected filaments that form along the inner leaflet of the plasma membrane. Actin cables are series of linear actin filaments that are created with the help of formins. These cable systems stretch from the bud neck of yeast out to the periphery of the cell, and are critical for polarized cell growth and transport of organelles [40]. Lastly, actin filaments polymerize into the actin component of the contractile actomyosin ring just prior to cytokinesis. While cortical actin patches and actin cables are present throughout the lifetime of a cell, actomyosin rings are present only for a short period just prior to and through cytokinesis [41]. The architecture of the actomyosin ring is still being resolved, but initial findings suggest it shares more similarities with the linear actin filaments of actin cables [42]. While all three actin structures are functionally and architecturally distinct, they are all dynamic. Treatment of yeast cells with Latrunculin A, a G-actin sequestering agent, leads to the rapid loss of each actin structure [42, 43].

Cortical actin patches are synonymous with endocytic sites that are in the mobile, actin polymerization phase. At each site, nearly 5000 actin monomers and 100 molecules of the Arp2/3 complex are arranged dynamically into a meshwork of short actin filaments [44]. The resulting filaments average ~50 nm in length and consist of only 20 actin subunits [45]. Cortical actin patches are comprised of nearly 30 proteins that arrive within 5-10 seconds of each other. Together these factors work to (1) nucleate new actin filaments, (2) cap the growing end of filaments, (3) crosslink filaments to provide network rigidity and (4) disassemble the resulting actin network. While the architecture of the network is still a subject of debate, most findings suggest cortical actin patches form a similar architecture to lamellipodia at the leading edge of mammalian cells, with polymerization of new filaments targeted towards the plasma membrane [46, 47]. The vast majority of the proteins involved in formation of the cortical actin patch have well-conserved functional homologs in humans, allowing for inference of function from species-

to-species [48, 49]. The major proteins that are involved in each of these processes are described in the sections below. A full list of the endocytic factors that are involved in the actin polymerization phase of CME are listed in **Table 1.1**. While some of these proteins fit neatly into a specific functional category, many contain multiple domains that impart multiple functions.

### *1.2.2 Actin filament nucleation: The Arp2/3 complex and NPFs*

Nucleation of an actin filament refers to the process of forming a nucleus, or seed filament, from which an actin filament can elongate. This is the rate limiting step of actin polymerization. As actin dimers and trimers are unstable, they require cofactors, or nucleators to help form actin seeds from which actin filaments can grow [50]. There are two types of actin nucleators in yeast cells: (1) Formins, which nucleate the linear actin filaments of actin cables and the actomyosin ring and (2) the Arp2/3 complex which nucleates branched actin filaments. The Arp2/3 complex is a seven-subunit protein complex that is well conserved from yeast to mammals [51]. This complex binds to the side of an existing filament, or mother filament, at a characteristic 70° angle to create a seed for polymerization of a daughter filament [52]. Each subunit of the Arp2/3 complex is critical for proper CME [53]. While it consists of seven subunits, the Arp2/3 complex derives its name from two of its subunits, Arp2 and Arp3. Prior to binding an actin filament, the Arp2 and Arp3 subunits remain separated from each other in an open register [54]. On its own, this structure acts only weakly as a nucleator and is poor at providing a stable platform for elongation of an actin filament [55]. In addition to binding to a mother filament, the Arp2/3 complex must also interact with a nucleation promoting factor for full activation.

Nucleation promoting factors (NPFs) are cofactors that bind to and activate the Arp2/3 complex. In addition to binding the Arp2/3 complex, NPFs bind to actin. The strength of the NPF depends on whether the NPF interacts with G- or F-actin. Class I NPFs bind G-Actin and have a strong NPF activity, while class II NPFs bind F-actin and have a comparatively weak NPF activity. In total, 5 NPFs have been described in yeast: Las17, Myo3, Myo5, Pan1 and Abp1.

**Table 1.1:** Proteins directly involved in actin network polymerization during CME. This list was adapted from [48]. Proteins with N/A listed have no/undetermined homolog.

<b>Endocytic Stage (Lifetime)</b>	<b>Yeast Protein</b>	<b>Mammalian Homolog</b>	<b>Actin-based Functions</b>
Intermediate Coat (~40 s)	Sla2	Hip1R, Hip1	Links actin cytoskeleton to membrane
Late Coat (~35 s)	Lsb3	SH3YL1a	Actin bundling, paralog of Ysc84, binds Las17
Late Coat (~35 s)	Pan1	Intersectin	Arp2/3 NPF
Late Coat (~35 s)	Sla1	CIN85	Inhibits Las17 NPF activity
Late Coat (~35 s)	Ysc84	SH3YL1a	Actin bundling, paralog of Lsb3, binds Las17
WASP/MYO (15-35 s)	Bbc1	N/A	Inhibits Las17, interacts with Myo3/5, Aim21
WASP/MYO (15-35 s)	Bzz1	Syndapin	Relieves Sla1 inhibition of Las17
WASP/MYO (15-35 s)	Las17	WASP/N-WASP	Strongest Arp2/3 NPF
WASP/MYO (15-35 s)	Myo3	Type I Myosin	Arp2/3 NPF, paralog of Myo5, interacts with Vrp1
WASP/MYO (15-35 s)	Myo5	Type I Myosin	Arp2/3 NPF, paralog of Myo3, interacts with Vrp1
WASP/MYO (15-35 s)	Vrp1	WIP	Interacts with Myp3/5, together promote actin nucleation
Actin (15-20 s)	Abp1	ABP1	Arp2/3 NPF, binds F-actin through ADH-H domain, numerous interactors
Actin (15-20 s)	Abp140	N/A	Actin bundling protein

Actin (15-20 s)	Act1	Actin	Actin monomer
Actin (15-20 s)	Aim3	N/A	Inhibits barbed end elongation with Abp1
Actin (15-20 s)	Aim21	N/A	Forms complex with Tda2, interacts with CP
Actin (15-20 s)	Aip1	AIP1/WDR	Binds Cof1 and Srv2, implicated in barbed end capping
Actin (15-20 s)	Arp2/3,Arc15 /18/19/35/40	Arp2/3 complex	Branched actin filament nucleator
Actin (15-20 s)	Bsp1	N/A	Localizes to cortical actin patches
Actin (15-20 s)	Cap1	Alpha subunit CP	Alpha subunit of CP, caps actin filaments, interacts with Twf1, Aim21
Actin (15-20 s)	Cap2	Beta subunit CP	Alpha subunit of CP, caps actin filaments, interacts with Twf1, Aim21
Actin (15-20 s)	Cof1	Cofilin	Actin filament severing protein, binds G- and F-actin
Actin (15-20 s)	Crn1	Coronin	Arp2/3 complex regulator
Actin (15-20 s)	Gmf1	GMF	Binds to Arp2/3, filament debrancher
Actin (15-20 s)	Lsb1	SH3D19	Inhibitor of Las17, paralog of Pin3
Actin (15-20 s)	Pfy1	Profilin	Binds Actin
Actin (15-20 s)	Pin3	GRB2	Inhibitor of Las17, paralog of Lsb1
Actin (15-20 s)	Sac6	Fimbrin	Actin bundling/crosslinking protein

Actin (15-20 s)	Scp1	Transgelin	Actin bundling/crosslinking protein, binds Abp1
Actin (15-20 s)	Srv2	CAP	Catalyzes cofilin-mediated filament severing, recycles ADP-actin monomers
Actin (15-20 s)	Tda2	N/A	Forms complex with Aim21, complex interacts with CP
Actin (15-20 s)	Twf1	Twinfilin	Actin depolymerization factor, binds Srv2 and CP

Las17, the yeast homolog of Wiskott-Aldrich syndrome protein (WASP) and a class I NPF, is the strongest activator of Arp2/3 [16]. It functions by binding to the Arp2/3 complex and inducing a conformational change, shifting the Arp2 and Arp3 subunits into a closed register that simulates a free actin filament barbed end [56, 57]. In addition, Las17 funnels G-actin monomers to the actin seed through its G-actin binding domains, further stabilizing the seed filament [58, 59]. Myo3 and Myo5 are unconventional, single-headed type I myosins with largely redundant functions. With their binding partner Vrp1, which binds to G-actin, they function as class I NPFs [16]. Both the motor activity and NPF activity are important for the function of the type I myosins during CME [16]. Mutations affecting the NPF activity of either myosin are synthetic lethal with equivalent Las17 mutations, showing that class I NPF activity is essential in cells [60, 61]. While the class II NPFs, Pan1 and Abp1, have NPF activity *in vitro*, the importance of this function *in vivo* is not well understood.

### 1.2.3 Actin capping proteins

Following activation of the Arp2/3 complex by NPFs, actin seeds are primed for polymerization. To prevent polymerization of long, unproductive actin filaments that exhaust the cellular pool of G-actin, capping of actin filaments at the growing barbed end is necessary. In addition, capping of filaments is thought to play a role in regulating the average length of filaments, thus maintaining the dense architecture of the branched network. The main player in this process is the heterodimeric actin capping protein (CP), which consists of a Cap1 and a Cap2 subunit that caps barbed ends of F-actin with nanomolar affinity [62]. While deletion of either Cap1 or Cap2 results in a phenotype in-line with an overgrowth of the CME actin network, the phenotype is mild, suggesting that there may be additional factors that participate in filament capping [63]. Indeed, more recent work has demonstrated that the disassembly factors Aip1 and Cof1 block barbed end growth [64]. Additionally, a complex of the endocytic factors Aim3 and Abp1 has been shown to cap barbed ends *in vitro*, albeit not as strongly as CP, and shows

synthetic defects with CP [65]. This study along with a study in fission yeast have suggested that different capping proteins may function at different locations along the invaginating membrane, with CP working closer to the membrane where new, ATP-rich actin filaments are being polymerized and Aip1-Cof1 functioning further into the invagination, where filaments are enriched in ADP [65, 66].

#### *1.2.4 Actin crosslinking proteins*

Actin crosslinking proteins contain multiple F-actin binding domains that can bundle together multiple actin filaments. Crosslinking proteins are important for providing rigidity to the actin network, which is necessary for properly transmitting force to the plasma membrane [67]. Defective crosslinking leads to less efficient CME, which subsequently reduces the available pool of polymerizable G-actin, further impairing CME [67]. While multiple crosslinking proteins have been described, the best studied is Sac6, the yeast homolog of fimbrin. Interestingly, Sac6 displays synthetic lethality with either subunit of CP, demonstrating that capping proteins and crosslinking proteins may have a synergistic role in maintaining the architecture of the actin network during CME [68, 69]. While crosslinking proteins have been shown to be important for proper endocytosis, where they are working in the invaginating membrane, and the how they function with other regulators is poorly understood. For instance, whether crosslinking occurs prior to or after filaments are capped is unknown.

#### *1.2.5 Actin disassembly factors*

The actin filaments at CME sites are not static from the time of their polymerization until vesicle scission. It is estimated that the actin network at CME turns over completely every 3-4 seconds [48]. Given that actin polymerization lasts for ~20 seconds during CME, assembly and disassembly are likely occurring concurrently. Numerous highly-conserved actin disassembly factors have been shown to be important for CME. These factors can function at any of three

levels during the actin disassembly process : (1) debranching, (2) severing/depolymerization and (3) monomer recycling. Debranching describes the process of removing the Arp2/3 from the sides of mother filaments. This is largely accomplished through the dedicated debranching factor, Gmf1, which binds to the Arp2/3 complex and releases it from the mother and daughter filament [70, 71]. At the center of severing and depolymerization is cofilin (Cof1), which is essential in yeast and required for the turnover of actin patches [72, 73]. The ability for cofilin to sever actin filaments by decorating the filament and inducing a conformational change in the helix has been well described [74]. Cofilin alone is not sufficient for filament severing and depolymerization, relying on Aip1, Srv2 and twinfilin (Twf1) for additional contributions [75-77]. Following depolymerization of F-actin, the resulting ADP-bound actin monomers must be converted back to ATP-G-Actin to be recharged for polymerization. The monomer recycling proteins Srv2 and profilin catalyze this process, with Srv2 having a particularly important role in yeast [78]. Through each of these processes, the nucleotide state of actin is of the utmost importance, as newer ATP-rich filaments may associate with different proteins than older ADP-rich filaments.

### *1.2.6 Actin associated proteins with unknown functions*

While many of the endocytic factors that arrive during the actin polymerization phase of CME have known functions, there are numerous that are poorly studied or do not have a clear mammalian homolog to infer a function from. One example is Aim21 (Altered Inheritance of Mitochondria 21), a little studied ~75 kDa protein. Aim21 was initially identified in a genome-wide screen for proteins whose deficiencies alter mitochondrial biogenesis or inheritance [79]. In addition, a GFP-tagged Aim21 was shown to co-localize with actin at cortical patches, linking it to endocytosis [80]. More recently, a genetic screen indicated Aim21 may be important for endocytosis [81]. While taken together, these findings suggested Aim21 may have a role in the actin polymerization phase of CME, the lack of a clear mammalian homolog and a lack of any

predicted secondary structure within the protein made it difficult to speculate on the potential function of Aim21.

Tda2 (Topoisomerase I Damage Affected 2) was first identified in a genetic screening for genes sensitive to Topoisomerase I-induced DNA damage, although the mechanism for this sensitivity has not been followed up [82]. More recently, a fluorescence microscopy based screen identified Tda2 as a novel endocytic factor [6]. Tda2 is a ~14.5 kDa protein with no clear homolog based on primary amino acid sequence. Following the identification of Tda2 as a novel endocytic factor, the crystal structure of Tda2 was solved and demonstrated it to be a symmetric homodimer, and unexpectedly, a structural homolog of the TcTex1 dynein light chain [83]. Interestingly, a proteomics study identified a potential physical interaction between Tda2, the little-studied endocytic factor Aim21, and actin capping protein [84]. Multiple studies would confirm that Tda2 forms a complex with Aim21, which together localize to CME sites during the actin polymerization stage [83, 85]. A reconstituted Tda2-Aim21 complex had the ability to interact with CP *in vitro*, although the significance of this interaction *in vivo* is a subject of debate (**Figure 1.2B**) [83, 85]. Despite these initial findings on Tda2, how it functions at the molecular level with Aim21 during CME remains poorly understood. One hypothesis is that the Tda2-Aim21 complex could be helping to recruit CP to CME sites, with fluorescence microscopy data supporting a recruitment defect of CP in both Tda2- and Aim21-null cells (**Figure 1.2C**) [83]. However, findings from another group suggest that Tda2 and Aim21 have little effect on CP localization to CME sites [85].

Bsp1 (Binding of Synaptojanin Protein 1) is a ~65 kDa protein that was identified as a binding partner for the yeast endocytic factors Inp52 and Inp53, both synaptojanin-type proteins that function as lipid phosphatases during CME [86]. Like Aim21, Bsp1 is predicted to be a largely disordered protein lacking secondary structure. Immunofluorescence imaging demonstrated that Bsp1 colocalized with cortical actin patches, later shown to be CME sites [86]. While Bsp1- and Abp1-null cells alone did not affect the internalization of  $\alpha$ -factor,

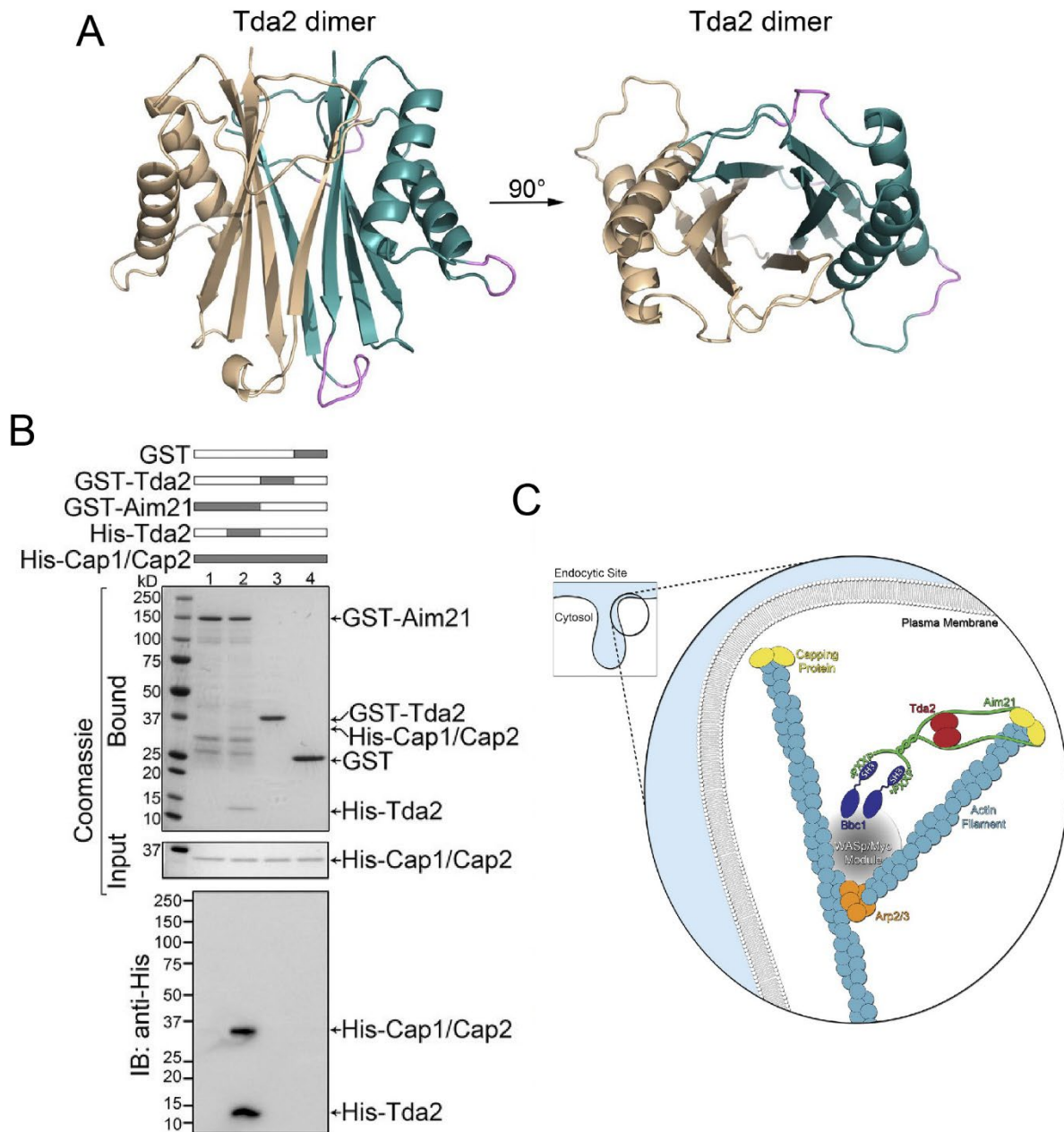


**Figure 1.2: Role of Tda2 and Aim21 in CME.** These figures were adapted from [citation]. (A) Crystal structure of the Tda2 homodimer (PDB Entry 5VKY). Structure is rotated 90° on the right for a view of the top-surface of Tda2. (B) A GST pull-down assay using purified recombinant proteins indicating His-Cap1/2 interacts with a reconstituted Tda2-Aim21 complex. (C) Model for the role of Tda2 and Aim21 in CME. The Tda2-Aim21 complex localizes to CME sites largely through the CME factor Bbc1. The interaction between the Tda2-Aim21 complex and CP could potentially aid in the localization of CP to endocytic sites.

combining the two resulted in a subtle defect in endocytosis, suggesting Bsp1 may have a redundant function during CME [86]. In addition to its localization to cortical actin patches, Bsp1 also localizes to the bud neck of yeast cells where it undergoes constriction, indicating that it is a component of the actomyosin ring that functions during cytokinesis [87]. However, cells lacking Bsp1 are able to complete cytokinesis with seemingly normal kinetics, suggesting that the role of Bsp1 in contraction of the actomyosin is auxiliary [87]. Despite these findings, how Bsp1 is functioning during CME and cytokinesis remains unknown.

### 1.3 Actin Capping Protein

#### 1.3.1 Actin capping protein background

Actin capping protein (CP), also known as  $\beta$ -actinin and CapZ, is a highly conserved complex that binds to the barbed end of actin filaments, preventing the addition or loss of additional actin subunits [88-90]. CP is a constitutive heterodimer consisting of an  $\alpha$  and  $\beta$  subunit, each with a molecular weight of ~30 kDa. While vertebrates express multiple isoforms of each CP subunit, other organisms have single genes for each subunit that encode a single gene product [91, 92]. CP binds to the barbed ends of F-actin with a 1:1 stoichiometry and with sub-nanomolar affinity *in vitro*, resulting in a dissociation half-time of nearly 30 minutes [93-95]. It has a critical role in assembly of Arp2/3-mediated branched actin networks, including in lamellipodia at the leading edge of motile cells [96]. In addition to limiting the overall length of actin filaments, CP binding to “unproductive” filaments is believed to reserve the pool of monomeric actin and funnel it to “productive” filaments near the plasma membrane [97, 98]. In muscle cells, CP caps the barbed end of actin filaments at the Z-disc of the sarcomere, hence its alternative name CapZ [89, 99]. Despite little sequence similarity between the two subunits, the crystal structure of CP demonstrates the complex folds into a mushroom shape with a surprising degree of structural symmetry [100]. The mushroom-shaped CP is functionally

divided into two components, the cap and the stalk. While the cap of the mushroom is responsible for capping actin filaments, the stalk region binds to- and is regulated by a subset of proteins containing CP-interacting (CPI) motifs (**Figure 1.3**)[101]. In addition to aiding in the localization of CP to branched actin networks, CPI motif-containing proteins have the ability to allosterically regulate CP, altering the affinity of CP for actin filament barbed ends [101, 102]. While CPI motif-containing proteins have been described in vertebrates, they have not been shown to function in budding yeast. In addition to allosteric regulation, the affinity of CP for barbed ends can be regulated sterically [101]. V-1, also known as myotrophin, binds to the cap region of CP and inhibits the CP:barbed end interaction [103, 104]. Additionally, phosphoinositides can bind to and inhibit CP *in vitro*, although the physiological relevance of this inhibition is not well understood [105, 106].

### 1.3.2 Capping mechanism

The crystal structure of chicken CP, which is highly conserved with human CP, was solved in 2003, and was a critical step in determining the mechanism of interaction between CP and F-actin barbed ends [100]. In the mushroom-shaped complex, the N-termini of both subunits are at the stalk, with the subunits heavily intertwined. At the top surface of the mushroom, the cap region, each subunit contains a C-terminal  $\alpha$  helix extension that extends out from the flat-top. The extreme ends of both C-termini were not clearly observed in the electron density. These C-terminal extensions were termed the  $\alpha$ -tentacle and  $\beta$ -tentacle for the  $\alpha$  and  $\beta$  subunits, respectively. Point mutations and truncations to each tentacle demonstrated that both were important for filament capping [95]. Of particular importance was the  $\alpha$ -tentacle, with its truncation resulting in a 5000-fold reduction in capping affinity [95]. As the tentacles are distal to each other in the crystal structure, it was hypothesized that CP interacted with multiple actin subunits at the barbed end. More recently, a low-resolution cryo-EM structure of CP bound

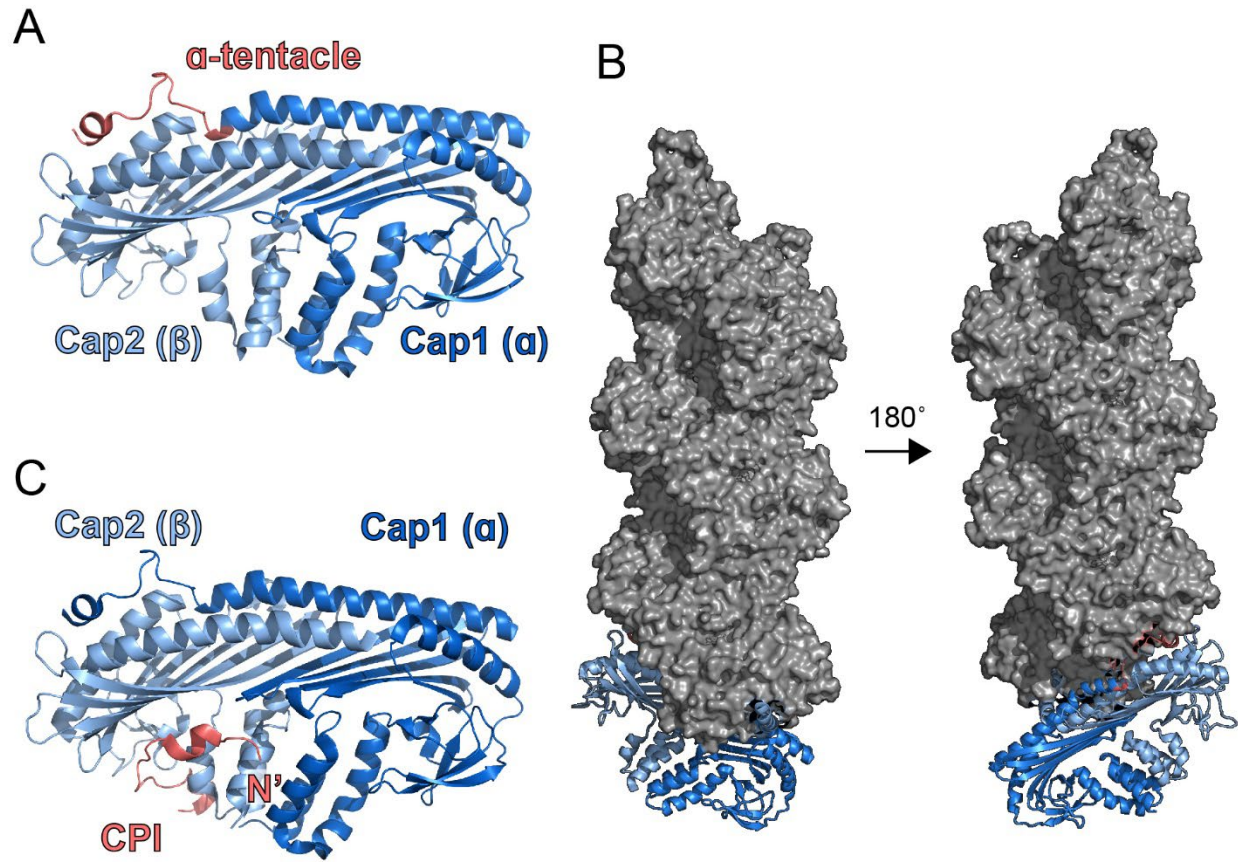


**Figure 1.3: Structures of the actin capping protein complex.** (A) Crystal structure of the actin capping protein complex (3AA7) displayed with the  $\alpha$ -subunit (Cap1) in dark blue and the  $\beta$ -subunit (Cap2) in light blue. The  $\alpha$ -tentacle, which is critical for the capping function of CP, is shown in red. (B) Crystal structure of the CP complex bound to the CPI motif of CD2AP (3AA6). The  $\alpha$ -subunit (Cap1) is displayed in dark blue, the  $\beta$ -subunit (Cap2) in light blue and the CPI motif of CD2AP is displayed in red. The N-terminus of the CPI motif is denoted with N'. (C) Cryo-EM structure of a CP capped actin filament (7PDZ) displayed with the  $\alpha$ -subunit (Cap1) in dark blue, the  $\beta$ -subunit (Cap2) in light blue, the  $\alpha$ -tentacle in red and the actin filament in grey. The structure is rotated 180 degrees on the right for a view of the  $\alpha$ -tentacle binding surface

to the barbed end of an actin filament provided support for the this theory [107]. These, among other studies, have led to a capping model where the  $\alpha$ -tentacle of CP first binds the actin filament through electrostatic interactions, followed by the  $\beta$ -tentacle binding to the F-actin largely via hydrophobic interactions [94, 107]. A recent co-crystal structure of CP bound to an actin filament barbed end substantiated this model [108].

### 1.3.3 Inhibition of CP by V-1

V-1 is a ~13 kDa ankyrin repeat-containing protein that was initially identified as a developmentally regulated protein in the rat cerebellum [109]. A proteomics study conducted to identify protein interactors with V-1 later identified CP as a V-1-interactor [104]. V-1 interacts with CP strongly in a 1:1 stoichiometry, and inhibits the capping function of CP [103]. While V-1 can inhibit CP from capping actin filaments, it does not interact with CP that is bound to F-actin [103]. Together, these findings suggested that V-1 may have an overlapping binding site on CP with the actin filament barbed end. Indeed, co-crystal and NMR structures have confirmed that V-1 interacts with the capping surface of CP, specifically with the  $\alpha$ -tentacle [110, 111]. This steric regulation of CP suggested that CP is not a constitutively active F-actin capper, and that there must be a mechanism to displace V-1 from CP, thereby activating the capping function of CP. While V-1 is well conserved in vertebrates, and even in the slime mold *Dicyostelium discoideum*, there is no clear homolog in budding yeast.

### 1.3.4 Capping protein interacting motifs

Capping protein-interacting (CPI) motifs are short motifs that facilitate the interaction with- and regulation of CP [101]. In early CP studies, a diverse set of proteins that interact directly with CP were identified in various organism [112-115]. Other than working at actin networks, these proteins were otherwise unrelated. In each of these cases, the CP-interacting protein decreased capping of actin filaments by CP in *in vitro* assays, and unlike V-1, they could

uncap capped filaments and allow them to elongate [112-115]. This led to the early hypothesis that these CPI motif proteins could be working downstream of CP binding to barbed ends, working to uncap and recycle CP [116]. The identification of numerous CP-interacting proteins allowed for the identification of a consensus CPI motif, a relatively flexible sequence rich in basic residues [116]. Solving the co-crystal structure of CP in complex with one of the CPI motifs indicated that the interaction occurs at the stalk region of CP, opposite the capping surface [116]. This important finding indicated that the inhibition/uncapping activity of CPI motifs is likely occurring through an allosteric mechanism. Numerous recent structural studies have confirmed this notion [111, 117, 118]. The best studied family of CPI motif proteins are the CARMIL (CP, Arp2/3 Myosin-I Linker) family of proteins, large multi-domain proteins that are important for actin-based motility [119]. While the early hypothesis for the function of CPI motifs in cells was to uncap actin filaments, CARMIL was later shown to be required for proper localization of CP to the actin network at the leading edge of cells [102]. In addition, the CPI motif-containing protein CD2AP was needed for localization of CP to lamellipodia [120]. These finding that CP was actively recruited to barbed ends contradicted the previous notion that CP freely diffused through the cytosol to stochastically bind barbed ends [98]. Given this, and that CPI motifs bind with nanomolar affinity to CP and reduce CPs ability to cap barbed ends [121], CPI motif proteins are likely to recruit CP as a transient capper. While a diverse group of CPI motif-containing proteins are present in many eukaryotes from slime mold to humans, they have not been identified in yeast.

### 1.3.5 *The Fujiwara model*

In addition to uncapping actin filaments and inhibiting CP in *in vitro* assays [116, 121], CPI motifs can bind to a CP:V-1 complex and induce dissociation on V-1 [121]. While the CP:V-1 complex is not able to bind barbed ends [103, 111], the CP:CPI still caps barbed ends with nanomolar affinity, compared to sub-nanomolar with CP alone [121]. Together these findings

have led to a model for the function of CP and its regulators in cells, termed the Fujiwara model [122]. According to this model, CP is initially bound to V-1 and inactive in the cytosol. Next, a CPI motif protein binds to CP:V-1, thereby dissociating V-1, and partially activating CP. Following this, the transient capper, CP:CPI, is recruited to the branched actin network, and the complex binds to the barbed ends of actin filaments. Finally, an unknown mechanism results in the dissociation of the CPI motif, removal of CP from barbed ends, and recharging of the inactive CP:V-1 complex.

### 1.3.6 *Twinfilin – a divergent CPI motif*

Twinfilin is a well-conserved actin disassembly factor that was originally identified and characterized in budding yeast. Early experiments indicated that twinfilin interacted directly with CP, and that this interaction was important for the localization of twinfilin, but not CP, to CME sites, providing an early link between twinfilin and CP [123, 124]. Twinfilin contains two actin depolymerization factor-homology (ADFH) domains separated by a short linker, and a short C-terminal tail. While twinfilin is categorized as an actin disassembly factor, how it functions physiologically is the subject of great debate. Findings from numerous *in vitro* studies have described twinfilin as: 1) an actin monomer sequestering protein, 2) a barbed end capping protein, 3) a barbed end depolymerization factor and a 4) pointed end depolymerization factor [125]. Recently, it was shown that the C-terminal tail of mouse twinfilin contained a sequence distantly related to the consensus CPI motif sequence that facilitated its direct interaction with CP [126]. The CPI motifs of twinfilin and CARMIL compete with each other for binding to CP, demonstrating an overlapping binding site on CP [126]. However, unlike CPI motif proteins and V-1, the twinfilin CPI motif did not inhibit the actin capping function of CP [126]. Somewhat surprisingly, the CPI motif of twinfilin was able to dissociate V-1 from the CP:V-1 complex, thus activating CP [126]. Given these findings, the group described twinfilin as a novel “pro-capping” CPI motif, as twinfilin activated CP while not affecting its capping function. Around the same

time, a different group dissected the role of twinfilin and CP with a larger focus on *in vivo* experiments [127]. While this group shared many of the same findings, their results argued against the characterization of twinfilin as a “pro-capping” factor, as twinfilin required interaction with CP for its localization but not vice-versa [127]. The group postulated that twinfilin works downstream of CP being recruited to barbed ends, which occurs via CARMIL-type CPI motifs, and uncaps CP from the barbed ends to allow for turnover of the network upon an unknown trigger [127]. While the trigger for twinfilin to uncap is still unknown, the group speculated that ATP hydrolysis of the actin filament could play a role, with CP bound to newer, ATP-rich filament being protected from uncapping [127]. Thus, while much is known about twinfilin, how it functions in cells is still muddled.

### 1.3.7 CP in budding yeast

In budding yeast, the CP  $\alpha$  and  $\beta$  subunits are encoded by the *CAP1* and *CAP2* genes respectively [63, 128]. Given this, CP is often referred to as Cap1/2 or Cap1/Cap2. Early studies of yeast CP sought to confirm a conserved-function of CP as a capping protein that works at yeast actin networks. Immunofluorescence imaging demonstrated that CP co-localized with actin at cortical patches, later known to be sites of CME, but not actin cables or the actomyosin ring [62]. Deletion of either *CAP1* or *CAP2* resulted in equivalent phenotypes. While cells were viable, deletion of either gene resulted in fewer actin cables within the cell, a phenotype consistent with a defect in capping actin filaments [63, 128]. Additionally, deletion of either gene led to reduced levels of the remaining gene product, likely due to destabilization and degradation of the lone subunit [128]. CP could be purified from yeast as a heterodimer, and this heterodimer retained capping activity that was inhibited by phosphoinositides [62]. Together, these early studies confirmed that *CAP1* and *CAP2* encode the  $\alpha$  and  $\beta$  subunits of CP respectively, and that the capping function of CP is conserved in yeast.

Nearly 10 years after these initial studies on yeast CP, advances in live-cell microscopy techniques allowed for visualization of the dynamic nature of CP at CME sites. In a landmark study for the endocytic field, two-color live-cell fluorescence microscopy demonstrated that a GFP-tagged Cap1 expressed from its endogenous locus has similar patch dynamics as Abp1-RFP, a marker for F-actin at cortical actin patches [9]. Both Cap1-GFP and Cap2-GFP displayed patch lifetimes of ~ 20 seconds [9]. When yeast cells were treated with latrunculin A, Cap1-GFP was diffuse in the cytosol, demonstrating that actin polymerization was necessary for its localization to endocytic sites [9]. Importantly, *cap1* $\Delta$  and *cap2* $\Delta$  displayed an endocytic phenotype consistent with a defect in actin filament capping, with brighter Abp1-RFP patches that persisted for over double the time, indicative of an overgrown and inefficient actin network [9].

Around the same time, the crystal structure of chicken CP was solved, and the mechanism for interaction between CP and barbed ends was determined [95, 100]. To confirm that the mechanism for CP interaction with barbed ends is conserved, a series of *in vitro* capping experiments using recombinant CP purified from bacteria were performed [129]. Wild-type recombinant CP bound strongly to barbed ends, with a dissociation constant of ~ 4nM [129]. When either of the tentacles of CP was truncated, the mutant CPs were unable to cap the actin filaments, and point mutations to the tentacles had similar effects [129]. The  $\alpha$ -tentacle alone was able to bind to- and cap barbed ends but only with low affinity, showing that the  $\alpha$ -tentacle was not sufficient for full capping activity [129]. Immunofluorescence imaging showed that the  $\alpha$ -tentacle was essential for the function of CP during CME, as actin patches were brighter and CP recruitment was diminished when the  $\alpha$ -tentacle of CP was truncated [129]. However, while CP displayed a recruitment defect when it was not able to bind F-actin, it was still present at reduced levels, indicating that CP may rely on other endocytic factors for proper recruitment to CME sites. This begs the question, what other factors could be contributing to CP recruitment to CME sites? The obvious answer would be a CPI motif-containing protein, but

there are no clear homologs present in yeast. Additionally, as there is no V-1 homolog in yeast, and thus CP likely does not need to be activated, would a CPI motif protein even be needed? Interestingly, a complex of the little-studied endocytic factors, Tda2 and Aim21, interacts directly with CP *in vitro* and deletion of either gene results in a slight CP recruitment defect [83].

While there is no homolog of V-1 in budding yeast, and no clear homologs of CPI motif-containing proteins, the CP-binding protein, twinfilin (Twf1), is well-conserved from yeast to mammals. The non-essential gene *TWF1* encodes the well-conserved actin disassembly factor [77]. Twinfilin was first identified in budding yeast as an actin monomer sequestering protein that localizes to cortical actin patches [77]. As is the case with twinfilin in higher eukaryotes, the multitude of *in vitro* functions twinfilin holds has made the task of determining its function *in vivo* difficult. Twinfilin localization to CME sites is dependent on CP, as deletion of either the *CAP1* or *CAP2* gene leads to diffuse cytoplasmic twinfilin [123]. Additionally, twinfilin and CP were shown to interact directly *in vitro* [123]. The interaction between twinfilin and CP occurs through the C-terminal tail of twinfilin, and the interaction does not affect the ability of CP to bind barbed ends [124]. While twinfilin is dependent on CP for its localization, CP localizes to CME sites independent of twinfilin [124]. Given the new findings on the divergent CPI motif present in vertebrate twinfilin, it's likely that yeast Twf1 also has a CPI motif in its C-terminal that facilitates interaction with CP, although this has not been shown explicitly. Despite these numerous findings, the physiological function of twinfilin remains unsettled both in yeast and in higher eukaryotes.

## 1.4 Overview of Dissertation

The main objective of the work presented in this dissertation is to understand how actin capping protein (CP) is regulated during clathrin-mediated endocytosis (CME) in budding yeast.

In Chapter 2, I present my findings on the molecular function of the endocytic factor Tda2 during CME. This work was published in *Molecular Biology of the Cell* (MBoC) in 2021 [130]. Additionally, a protocol I developed for a method utilized in this paper was published in *STAR Protocols* in 2022 [131]. Tda2 was first identified as a novel endocytic factor by a previous graduate student in the lab, Kristen Farrell [6]. In a follow-up paper published in the *Journal of Cell Biology* (JCB) in 2017 by our lab, the crystal structure of Tda2 was solved with help from collaborators, and a potential role for Tda2 during CME was established [83]. I began my work in the Di Pietro laboratory as a rotation student when the work in this paper was being completed, and am included as a middle author on the publication. In the work described in chapter 2, My findings support Tda2 functioning as a dimerization engine for another endocytic factor, Aim21. Together, the Tda2-Aim21 complex interacts directly with CP to recruit it to CME sites.

In Chapter 3, I present my findings on how CP is regulated by three CPI motif-containing endocytic factors during CME in budding yeast. At the time of this writing, this work is in the process of being finalized for submission to a peer reviewed journal. While my previous work laid the groundwork for the idea that the Tda2-Aim21 complex interacts directly with CP, how it's regulating CP is still poorly understood. In addition to the Tda2-Aim21 complex, this work explores two additional endocytic factors that interact with- and regulate CP during CME, Bsp1 and Twf1 (Twinfilin). My work demonstrates that the three CPI motif proteins involved in CME regulate CP in distinct ways.

## CHAPTER 2

### TDA2 FUNCTIONS AS A DIMERIZATION ENGINE FOR AIM21 TO REGULATE ACTIN CAPPING PROTEIN DURING CME

#### 2.1 Summary

This chapter is reproduced with slight changes from an article published in *MBoC* (Lamb et al., 2021) [130]. Clathrin- and actin-mediated endocytosis is a fundamental process in eukaryotic cells. Previously, we discovered Tda2 as a new yeast dynein light chain that works with Aim21 to regulate actin assembly during endocytosis. Here, we show Tda2 functions as a dimerization engine bringing two Aim21 molecules together using a novel binding surface different than the canonical dynein light chain ligand binding groove. Point mutations on either protein that diminish the Tda2-Aim21 interaction *in vitro* cause the same *in vivo* phenotype as *TDA2* deletion showing reduced actin capping protein recruitment and increased filamentous actin at endocytic sites. Remarkably, chemically induced dimerization of Aim21 rescues the endocytic phenotype of *TDA2* deletion. We also uncovered a capping protein interacting motif in Aim21, expanding its function to a fundamental cellular pathway and showing such motif exists outside mammalian cells. Furthermore, specific disruption of this motif causes the same deficit of actin capping protein recruitment and increased filamentous actin at endocytic sites as *AIM21* deletion. Thus, the data indicates the Tda2-Aim21 complex functions in actin assembly primarily through capping protein regulation. Collectively, our results provide a mechanistic view of the Tda2-Aim21 complex and its function in actin network regulation at endocytic sites.

## 2.2 Introduction

Endocytosis is vital for processes such as nutrient uptake, cell signaling, maintenance of membrane composition and virus internalization. A major endocytic pathway is clathrin-mediated endocytosis (CME), an essential pathway in all eukaryotic cells [132, 133]. The CME pathway is highly conserved from yeast to mammalian cells in components, progression and function [11, 32, 33, 134-138]. CME is a highly choreographed process involving the sequential assembly of nearly 60 proteins at endocytic patches on the plasma membrane [9, 33, 139]. These endocytic factors work together to collect cargo into a clathrin-coated pit, invaginate the surrounding membrane, and pinch off the invagination as a vesicle inside the cell. Despite its crucial role in cell physiology, many aspects of CME and its regulation remain poorly understood. For example, the molecular function of numerous endocytic factors has not been elucidated [6, 88, 139].

In budding yeast, CME is reliant on polymerization of a branched actin network to provide the force necessary for membrane invagination [48, 140]. When cells are treated with latrunculin A to inhibit actin polymerization, membrane invagination fails to occur, and endocytosis is stalled. Numerous regulatory factors are needed for the proper formation of branched actin networks. One key regulator is actin capping protein (CP), which binds to the barbed end of actin filaments with high affinity to prevent the loss or addition of actin subunits [88, 129]. CP is a well-conserved heterodimer consisting of an alpha and beta subunit. Yeast cells with a deletion of the *CAP1* or *CAP2* genes encoding either subunit of CP exhibit an abnormally large actin network and defect in CME [9, 63]. In higher eukaryotes, regulation of CP by proteins containing a capping protein-interacting (CPI) motif has been demonstrated [101, 102, 114, 116, 122, 126, 127, 141]. One of the best studied of these is the CARMIL family of proteins, which bind to CP through a CPI motif to regulate the localization and function of CP

[101, 119]. While CP is highly conserved throughout eukaryotes, its unknown whether CPI motifs regulate CP in yeast.

Dynein light chains (DLCs) were first identified as accessory proteins in the microtubule-associated dynein motor complex, where they interact directly with the dynein intermediate chain. However, they have since been reported to interact with a diverse group of proteins and have functions independent of the dynein motor complex [142-147]. Three families of DLCs have been described: the LC8 family, the TcTex1 family, and the roadblock family. All three families form symmetric homodimers with two identical ligand binding sites. While the better studied LC8 and TcTex1 families share a common fold, the roadblock family has a divergent fold. Interestingly, many of the reported binding partners of DLCs are dimeric or have dimerization domains themselves, including the dynein intermediate chain. Thus, DLCs have been proposed to function as dimerization hubs for their numerous binding partners [142, 146, 148-151]. While yeast have an LC8 DLC that is part of the dynein motor complex, neither TcTex1 or roadblock were thought to exist until recently.

Tda2 was recently identified as a novel factor in yeast CME [6]. The crystal structure of Tda2 demonstrates it to be a symmetric homodimer, and unexpectedly, a structural homolog of the TcTex1 DLC [83]. In accord with other DLCs, Tda2 was demonstrated to be a dimer in solution through analytical ultracentrifugation [83]. Tda2 does not function as part of the dynein motor complex, but instead forms a complex with the little-studied endocytic factor Aim21, which together localize to CME sites during the actin polymerization stage [83, 85]. Thus, Tda2 represents a unique example of a DLC that works in endocytosis and regulates the actin cytoskeleton. Aim21 (YIR003W) was initially identified in genome-wide screenings as a protein localized to CME sites and needed for normal cargo endocytosis as well as for normal mitochondrial inheritance, but how it may accomplish these functions was unclear [6, 79-81]. More recently, a

reconstituted Tda2-Aim21 complex was shown to interact with CP *in vitro*, although the significance of this interaction for regulation of actin assembly *in vivo* is a subject of debate [83, 85]. Despite these initial findings on Tda2 and Aim21, how they function at the molecular level during CME remains poorly understood.

Here, we uncover the molecular function of Tda2 as a dimerization engine for its binding partner Aim21 and characterize the Tda2-Aim21 complex as an heterotetramer. Tda2-induced dimerization of Aim21 facilitates its proper localization and interaction with CP through a newly defined CPI motif of Aim21. Furthermore, point mutation of the Aim21 CPI motif recapitulates the endocytic phenotype of *AIM21* gene deletion suggesting the Tda2-Aim21 complex regulates actin polymerization chiefly through actin capping protein.

## 2.3 Results

### 2.3.1 *The Tda2 binding region of Aim21 maps near its C-terminus*

While it has been established that Aim21 interacts directly with Tda2, the precise region of Aim21 responsible for the interaction is less clear [83, 85]. To determine the region of Aim21 that interacts with Tda2, a series of yeast two-hybrid (Y2H) experiments were performed. Initially, ~100-amino acid (AA) fragments of Aim21 were tested for interaction with Tda2. Of the eight Aim21 fragments tested, only AA 495-595 interacted with Tda2, indicated by growth on selective medium lacking histidine (-HIS; **Figure 2.1A**). Growth persisted even at a high concentration of 3-amino-1,2,4-triazole (3AT), indicating a strong interaction (**Figure 2.1A**). Stronger growth by the AA 495-595 fragment relative to full length Aim21 may reflect higher expression level of the fragment or partial steric hindrance for interaction with full length Aim21. The AA 495-595 fragment was further sectioned into ~30-amino acid fragments within the 495-595 region, and interaction with Tda2 was detected for both the AA 510-540 and AA 525-555 fragments (**Figure 2.2A**). Lastly, the region spanning AA 510-555 was sectioned into 16-amino



histidine (-HIS) and supplemented with various concentrations of 3AT. Cell growth was detected with full length Aim21 and the AA 495-595 fragment, indicative of an interaction with Tda2. (B) Yeast two-hybrid analysis with Tda2 and varying 15-amino acid fragments of Aim21 between amino acids 510-555. Equivalent strength interactions were detected for the AA 525-540 and AA 530-545 fragments. (C) A GST-pulldown assay was performed with GST fused to a fragment of Aim21 spanning amino acids 510-555. The GST-Aim21 fusions either contained no mutations (wild-type) or contained a single amino acid mutated to alanine. Each GST fusion protein was incubated with His-Tda2, and bound proteins were analyzed by SDS-PAGE and Coomassie staining. The W536A mutation to Aim21 severely decreased Tda2 binding, while the F533A mutation showed a moderate decrease. (D) A GST-pulldown assay was performed as in Fig. 1C, now using GST-Aim21 fusions with tandem amino acid mutations. Mutating amino acids surrounding F533 exacerbated the effect of the F533A mutation. (E) Organization of Aim21 Domains. PxxP = Polyproline motif-rich region. TBR = Tda2 binding region. The Tda2 binding region sequence spanning amino acids 525-540 is shown below Aim21. The underlined sequence spanning amino acids 530-540 represents the core binding region, and the critical amino acids F533 and W536 are marked with an asterisk.

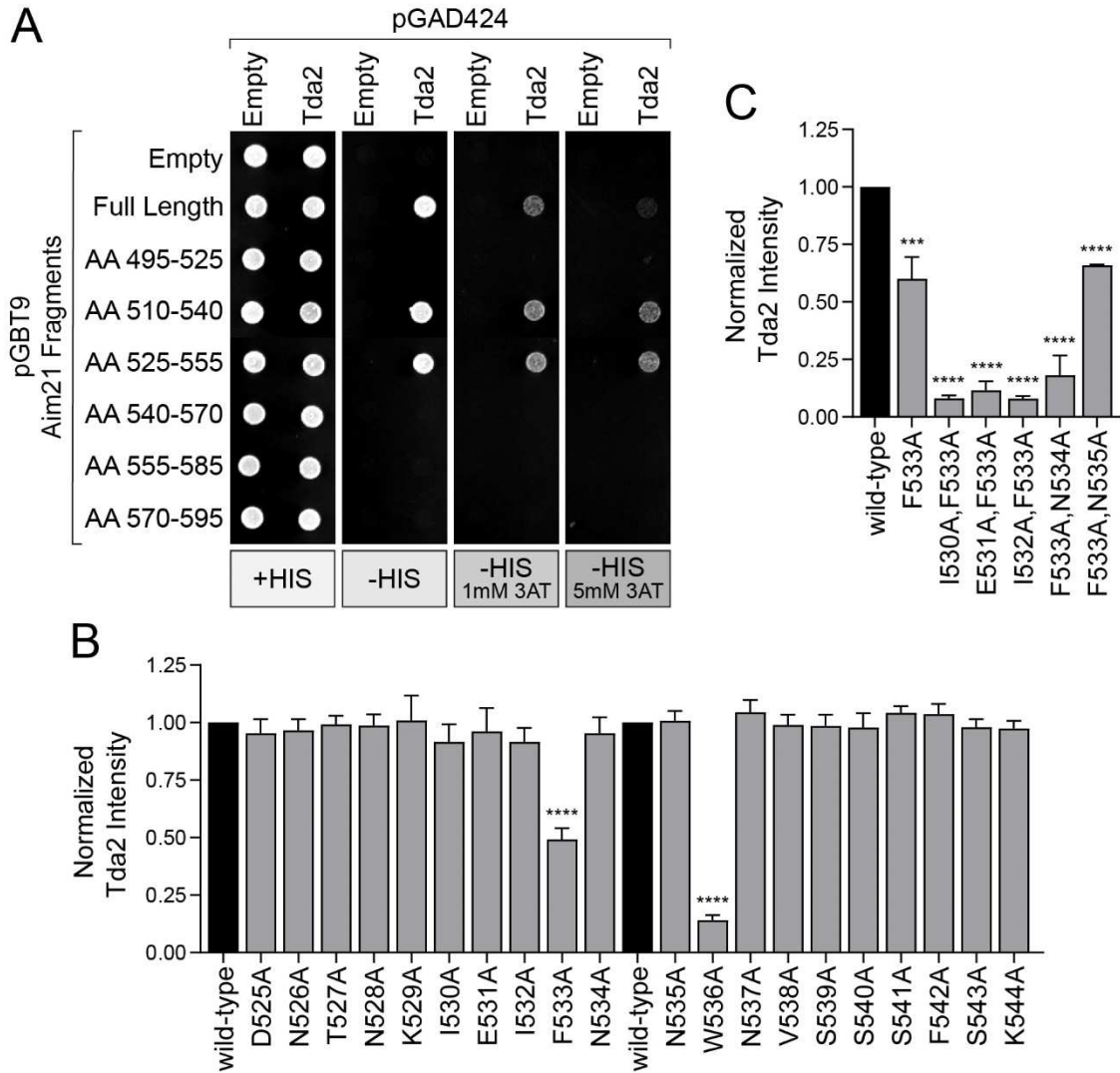


**Figure 2.2: Tda2 interacts with Aim21 near its C-terminus.** (A) Yeast two-hybrid analysis of cells co-transformed with plasmids expressing the GAL4 activation (pGAD424) and binding (pGBT9) domains fused to Tda2 and 30-amino acid fragments of Aim21 between amino acids 495-595, respectively. Cells were spotted onto plates containing histidine (+HIS, control) or selective medium lacking histidine (-HIS) and supplemented with various concentrations of 3AT. Cell growth was detected with full length Aim21 and the both the AA 510-540 and AA 525-555 fragments, indicative of an interaction with Tda2. (B) Quantification of GST-pulldown results in Figure 1C. Both F533A and W536A Tda2 mutants show a significant decrease in Aim21 binding,  $n = 3$  independent experiments. Error bars, mean with standard deviation, \*\*\*\* $P \leq 0.0001$ . (C) Quantification of GST-pulldown results in Figure 1D. Mutating amino acids surrounding F533 exacerbate the effect of the F533A mutation,  $n = 3$  independent experiments. Error bars, mean with standard deviation, \*\*\* $P \leq .001$ , \*\*\*\* $P \leq 0.0001$ .

acid fragments. Two overlapping fragments, AA 525-540 and AA 530-545, both displayed an interaction with Tda2 (**Figure 2.1B**). The fragments exhibited similar growth even at high concentrations of 3AT, suggesting the amino acids shared between the two fragments, AA 530-540, represents the core binding region (**Figure 2.1B**).

Having established AA 530-540 as the region of Aim21 that interacts with Tda2, we next wanted to determine which amino acids in the region were important for the interaction. A series of GST pulldown assays using purified recombinant proteins were performed to identify the important residues. A truncated Aim21 containing the Tda2 binding region was fused to glutathione-S-transferase (GST-Aim21<sup>510-555</sup>) and alanine scanning mutagenesis was performed between residues 525-544. GST-Aim21 fusion proteins were immobilized on glutathione Sepharose resin and subsequently incubated with 6-histidine-tagged Tda2 (His-Tda2). SDS-PAGE analysis showed robust binding of His-Tda2 to GST-Aim21<sup>510-555</sup>, consistent with the Y2H results (**Figure 2.1C**). Importantly, the W536A mutation abolished the Tda2-Aim21 interaction and the F533A mutant exhibited decreased Tda2 binding (**Figure 2.1C, 2.2B**). To further probe the importance of F533 to the Tda2-Aim21 interaction, the experiment was repeated using mutants harboring a second mutation surrounding the F533A mutation. Each of the I530A, E531A, I532A and N534A mutations significantly exacerbated the Tda2 binding defect seen with F533A alone (**Figure 2.1D, 2.2C**). Thus, the Aim21 region spanning AA 530-540 encompasses the Tda2 binding region (TBR), with the large, hydrophobic residues F533 and W536 particularly important for the interaction (**Figure 2.1E**). The data also suggest minor contributions to binding from Aim21 residues I530, E531, I532 and N534. Sequence alignment shows the Aim21 TBR is well conserved among fungi, especially key residue W536 (**Figure 2.3**). There are no clear homologs of Aim21 in higher eukaryotes.

Aim21 1-PxxP-PxxP-PxxP-CPI-TBR-679

		% Identity		
		FL	CPI	TBR
	<b>CPI</b>			
	<b>TBR</b>			
<i>Saccharomyces cerevisiae</i>	AKTGPLGGTRRG <b>RGPRGR</b> KLPSKVASVEKIEEDDNTNKIEI <b>FNNWN</b> VSSSFSK	74	88	91
<i>Saccharomyces paradoxus</i>	AKNGPLGNTRRARGPRGRKLPSKVASVEKVEEDDNTNKIEI <b>FNNWN</b> VVSFSK	54	81	91
<i>Saccharomyces kudriavzevii</i>	TKNVSLSSTRRARGPRGRKLPSKVAGVEKIEEDSNSNEIEI <b>FNNWN</b> VVSFPSK	52	81	73
<i>Saccharomyces eubayanus</i>	ARSTPLSNTRRARGPRGRKLPSKVAAVEKVEENGNKNGIEI <b>FNI</b> IWHVYSIPSK	29	69	46
<i>Kazachstania africana</i>	RNEVSDVRQRRARGPRGRKLPSVSNVKKVVAENSTSSIEV <b>F</b> EVWTISNVRKA	26	63	55
<i>Candida glabrata</i>	GTNLKDVRHGRARGPRGRKLPTKVATTEKVKVSETGNTIEI <b>F</b> SAWKLSTIKGQV	26	63	46
<i>Zygosaccharomyces rouxii</i>	PPSVSNVRSRRARGPRGRKLPSNVASVEKVNSESKTNEIEI <b>F</b> KTWKTVVHKKE	26	63	46
<i>Zygosaccharomyces bailii</i>	TKPAPSVRQPRARGPRGRKLPSVAAVEKVSSESKTNEIEI <b>F</b> KTWRTVMFKPV	25	69	46
<i>Torulaspota globosa</i>	TRTPSESQRRARGPRGRKLPSLVANVEKVK-TENSNDIE <b>L</b> FHMWTIVSNRD	25	33	27
<i>Kluyveromyces lactis</i>	AELPKVPARSKKTRGPHKRLPKTVASIEKVE-TKSTNSI <b>S</b> VVKTWSISFKPDL	23	33	18
<i>Kluyveromyces marxianus</i>	QSIPTPSRPKRSKGPAKRLPKNVSSIEKVD-AKSTFDV <b>G</b> VVKAWSVIVKPTP	23	56	36
<i>Saccharomycodes ludwigii</i>	EKKIDDVRQKRARGPRGRRLPTKIANVEKIEVKANENVVEVFD <b>T</b> WCFSFADND	21	53	36
<i>Eremothecium gossypii</i>	TVPAPLPTSNTRVRGPRSRKLPSAFKGVEKAK-PVSTNTI <b>S</b> FP <b>T</b> WSV <b>T</b> FTARA	20	63	27
<i>Candida albicans</i>	ESATANAPVRRTRGPRGKLPKAVADAEVKTE--SRFA <b>I</b> ESGKLWSIEFKKKI			
Human CD2AP	SSENLHLTLANRPKMPGRRLPGRFNG	15	33	--
Human CIN85	STEKLSHPTTSRPKATGRRP <b>S</b> QSLT	15	33	--

**Figure 2.3: The CPI motif and TBR of *S. cerevisiae* Aim21 are conserved throughout budding yeasts.** Alignment of the capping protein-interacting (CPI) motif and Tda2 binding region (TBR) of *S. cerevisiae* Aim21 with homologs from other budding yeasts. The critical residues R504, R507, R509, F533 and W536 of *S. cerevisiae* Aim21 are shown in bold. Percent identity comparing *S. cerevisiae* Aim21 to other budding yeast species were determined through multiple sequence alignments of respective regions using Clustal Omega. The CPI motif regions of two human proteins, CD2AP and CIN85, are shown at bottom for comparison. Accession numbers from top to bottom: *S. cerevisiae* (NP\_012268.3), *S. paradoxus* (XP\_033767044.1), *S. kudriavzevii* (EJT44884.1), *S. eubayanus* (XP\_018221609.1), *K. africana* (XP\_003959597.1), *C. glabrata* (KTB14665.1), *Z. rouxii* (XP\_002498168.1), *Z. baillii* (CDF91740.1), *T. globosa* (XP\_037140682.1), *K. lactis* (QEU60886.1), *K. marxianus* (QGN16745.1), *S. ludwigii* (SSD61678.1), *E. gossypii* (NP\_984110.2), *C. albicans* (C4YD35.1), CD2AP (NP\_036252.1), CIN85 (NP\_114098.1).

### 2.3.2 *Tda2 interacts with Aim21 through a distinct mechanism from other DLCs*

To determine the binding affinity between Tda2 and Aim21, a series of fluorescence polarization assays were performed. A FITC-labelled Aim21 peptide spanning amino acids 529-539 (FITC-Aim21) was titrated with various concentrations of His-Tda2, and fluorescence polarization values were measured. Interestingly, when the data were fit to both one-site and two-site binding isotherms, the binding was more consistent with the two-site model (**Figure 2.4A,B**, one-site and two-site binding isotherms shown with red and black lines, respectively). Considering the more likely two-site model, the affinities of the binding events were  $K_{d1}$  of  $1.9 \pm 0.2 \mu\text{M}$  and  $K_{d2}$  of  $28 \pm 3 \mu\text{M}$  (**Figure 2.4B**). In comparison, a mutated Aim21 peptide with I532A and F533A (FITC-Aim21\*) exhibited no binding to Tda2, consistent with the GST pulldown data (Figure 2B). To determine the stoichiometry of the higher affinity binding event, a concentration of  $10 \mu\text{M}$  FITC-Aim21, well above  $K_{d1}$ , was titrated with His-Tda2. Binding steadily increased until the concentration reached  $5 \mu\text{M}$  Tda2 dimer and then leveled off, indicative of a 2:1 stoichiometry between Aim21 and the Tda2 homodimer (**Figure 2.4C**). This and other data (see below) indicate the high affinity binding event detected by this assay is likely the physiologically relevant binding event and allows a Tda2 homodimer to act as a dimerization engine for Aim21.

Available structures of liganded TcTex1- and LC8-type DLCs show interactions occur in canonical binding grooves where the ligands bind in an extended conformation that effectively adds two strands to the  $\beta$ -sheets found on the two symmetrically equivalent faces of the homodimeric DLCs [149]. To determine if the Tda2-Aim21 interaction occurs in the same fashion, a GST pulldown experiment was performed with Tda2 mutants targeting two distinct regions of the Tda2 homodimer. To disrupt interactions in the canonical  $\beta$ -strand binding groove, residues F86, I103 and K107 of Tda2 were mutated (**Figure 2.4D top**). Additionally, mutations were made to target the top face of the Tda2 homodimer, where solvent exposed hydrophobic pockets could accommodate the largely hydrophobic Aim21 peptide segment

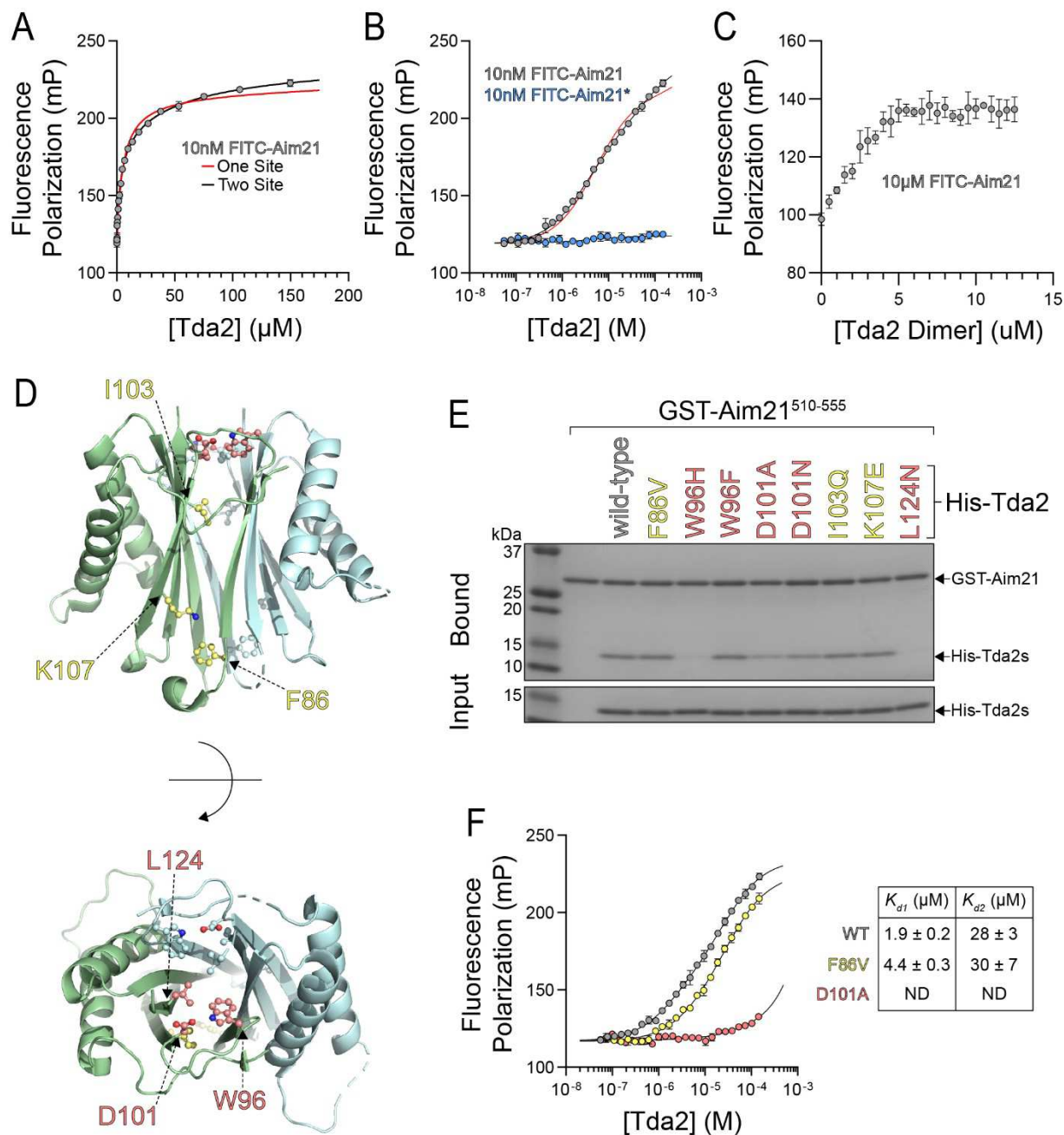


**Figure 2.4: Tda2 interacts with Aim21 through distinct mechanism.** (A) A fluorescence polarization assay was performed using 10nM FITC-Labelled Aim21 peptide spanning amino acids 529-539 (FITC-Aim21) and various concentrations of His-Tda2. Data points represent the average and standard deviation from a single representative experiment performed in three technical replicates. Note that error is too small for most Tda2 concentration data points to produce an error bar larger than the symbol. The data were fit to both 1-site (red line) and 2-site (black line) binding isotherms. The Tda2-Aim21 interaction most likely occurs through a 2-site model. (B) A fluorescence polarization assay was performed using either 10nM FITC-Aim21 peptide (FITC-Aim21; KIEIFNNWNVS) or a mutant peptide (FITC-Aim21\*; KIEAANNWNVS). FITC-Aim21\* displayed no interaction with Tda2. The data were fit to both 1-site (red line) and

2-site (black line) binding isotherms. (C) A fluorescence polarization assay was performed using 10 $\mu$ M FITC-Aim21 peptide and various concentrations of His-Tda2. FITC-Aim21 became saturated at a Tda2 Dimer concentration of 5  $\mu$ M, indicating a stoichiometry of 2:1 between Aim21 and the Tda2 dimer for the high affinity binding event. (D, top) Crystal structure of the Tda2 homodimer (PDB entry 5VKY). One Tda2 molecule is shown in pale green, and the other in pale cyan. The residues F86, I103 and K107 are colored yellow and indicated with arrows on one Tda2 molecule. These residues sit along the canonical  $\beta$ -strand binding groove that has been described for other dynein light chain-ligand interactions. (Bottom) The Tda2 homodimer is rotated 90° for a view of the top face of the homodimer. The residues W96, D101 and L124 are shown as spheres and colored in salmon and indicated with arrows on one Tda2 molecule. (E) GST-pulldown assay data from GST fused to a fragment spanning amino acids 510-555 of Aim21. Each GST fusion protein was incubated with either His-Tda2 (wild-type) or His-Tda2 containing a single amino acid mutation. Bound proteins were analyzed by Coomassie staining. Mutating amino acids W96, D101, and L124 of Tda2 resulted in a significant decrease in interaction with Aim21, while mutating amino acids F86, I103 and K107 had little or no effect. (F) A fluorescence polarization assay was performed using 10nM FITC-Aim21 and various concentrations of His-Tda2 (WT) or Tda2 mutants (F86V and D101A). Data points represent the average and standard deviation from a single experiment performed in triplicate. Dissociation constants represent the mean  $\pm$  SEM of data from 3 independent experiments each fit to a two-site binding isotherm. ND = not determined.

residues (**Figure 2.4D bottom**). GST-Aim21<sup>510-555</sup> was immobilized on glutathione Sepharose resin, and subsequently incubated with each of the His-Tda2 mutants. SDS-PAGE analysis of bound proteins indicated that the mutations made along the canonical binding groove (F86V, I103Q and K107E) had little effect on the Tda2-Aim21 interaction (Figure 2E, S3A). In contrast, mutations made at the hydrophobic top face (W96H, D101A, D101N and L124N) had a pronounced decrease in binding (**Figure 2.4E, 2.5A**). To confirm the results of the GST-pulldown in a more quantitative assay, the F86V and D101A mutants were utilized in our fluorescence polarization assay. Consistent with the pulldown results, the F86V mutation had a subtle effect on binding, whereas the D101A mutation displayed little binding to FITC-Aim21 (**Figure 2.4F**). Size-exclusion chromatography indicated that neither mutation affected Tda2 homodimer formation (**Figure 2.5B**). Together, these results suggest that Tda2 interacts with Aim21 at a site different from the canonical binding groove described in other DLCs.

### 2.3.3 The Tda2-Aim21 interaction is essential for recruitment and function of Tda2 during CME

Having identified mutations that disrupt the Tda2-Aim21 complex *in vitro*, we next assessed how these mutations affect the recruitment of each protein to CME sites *in vivo*. Previously, it was shown that Tda2-GFP was not recruited to endocytic patches in cells carrying a deletion of the *AIM21* gene (*aim21Δ*) [83]. To test whether disrupting the Tda2-Aim21 interaction had a similar effect, the mutant alleles *aim21*<sup>533,536A</sup> and *tda2*<sup>D101A</sup> were each integrated at their endogenous loci in *TDA2-GFP* cells. Live cell imaging demonstrated that in both cases, the phenotype matched that of *aim21Δ* cells, with a total loss in Tda2-GFP and Tda2<sup>D101A</sup>-GFP localization, respectively (**Figure 2.6A**). Importantly, immunoblotting of total cell extract showed expression levels of Tda2-GFP and Tda2<sup>D101A</sup>-GFP in mutant strains was comparable to that in control cells (**Figure 2.7A**). Conversely, recruitment of Aim21-GFP to endocytic sites was shown to be diminished but not abolished in cells carrying a deletion of the *TDA2* gene (*tda2Δ*) [83].

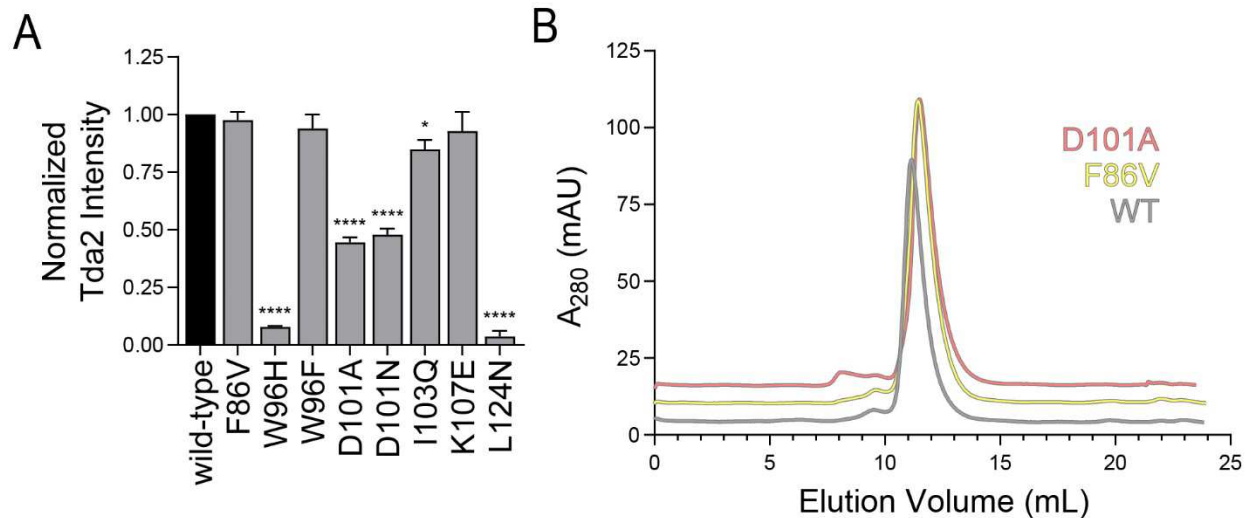


**Figure 2.5: Tda2 mutations do not affect dimerization.** (A) Quantification of GST-pulldown results in Figure 2E,  $n = 3$  independent experiments. Error bars, mean with standard deviation.  $*P \leq .05$ ,  $****P \leq 0.0001$ . (B) His-Tda2 (WT) and His-Tda2 mutants (F86V and D101A) were fractionated by size-exclusion chromatography on a Superdex Increase 75 column. Chromatograms are shown offset for clarity. The Tda2 mutants share similar elution profiles to the Tda2 dimer.

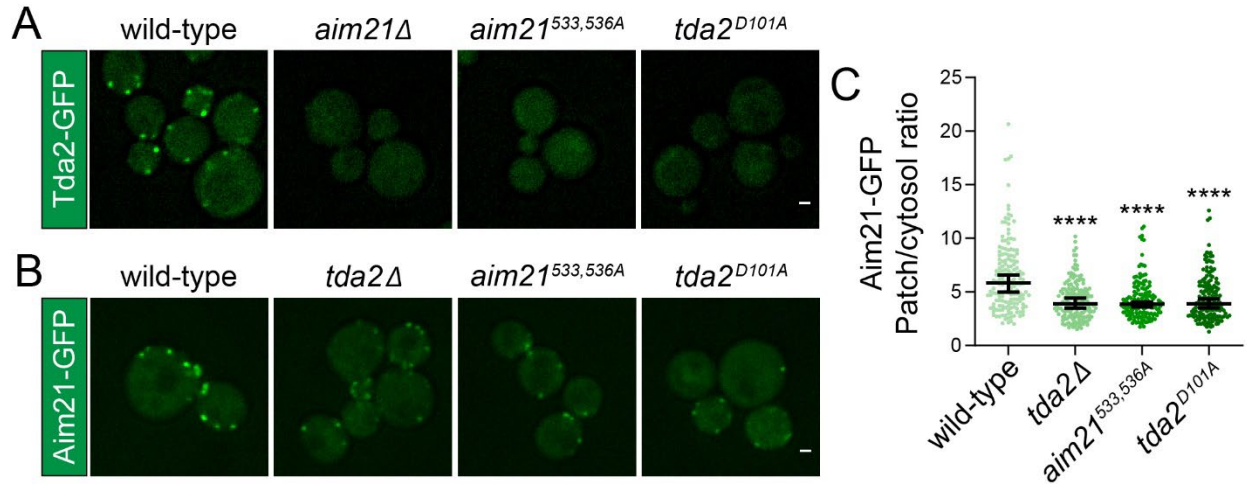


**Figure 2.6: Recruitment of Tda2 and Aim21 to endocytic sites is dependent on their interaction.** (A) Live-cell fluorescence microscopy showing no recruitment to endocytic sites of Tda2-GFP expressed from the endogenous locus in cells lacking Aim21 (SDY1291) or cells with a disrupted Tda2-Aim21 interaction (SDY1297 and SDY1466). Scale bar, 1  $\mu$ m. (B) Live-cell fluorescence microscopy showing reduced recruitment to endocytic sites of Aim21-GFP expressed from the endogenous locus in cells lacking Tda2 (SDY1290) or cells with a disrupted Tda2-Aim21 interaction (SDY1324 and SDY1467). Scale bar, 1  $\mu$ m. (C) Quantification of Aim21-GFP fluorescence intensity at endocytic patches in wild-type, *tda2*Δ, *aim21*<sup>533,536A</sup> and *tda2*<sup>D101A</sup> cells. From left to right, median patch/cytosol ratio = 5.85, 3.90, 3.87, 3.90 and n = 161, 162, 155, 164. Error bars, median with 95% CI. \*\*\*\**P* ≤ 0.0001.

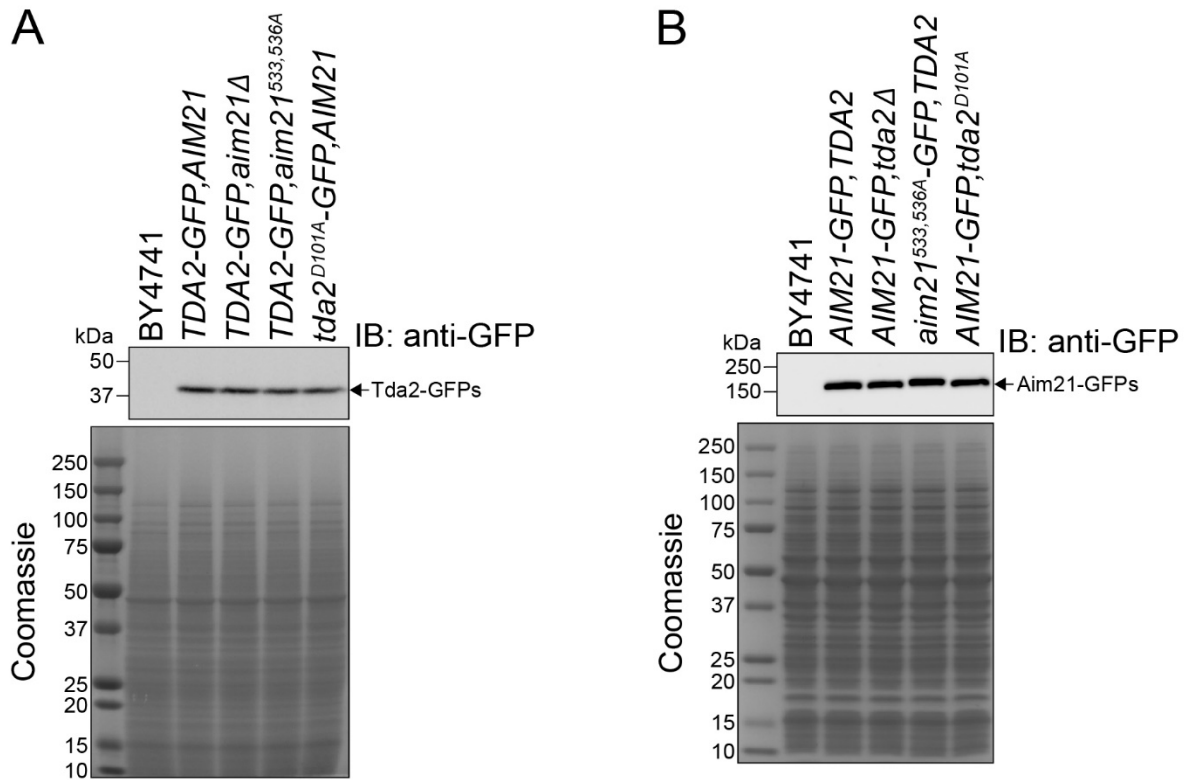


**Figure 2.7: Tda2-GFP and Aim21-GFP expression levels are unaffected by mutations.** (A, top) Cell extracts from Tda2-GFP strains used for fluorescence microscopy (Figure 3A) were analyzed by immunoblotting (IB) using antibodies to the GFP tag (anti-GFP). The parent strain, BY4741, is shown as a negative control. (Bottom) Coomassie-stained gel of extracts show equal loading. The strains display comparable expression of Tda2-GFP. (B) Cell extracts from Aim21-GFP strains used for fluorescence microscopy (Figure 3B) were analyzed as in Figure S2A. The strains display comparable expression of Aim21-GFP.

Here, the mutant alleles *aim21*<sup>533,536A</sup> and *tda2*<sup>D101A</sup> were each integrated at the corresponding endogenous locus in *AIM21-GFP* cells. Live cell imaging demonstrated the mutations caused a marked reduction of *aim21*<sup>533,536A</sup>-GFP and Aim21-GFP recruitment to endocytic sites, respectively (**Figure 2.6B**). Quantification of fluorescence intensity at endocytic sites showed such reduction parallels that of Aim21-GFP in *tda2*Δ cells (**Figure 2.6B,C**). Control immunoblotting experiments indicated that expression levels of Aim21<sup>533,536A</sup>-GFP and Aim21-GFP in mutant strains was similar to that of control cells (**Figure 2.7B**).

As Tda2 was wholly dependent on its interaction with Aim21 for localization to CME sites, we reasoned that cells with a disrupted Tda2-Aim21 interaction would display the same endocytic phenotype as *tda2*Δ cells. Previously, *tda2*Δ cells were shown to have a modest reduction in recruitment of actin capping protein (CP) compared to wild-type cells [83]. Consistent with this, *aim21*<sup>533,536A</sup> and *tda2*<sup>D101A</sup> cells displayed an equivalent reduction in Cap1-GFP recruitment levels at endocytic sites, as determined by live cell microscopy (**Figure 2.8A, 2.8B left**). Additionally, the lifetime of Cap1-GFP patches in mutant cells increased slightly compared to wild-type cells (**Figure 2.8B right**). Cells with a defect in capping protein recruitment show increased levels of the filamentous actin binding protein Abp1 at CME sites. Accordingly, both *tda2*Δ cells and cells lacking the Tda2-Aim21 interaction showed an appreciable increase in Abp1-GFP levels at endocytic sites (**Figure 2.8C, 2.8D left**). In addition to the increased recruitment, Abp1-GFP patches persisted longer, indicative of a less efficient actin network (**Figure 2.8D right**). Together these *in vivo* experiments corroborate mapping of the Tda2-Aim21 interaction performed with *in vitro* assays and indicate Tda2 functions in actin regulation at endocytic sites through its interaction with Aim21.

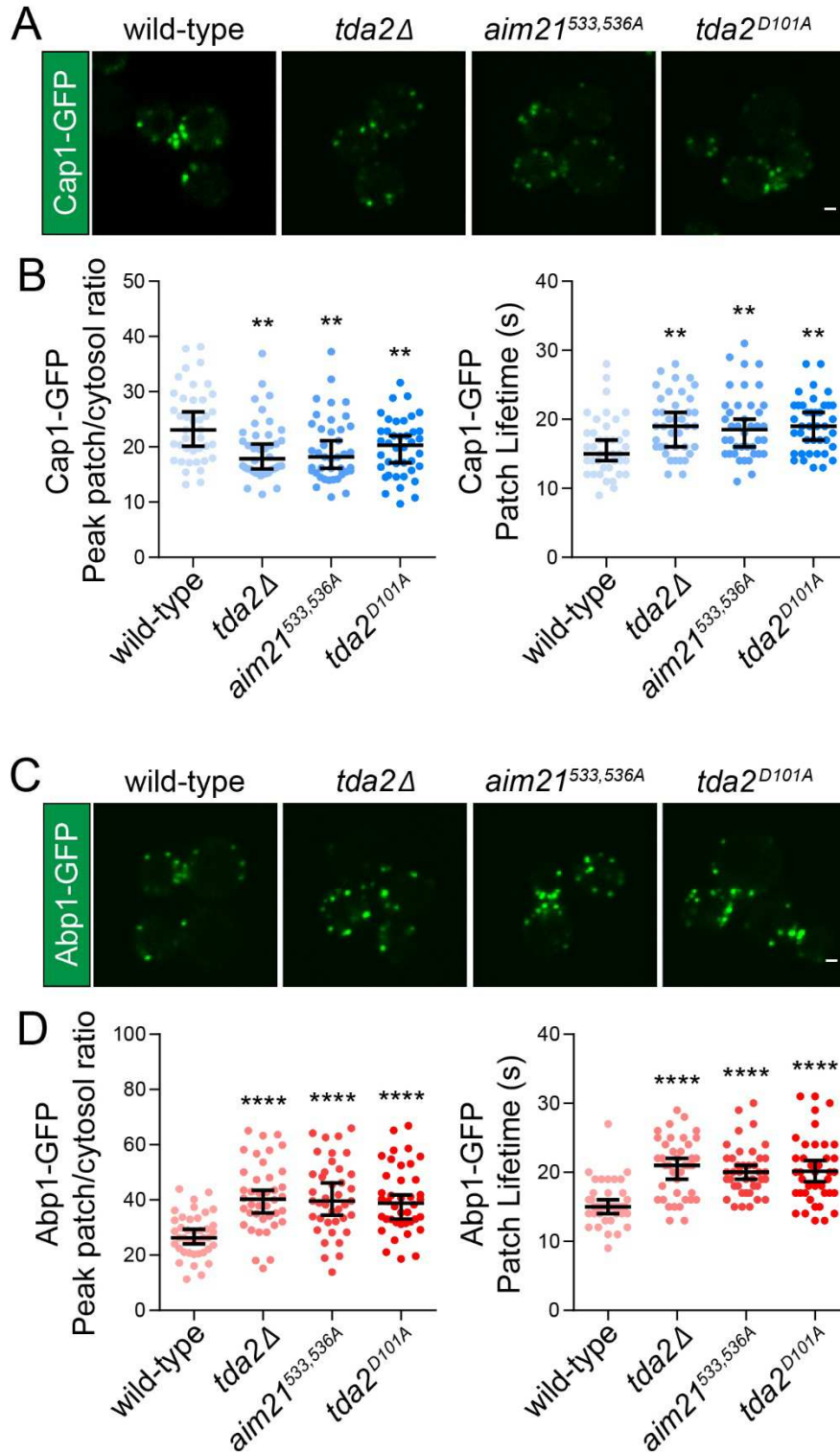


**Figure 2.8: Disruption of the Tda2-Aim21 interaction mimics the *tda2Δ* endocytic phenotype.** (A) Live-cell fluorescence microscopy showing reduced levels of Cap1-GFP at endocytic sites in cells lacking Tda2 (SDY1293) or cells with a disrupted Tda2-Aim21 interaction

(SDY1298 and SDY1468). Scale bar, 1  $\mu\text{m}$ . (B, left) Quantification of Cap1-GFP peak fluorescence intensity at endocytic patches in wild-type, *tda2* $\Delta$ , *aim21*<sup>533,536A</sup> and *tda2*<sup>D101A</sup> cells. From left to right, median peak patch/cytosol ratio = 23.1, 17.9, 18.2, 20.3 and n = 40 for all groups. (Right) Quantification of Cap1-GFP patch lifetime at endocytic patches in wild-type, *tda2* $\Delta$ , *aim21*<sup>533,536A</sup> and *tda2*<sup>D101A</sup> cells. From left to right, median patch lifetime = 15.0, 19.0, 18.5, 19.0 and n = 40 for all groups. Error bars, median with 95% CI. \*\* $P \leq 0.01$ . (C) Live-cell fluorescence microscopy showing increased levels of Abp1-GFP at endocytic sites in cells lacking Tda2 (SDY1295) or cells with a disrupted Tda2-Aim21 interaction (SDY1299 and SDY1469). Scale bar, 1  $\mu\text{m}$ . (D, left) Quantification of Abp1-GFP peak fluorescence intensity at endocytic patches in wild-type, *tda2* $\Delta$ , *aim21*<sup>533,536A</sup> and *tda2*<sup>D101A</sup> cells. From left to right, median peak patch/cytosol ratio = 26.3, 40.3, 39.6, 38.9 and n = 40 for all groups. (Right) Quantification of Abp1-GFP patch lifetime at endocytic patches in wild-type, *tda2* $\Delta$ , *aim21*<sup>533,536A</sup> and *tda2*<sup>D101A</sup> cells. From left to right, median patch lifetime = 15.0, 21.0, 20.0, 20.0 and n = 40 for all groups. Error bars, median with 95% CI. \*\*\*\* $P \leq 0.0001$ .

#### 2.3.4 *Tda2 functions as a dimerization engine for Aim21*

DLCs may function as dimerization hubs for their binding partners. Based on the above results, we hypothesized that the Tda2 homodimer may have such a function during yeast CME, helping to bring together two copies of Aim21. To determine if the reconstituted Tda2-Aim21 complex has a size consistent with this hypothesis, we performed size-exclusion chromatography using purified recombinant proteins. His-tagged Aim21, Aim21<sup>533,536A</sup> and Tda2 were fractionated on a Superose 6 column and the fractions were analyzed by SDS-PAGE. In addition to the purified recombinant proteins, six globular proteins with well-defined hydrodynamic radii were analyzed in parallel. His-Aim21 and His-Aim21<sup>533,536A</sup> had identical elution profiles, both eluting as species larger than the 443 kDa (61 Å) globular standard (**Figure 2.9A**). As His-Aim21 has a theoretical molecular weight of 76.0 kDa, Aim21 is either highly asymmetric, consistent with the prediction that Aim21 is a highly disordered protein, or is capable of forming homo-oligomers. The Tda2 homodimer eluted as a much smaller species than Aim21, consistent with its compact structure and molecular weight (**Figure 2.9A**). When His-Aim21 and His-Tda2 were combined at equimolar levels, the Tda2-Aim21 complex was successfully reconstituted, indicated by co-fractionation of the two proteins (**Figure 2.9A**). Notably, the elution volume indicated the hydrodynamic radius of the complex was larger than that of the 669 kDa (86 Å) standard (**Figure 2.9A**). The sizeable shift in elution volumes between Tda2-Aim21 and Aim21 could not be explained by the addition of a 31 kDa Tda2 homodimer to Aim21 alone, supporting the idea that Tda2 links multiple copies of Aim21. His-Aim21<sup>533,536A</sup> showed no co-fractionation with His-Tda2 upon incubation of the two proteins, confirming that the mutations abolish the Tda2-Aim21 interaction (**Figure 2.9A**).

These initial findings suggested Tda2 and Aim21 interact to form an asymmetric, elongated complex. To corroborate this, the proteins were fractionated in a 5-20% (w/v) sucrose gradient to separate samples based on density. Four globular standard proteins with known sedimentation coefficients (S) were analyzed in parallel. His-Aim21 and

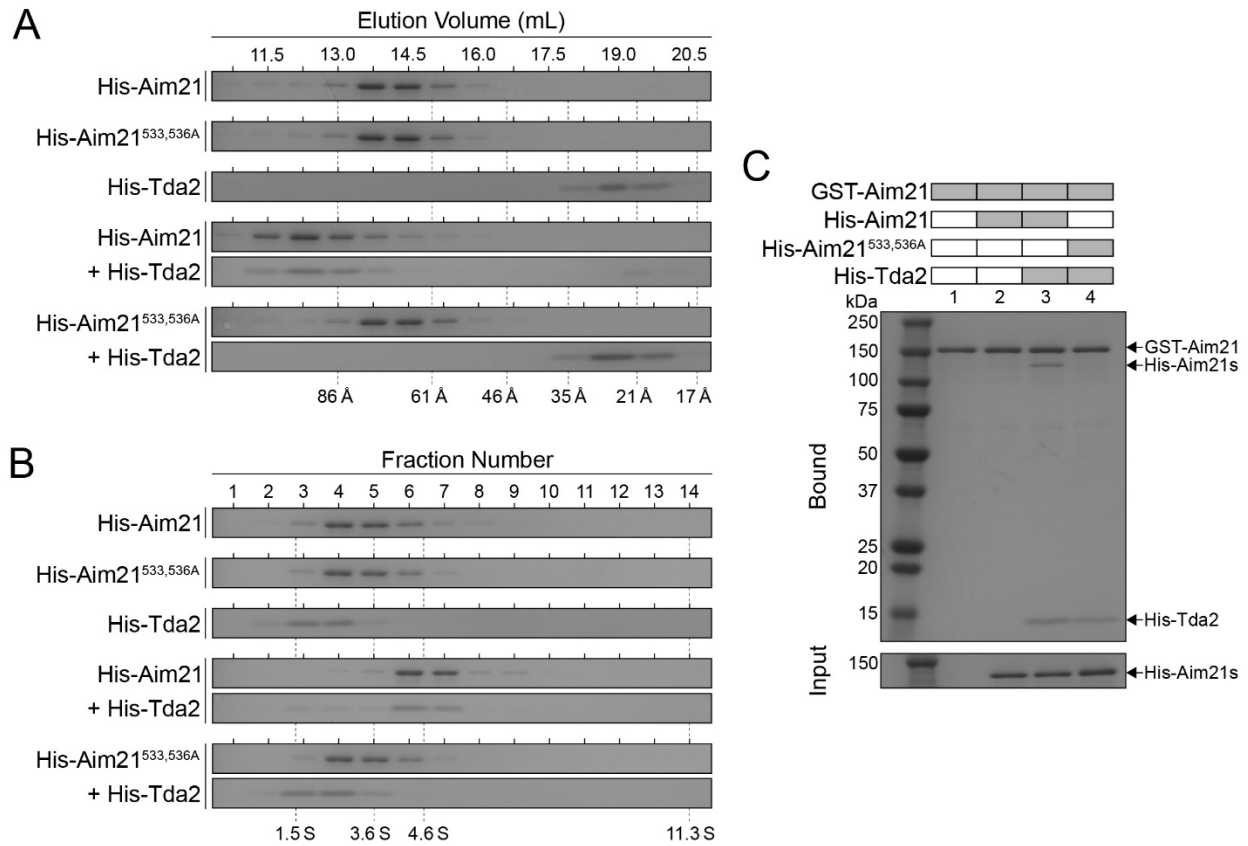


**Figure 2.9: Tda2 functions as a dimerization engine for Aim21.** (A) Purified recombinant His-Aim21 and His-Aim21<sup>533,536A</sup> were incubated with buffer alone or His-Tda2 and fractionated by size-exclusion chromatography on a Superose 6 column. Fractions were analyzed by SDS-PAGE. Stokes radii of six standard proteins are shown at the bottom. The reconstituted Tda2-Aim21 complex runs as a much larger complex than Aim21 alone. (B) Purified recombinant His-Aim21 and His-Aim21<sup>533,536A</sup> were incubated with buffer alone or His-Tda2 and fractionated in a 5-20% (w/v) linear sucrose gradient. Fractions were analyzed by SDS-PAGE. Sedimentation coefficients of four standard proteins are shown at the bottom. The reconstituted Tda2-Aim21 complex runs as a slightly larger complex than Aim21 alone. (C) A GST-pulldown assay was performed with GST fused to Aim21. GST fusion proteins were incubated with His-Aim21 alone (lane 2), His-Aim21 and His-Tda2 (lane3), or His-Aim21<sup>533,536A</sup> and His-Tda2 (lane 4). Bound proteins were analyzed by SDS-PAGE and Coomassie staining. GST-Aim21 only displayed an interaction with His-Aim21 in the presence of His-Tda2.

His-Aim21<sup>533,536A</sup> were concentrated in fractions 4 and 5, displaying a similar density to the 43 kDa (3.6 S) standard (**Figure 2.9B**). Tda2 eluted primarily in fractions 3 and 4, consistent with its molecular weight and fold (**Figure 2.9B**). When Aim21 and Tda2 were combined to reconstitute the Tda2-Aim21 complex, the proteins cofractionated in fractions 6 and 7, and the complex displayed a similar density to the 66 kDa (4.6 S) standard (**Figure 2.9B**).

Analysis of the size-exclusion chromatography and sucrose gradient fractionation data suggest the Tda2 homodimer interacts with two Aim21 molecules, resulting in a four-subunit complex. From our fractionation experiments, Stokes radii and sedimentation coefficients were estimated for Tda2, Aim21 and the Tda2-Aim21 complex, allowing us to calculate an experimental molecular weight (MW) for each species. Tda2 displayed an experimental MW of  $24.9 \pm 0.4$  kDa ( $27.2 \pm 0.3$  Å and  $2.3 \pm 0.1$  S), similar to the 31.1 kDa theoretical MW of the homodimer. Aim21 displayed an experimental MW of  $94.6 \pm 5.6$  kDa ( $79.5 \pm 2.2$  Å and  $2.9 \pm 0.1$  S), in line with the 76.0 kDa theoretical MW of an Aim21 monomer. Lastly, the experimental MW of the Tda2-Aim21 complex was  $206.5 \pm 7.9$  kDa ( $108.4 \pm 0.9$  Å and  $4.7 \pm 0.1$  S). This MW compares nicely with the 183.0 kDa theoretical MW of a complex consisting of one Tda2 homodimer and two Aim21 molecules.

To further test if Tda2 could function as a dimerization factor for Aim21, a GST-pulldown assay was performed to assess if GST-fused Aim21 could interact with supplemental Aim21. GST-Aim21 was first immobilized on glutathione resin, then incubated with His-tagged Aim21 (His-Aim21 or His-Aim21<sup>533,536A</sup>). GST-Aim21 did not pulldown His-Aim21 when Tda2 was not present (**Figure 2.9C lane 2**). When GST-Aim21 was incubated with both His-Tda2 and His-Aim21, the supplemental Aim21 was now pulled down (**Figure 2.9C lane 3**). When His-Aim21<sup>533,536A</sup> was used in place of wild-type His-Aim21, it was no longer pulled down by GST-Aim21 despite the presence of His-Tda2 (**Figure 2.9C lane 4**). The data are consistent with the idea that formation of the Tda2-Aim21 complex is reliant upon the ability of two Aim21

molecules to interact directly with the Tda2 homodimer, thus supporting the proposed function of Tda2 as a dimerization engine for Aim21.

### 2.3.5 Chemical dimerization of Aim21 rescues *tda2*Δ endocytic phenotype

Previously, we demonstrated *tda2*Δ cells have a phenotype characterized by decreased recruitment of Aim21 and increased levels of Abp1, indicative of an overgrown actin network at CME sites (**Figure 2.6, 2.8**). As our *in vitro* data supports Tda2 acting as a dimerization engine for Aim21, we reasoned that artificial dimerization of Aim21 could rescue the *tda2*Δ phenotype.

To test this, we utilized a chemically induced dimerization system consisting of FK506 binding protein (FKBP) and the bivalent chemical AP20187, which induces homodimerization of FKBP [152-155]. Yeast strains were engineered to express Abp1-mCherry and full-length Aim21 tagged with both FKBP and GFP (Aim21<sup>FL</sup>-FKBP-GFP) from their endogenous loci. Incorporation of the FKBP tag did not affect Aim21-GFP expression or patch dynamics, as Aim21-GFP and Aim21<sup>FL</sup>-FKBP-GFP were expressed at comparable levels and displayed equivalent patch lifetimes (**Figure 2.10A, 2.10B**). In cells with functional Tda2 (*TDA2*), treatment with AP20187 did not affect recruitment of Aim21<sup>FL</sup>-FKBP-GFP when compared to the vehicle (EtOH) control (**Figure 2.11A top, 2.11B**). Additionally, Abp1-mCherry levels at CME sites were indistinguishable between the AP20187 and EtOH groups (**Figure 2.11A top, 2.11C**). As expected, *tda2*Δ cells showed diminished Aim21<sup>FL</sup>-FKBP-GFP recruitment and increased Abp1-mCherry levels with vehicle alone (**Figure 2.11A middle, 2.11B, 2.11C**). Interestingly, upon incubation with AP20187, *tda2*Δ cells displayed a marked increase in Aim21<sup>FL</sup>-FKBP-GFP recruitment (**Figure 2.11A middle, 2.11B**). While chemical dimerization of Aim21 resulted in nearly a full rescue of its recruitment to endocytic sites, rescue of the Abp1-mCherry level at endocytic sites was partial (**Figure 2.11A middle, 2.11C**).

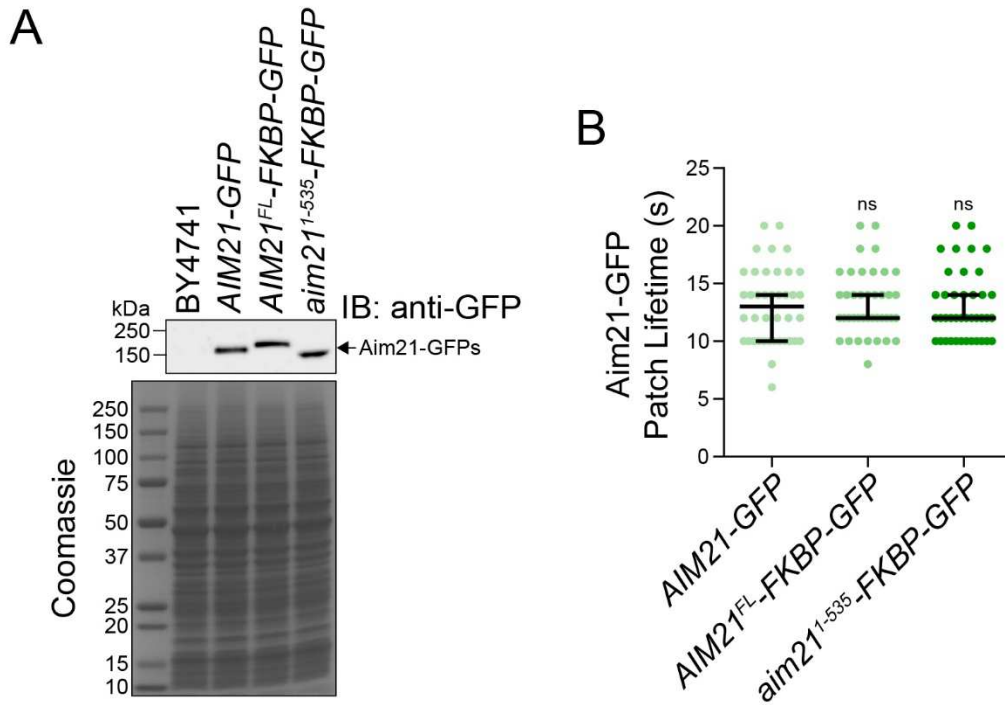


**Figure 2.10: Tagging Aim21 with FKBP does not affect expression level or patch lifetime.**

(A, top) Cell extracts from *AIM21-FKBP-GFP* strains used for fluorescence microscopy (Figure 6A) were analyzed by immunoblotting (IB) using antibodies to the GFP tag (anti-GFP). The parent strain, BY4741, is shown as a negative control. (Bottom) Coomassie-stained gel of extracts show equal loading. Aim21-FKBP-GFP expressing strains display comparable expression with Aim21-GFP. (B) Quantification of Aim21-GFP, Aim21<sup>FL</sup>-FKBP-GFP and Aim21<sup>1-535</sup>-FKBP-GFP patch lifetimes showing the FKBP tag does not affect Aim21 dynamics at endocytic sites. From left to right, median patch lifetime = 13.0, 12.0, 12.0 and  $n = 40$  for all groups. Error bars, median with 95% CI. ns  $P > 0.05$ .

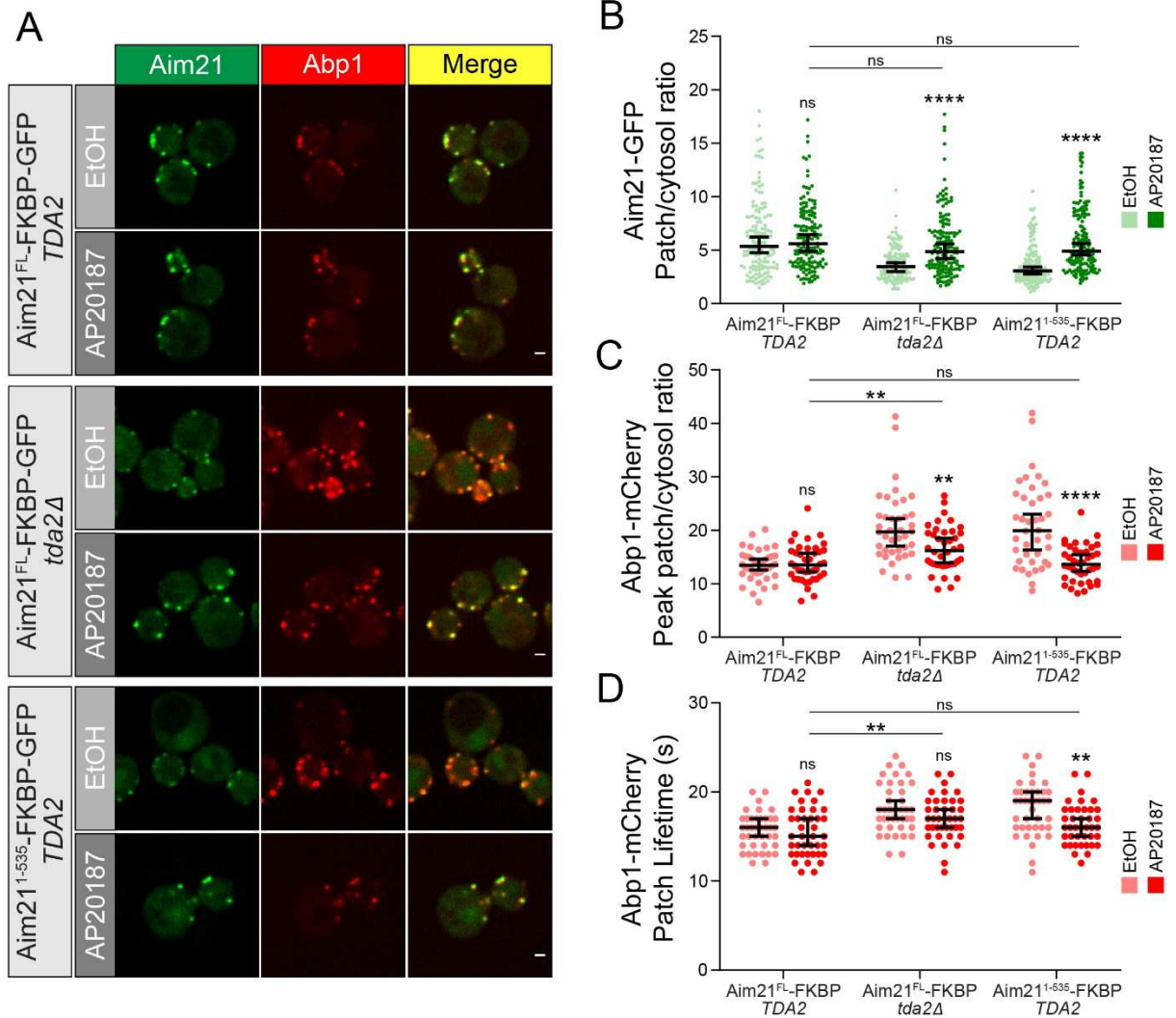


**Figure 2.11: Chemically induced dimerization of Aim21 rescues the phenotype of *tda2Δ* cells.** (A) Yeast strains were created to express Abp1-mCherry and Aim21 tagged with both FKBP and GFP (Aim21<sup>FL</sup>-FKBP-GFP or Aim21<sup>1-535</sup>-FKBP-GFP) from their endogenous loci. Prior to imaging, cells were incubated with EtOH (vehicle) or AP20187 (FKBP dimerizer). (Top) Live-cell fluorescence microscopy of cells expressing Aim21<sup>FL</sup>-FKBP-GFP and Tda2 (SDY1377) showing no change in levels of Aim21<sup>FL</sup>-FKBP-GFP and Abp1-mCherry upon treatment with AP20187. (Middle) Cells expressing Aim21<sup>FL</sup>-FKBP-GFP but lacking Tda2 (SDY1378) display an increase in Aim21<sup>FL</sup>-FKBP-GFP and a decrease in Abp1-mCherry patch intensity levels upon treatment with AP20187. (Bottom) Cells expressing Aim21<sup>1-535</sup>-FKBP-GFP and Tda2 (SDY1431) display an increase in Aim21<sup>1-535</sup>-FKBP-GFP and a decrease in Abp1-mCherry patch intensity upon treatment with AP20187. Note the similarities between AP20187 groups in the three panels. Scale bars, 1  $\mu$ m. (B) Quantification of Aim21<sup>FL</sup>-FKBP-GFP and Aim21<sup>1-535</sup>-FKBP-GFP fluorescence intensity at endocytic patches showing chemical dimerization of Aim21 can rescue the defect in Aim21 recruitment seen in cells lacking a Tda2-Aim21 complex. From left to right, median patch/cytosol ratio = 5.36, 5.61, 3.46, 4.98, 3.07, 4.91 and n = 138, 146, 131, 146, 141, 158. Error bars, median with 95% CI. ns  $P > 0.05$ , \*\*\*\* $P \leq 0.0001$ . (C)

Quantification of Abp1-mCherry peak fluorescence intensity at endocytic patches showing chemical dimerization of Aim21 can rescue the increased levels of Abp1 recruitment seen in cells lacking a Tda2-Aim21 complex. From left to right, median peak patch/cytosol ratio = 13.5, 13.5, 19.7, 16.2, 20.0, 13.6 and  $n = 40$  for all groups. Error bars, median with 95% CI. ns  $P > 0.05$ , \*\* $P \leq 0.01$ , \*\*\*\* $P \leq 0.0001$ . (D) Quantification of Abp1-mCherry patch lifetime showing chemical dimerization of Aim21 can rescue the increased Abp1 patch lifetime seen in cells lacking a Tda2-Aim21 complex. From left to right, median patch lifetime = 16.0, 15.0, 18.0, 17.0, 19.0, 16.0 and  $n = 40$  for all groups. Error bars, median with 95% CI. ns  $P > 0.05$ , \*\* $P \leq 0.01$ .

Strikingly, cells expressing Aim21<sup>1-535</sup>-FKBP-GFP, with the dimerizing element placed at the Tda2 binding region of a C-terminal truncated Aim21, exhibited a full rescue of the phenotype upon AP20187 treatment, with both Aim21<sup>1-535</sup>-FKBP-GFP and Abp1-mCherry recruitment levels comparable to wild-type cells (**Figure 2.11A bottom, 2.11B, 2.11C**). Examining the patch lifetime of Abp1-mCherry showed the same trend, with cells expressing Aim21<sup>1-535</sup>-FKBP-GFP displaying a more complete rescue than Aim21<sup>FL</sup>-FKBP-GFP expressing cells upon FKBP dimerization (**Figure 2.11D**). Together, these findings suggest that Tda2 functions as a dimerization engine for Aim21 *in vivo*, which is necessary for normal actin polymerization during endocytosis.

### 2.3.6 *Aim21 contains a capping protein interaction motif*

Given the direct physical interaction of the Tda2-Aim21 complex with CP [83], we reasoned that Tda2 or Aim21 may contain a capping protein-interacting (CPI) motif that facilitates the interaction. When we analyzed the primary amino acid sequence of Aim21 against the consensus CPI motif sequence [114, 116], two potential CPI motifs were identified. To test whether either of these regions were responsible for the interaction with CP, a GST pulldown experiment was performed with GST fused to wild-type Aim21 or Aim21 harboring point mutations to the potential CPI motif. In each mutant, three closely positioned basic residues, which are prevalent in CPI motifs, were mutated to glutamic acid. GST-Aim21 and the mutants (GST-Aim21<sup>504,507,509E</sup> and GST-Aim21<sup>564,566,573E</sup>) were immobilized on glutathione resin, and subsequently incubated with His-Tda2 and His-Cap1/2. While both mutants showed interaction with Tda2, GST-Aim21<sup>504,507,509E</sup> displayed no interaction with CP, suggesting the mutated region contained a CPI motif (**Figure 2.12A**). Notably, the region containing the potential CPI motif in Aim21, spanning amino acids 495-515, lies directly adjacent to the Tda2 binding region (**Figure 2.12B**).

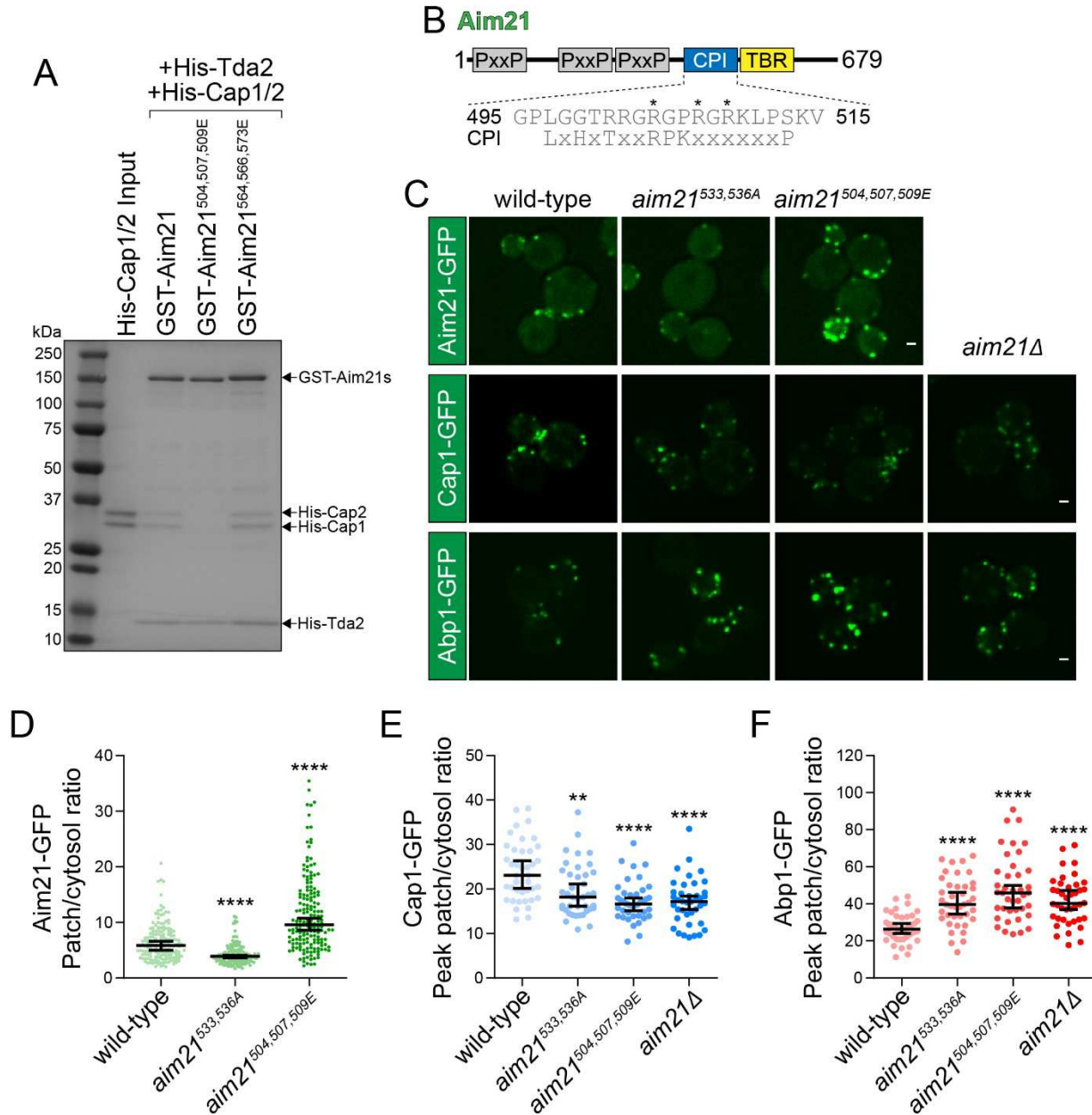


**Figure 2.12: Aim21 contains a capping protein interacting (CPI) motif.** (A) A GST-pulldown assay was performed with GST fused to Aim21. The GST-Aim21 fusions either contained no mutations or contained three basic residues mutated to glutamic acid in potential CPI motifs of Aim21 (GST-Aim21<sup>504,507,509E</sup> and GST-Aim21<sup>564,566,573E</sup>). Each GST fusion protein was incubated with His-Tda2 and His-Cap1/2, and bound proteins were analyzed by SDS-PAGE and Coomassie staining. The GST-Aim21<sup>504,507,509E</sup> mutant displayed a significant decrease in binding with His-Cap1/2 compared to GST-Aim21 or GST-Aim21<sup>564,566,573E</sup>. (B) Organization of Aim21 Domains. PxxP = Polyproline motif-rich region. CPI = capping protein interacting motif. TBR = Tda2 binding region. The CPI motif sequence spanning amino acids 495-515 is shown below Aim21, with residues that were mutated to disrupt the Aim21-capping protein interaction denoted with an asterisk. The consensus CPI motif sequence that has been described

previously is shown for comparison. (C, top) Live-cell fluorescence microscopy showing reduced recruitment of Aim21-GFP to endocytic sites in cells with a disrupted Tda2-Aim21 interaction (SDY1324). In contrast, cells lacking the Aim21-capping protein interaction (SDY1472) display an increase in Aim21-GFP patch intensity. (Bottom) Live-cell fluorescence microscopy showing decreased recruitment of Cap1-GFP and increased recruitment of Abp1-GFP to endocytic sites in cells lacking the Aim21-Tda2 interaction (SDY1298 and SDY1299), the Aim21-capping protein interaction (SDY1474 and SDY1434) and Aim21 (SDY1292 and SDY1294). Scale bars, 1  $\mu$ m. (D) Quantification of Aim21-GFP fluorescence intensity at endocytic patches in wild-type, *aim21*<sup>533,536A</sup> and *aim21*<sup>504,507,509E</sup> cells. From left to right, median patch/cytosol ratio = 5.85, 3.87, 9.58 and n = 161, 155, 170. Error bars, median with 95% CI. \*\*\*\**P* ≤ .0001. (E) Quantification of Cap1-GFP peak fluorescence intensity at endocytic patches in wild-type, *aim21*<sup>533,536A</sup>, *aim21*<sup>504,507,509E</sup> and *aim21*Δ cells. From left to right, median peak patch/cytosol ratio = 23.1, 18.2, 16.6, 17.2 and n = 40 for all groups. Error bars, median with 95% CI. \*\**P* ≤ .01, \*\*\*\**P* ≤ .0001. (F) Quantification of Abp1-GFP peak fluorescence intensity at endocytic patches in wild-type, *aim21*<sup>533,536A</sup>, *aim21*<sup>504,507,509E</sup> and *aim21*Δ cells. From left to right, median peak patch/cytosol ratio = 26.3, 39.6, 46.0, 40.2 and n = 40 for all groups. Error bars, median with 95% CI. \*\*\*\**P* ≤ .0001.

We next wanted to test if the potential CPI motif of Aim21 was functionally relevant *in vivo*. Previously, we reported that recruitment of the Tda2-Aim21 complex to the actin network at endocytic sites depends at least in part on Aim21 interaction with Bbc1 [83]. Furthermore, while deletion of *TDA2* or *AIM21* resulted in lower levels of CP at sites of endocytosis, deletion of *CAP1* caused higher levels of Tda2-Aim21 complex at endocytic sites, suggesting the Tda2-Aim21 complex helps recruit CP rather than the converse model [83]. Interestingly, when mutations to disrupt the Aim21 CPI motif were integrated into the genome of *AIM21-GFP* cells (*aim21*<sup>504,507,509E</sup>-*GFP*), Aim21 displayed a different recruitment phenotype compared to cells unable to form the Tda2-Aim21 complex (*aim21*<sup>533,536A</sup>-*GFP*, Figure 7C). While Aim21<sup>533,536A</sup>-GFP had a deficit in recruitment to endocytic sites, Aim21<sup>504,507,509E</sup>-GFP had a significant increase in recruitment (**Figure 2.12C top, 2.12D**). This is probably due to a larger than normal actin network in *aim21*<sup>504,507,509E</sup> cells (see below). Importantly, this difference was not due to a change in expression levels between Aim21-GFP, Aim21<sup>533,536A</sup>-GFP and Aim21<sup>504,507,509E</sup>-GFP (**Figure 2.13**). Most importantly and consistent with the idea that Aim21 residues 495-515 define a CPI motif, *aim21*<sup>504,507,509E</sup> cells showed a deficit in Cap1-GFP recruitment to sites of endocytosis (**Figure 2.12C middle, 2.12E**). The defect in Cap1-GFP recruitment was more pronounced in *aim21*<sup>504,507,509E</sup> cells than in *aim21*<sup>533,536A</sup>, with *aim21*<sup>504,507,509E</sup> cells exhibiting a similar defect to those lacking Aim21 (*aim21*Δ, **Figure 2.12C middle, 2.12E**). Lastly, Abp1-GFP levels were significantly elevated in *aim21*<sup>504,507,509E</sup> cells, consistent with an overgrown actin network at CME sites (**Figure 2.12C bottom, 2.12F**). Together, these results suggest the CPI motif identified in Aim21 is important for regulation of capping protein localization and function at CME sites. Moreover, the fact that the Abp1-GFP phenotype is not more severe in *aim21*Δ cells than in *aim21*<sup>504,507,509E</sup> cells suggests the negative regulation of Aim21 on actin assembly at endocytic sites is mostly dependent on its interaction with CP.

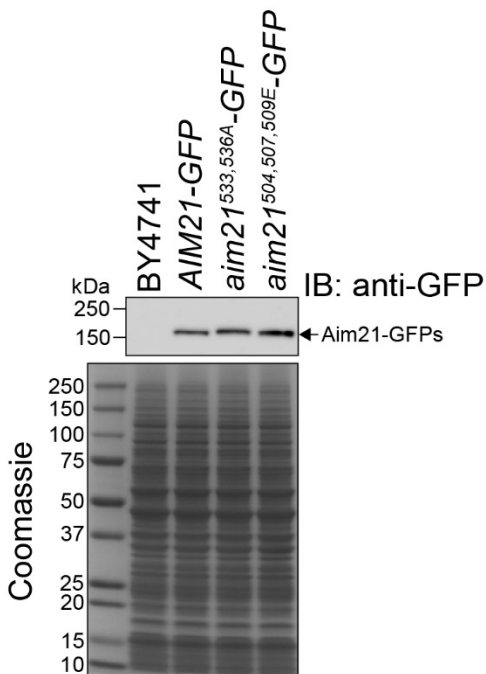


**Figure 2.13: Aim21-GFP expression level is unaffected by mutation to its CPI motif.** Cell extracts from Aim21-GFP strains used for fluorescence microscopy (Figure 7C) were analyzed by immunoblotting (IB) using antibodies to the GFP tag (anti-GFP). The parent strain, BY4741, is shown as a negative control. (Bottom) Coomassie-stained gel of extracts show equal loading. The strains display comparable expression of Aim21-GFP.

### 2.3.7 *Dimerization of Aim21 near CPI motif facilitates interaction with actin capping protein*

Having determined the CPI motif of Aim21 facilitates interaction of the Tda2-Aim21 complex with CP, we next wanted to examine the interaction of Aim21 with CP in a more quantitative fashion. To determine the binding affinity between Aim21 and CP, a fluorescence polarization assay was performed. A FITC-labelled Aim21 peptide containing both the CPI motif and Tda2 binding region of Aim21 (FITC-Aim21<sup>CPI+TBR</sup>) was titrated with various concentrations of CP, and fluorescence polarization values were measured. The data were fit to a one-site binding model, yielding a  $K_d$  value of  $3.1 \pm 0.2 \mu\text{M}$  (**Figure 2.14A**). To determine the effect of reconstitution of the Tda2-Aim21 complex on the binding affinity, the experiment was repeated in the presence of  $25 \mu\text{M}$  His-Tda2. Strikingly, the  $K_d$  value of the binding event decreased to  $250 \pm 13 \text{ nM}$ , representing a  $\sim 12$ -fold increase in binding affinity (**Figure 2.14A**). These data are consistent with previous findings from pulldown experiments, and together support the idea that Tda2 is necessary for the efficient interaction between Aim21 and CP.

Given the potential function of Tda2 as a dimerization engine for Aim21, we hypothesized that artificial dimerization of Aim21 could replicate the ability of the reconstituted Tda2-Aim21 complex to bind CP. To test this, we exploited the dimeric nature of the glutathione S-transferase tag in a GST pulldown assay using purified recombinant proteins. As GST is a strong parallel dimer, and its interaction with glutathione does not occur when in monomeric form, all GST fusion protein bound to glutathione resin will be dimeric fusion proteins. Accordingly, Aim21 was tagged with GST either at its N- or C-terminus, immobilized on glutathione Sepharose resin, and incubated with 6-histidine-tagged CP (His-Cap1/2 heterodimer). While the reconstituted Tda2-Aim21 complex displayed a robust interaction with capping protein, GST-Aim21 alone, dimerized by GST at its N-terminus, was not able to interact efficiently with CP (**Figure 2.14B lanes 1 and 2, 2.14C**). When the GST tag was flipped to the C-terminus of Aim21, Aim21 showed a modest interaction with CP, even in the absence of Tda2 (**Figure 2.14B lane 3, 2.14C**).

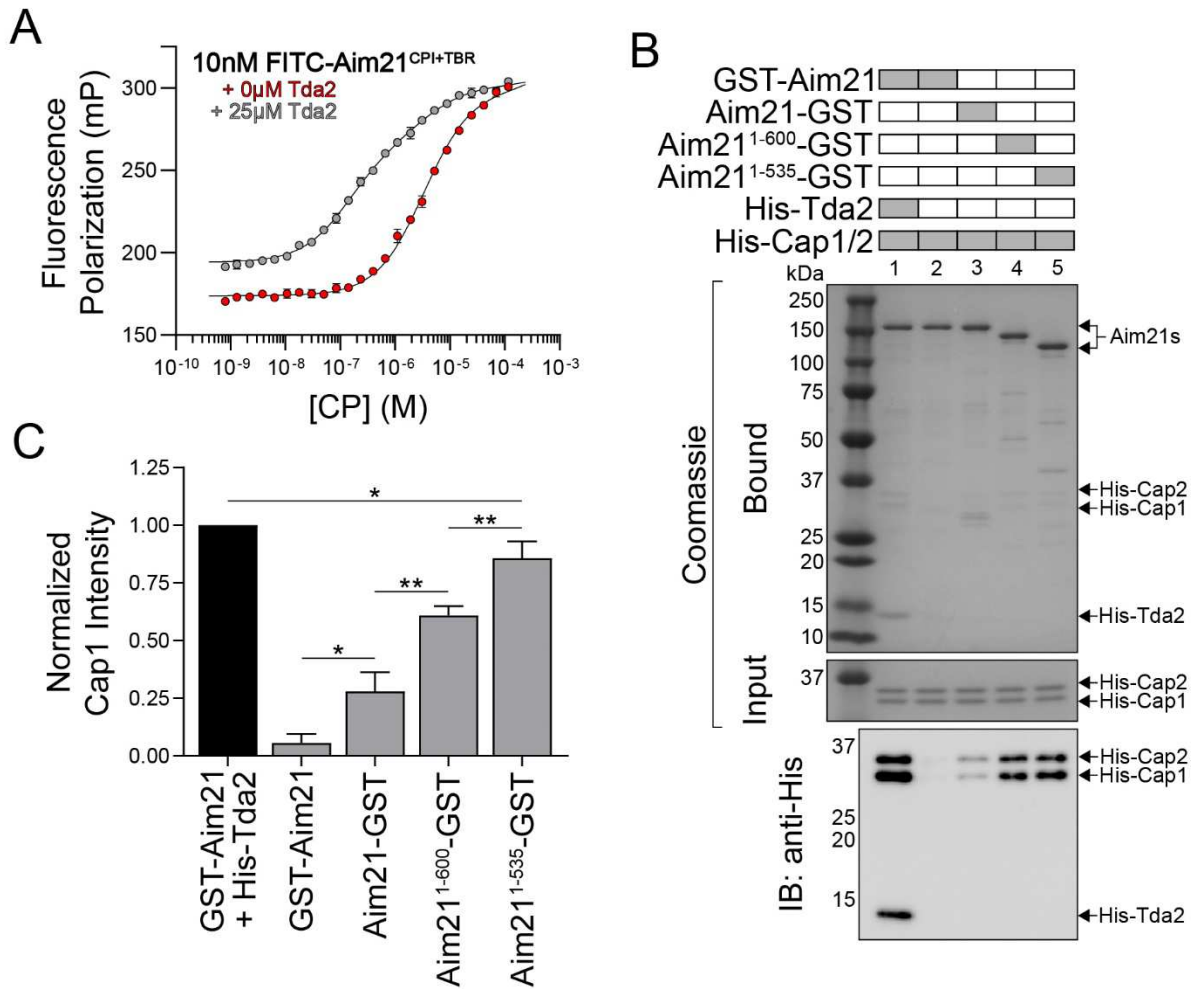


**Figure 2.14: Dimerization of Aim21 near CPI motif facilitates interaction with actin capping protein.** (A) A fluorescence polarization assay was performed using 10nM FITC-Labelled Aim21 peptide spanning amino acids 493-539 (FITC-Aim21<sup>CPI+TBR</sup>) and various concentrations of His-Cap1/2 (CP). Reactions either included 25  $\mu$ M His-Tda2 or lacked His-Tda2 (0  $\mu$ M). Data points represent the average and standard deviation from a single experiment performed in 3 technical replicates. Note that error is too small for many CP concentration data points to produce an error bar larger than the symbol. Dissociation constants represent the mean  $\pm$  SEM of data from 3 independent experiments fit to a one-site binding isotherm. (B) A GST-pulldown assay was performed with GST-Aim21 (lanes 1 and 2), Aim21-GST (lane 3), Aim21<sup>1-600</sup>-GST (Lane 4), and Aim21<sup>1-535</sup>-GST (lane 5). GST fusion proteins were incubated with either His-Cap1/2 alone (lanes 2, 3, 4 and 5) or His-Cap1/2 and His-Tda2 (lane 1). Bound proteins were analyzed by SDS-PAGE and Coomassie staining (top) and anti-His immunoblotting (bottom). Dimerization of Aim21 at its C-terminus by GST allowed for interaction with His-Cap1/2 at comparable levels to the reconstituted Tda2/Aim21 complex. (C) Quantification of normalized His-Cap1 intensity from GST-pulldown in Figure 8B, n = 3 independent experiments. Error bars, mean with standard deviation. \* $P \leq .05$ , \*\* $P \leq 0.01$ .

Notably, as Aim21 was truncated and the C-terminal GST tag was moved closer to the Tda2 binding region of Aim21 (AA 530-540), the degree of CP binding increased, showing optimal levels when the GST tag was placed at AA 535 (**Figure 2.14B lane 4 and 5, 2.14C**). Thus, dimerization of Aim21 at its C-terminus appears to facilitate the efficient interaction between Aim21 and CP, and this dimerization is most effective when located close to the CPI motif as it happens naturally for the Tda2 binding region of Aim21. Alternatively, it is possible that the position of the GST tag in the fusion protein may affect accessibility of the CPI motif to interact with CP.

## **2.4 Discussion**

The function of dynein light chains has been a subject of debate. Similarly, the molecular function of Tda2, the recently discovered *S. cerevisiae* TcTex1 DLC, is poorly understood. Unveiling the function of Tda2 would not only establish its role in yeast CME, but also provide insight into the function of DLCs in other eukaryotes. Here, we reveal that the Tda2 homodimer functions as a dimerization engine for Aim21 during CME. Tda2-induced dimerization of Aim21 in turn facilitates its localization and interaction with CP through a newly defined CPI motif in Aim21. The finding of a CPI motif in yeast suggests a conserved mechanism of CP regulation outside mammalian cells and the fact that it operates in endocytosis implies a broader function than previously appreciated [101].

DLCs have been suggested to function as hub proteins that induce dimerization of their numerous interacting partners [142, 146, 149-151]. Given this, we proposed a model in which Tda2 functions to bind to and induce dimerization of two Aim21 subunits. A number of our findings are in support of this model: A) Biochemistry indicates Aim21 itself is a monomer and thus is capable of being dimerized. B) Fluorescence polarization and GST-pulldown assays confirmed the Tda2 homodimer has the ability to bind two Aim21 subunits. C) The experimental molecular weight of the reconstituted Tda2-Aim21 complex was in agreement with the

theoretical molecular weight of a complex consisting of one Tda2 homodimer and two Aim21 molecules. D) The endocytic phenotype of *tda2Δ* cells was rescued by chemically induced dimerization of Aim21. Given that Tda2 is wholly dependent on its interaction with Aim21 for recruitment to endocytic sites, its role in dimerization and thus regulation of Aim21 may be the sole function it has in CME. Numerous proteins that interact with DLCs are also reported to contain domains capable of dimerization, such as coiled coils [142, 149-151]. Accordingly, we previously hypothesized that Tda2 could be inducing dimerization of Aim21 through a predicted coiled-coil near the N-terminus of Aim21 (residues 82-110). However, gel filtration and density gradient fractionation experiments indicated that this predicted coiled-coil does not mediate Aim21 dimerization and was unimportant for the formation and of the Tda2-Aim21 complex (**Figure 2.15**). While we cannot rule out that such a dimerizing element exists in Aim21, our study did not indicate that such a region was necessary.

The interaction between DLCs and their binding partners have largely been shown to occur through extension of the DLC  $\beta$ -sheet using symmetric binding grooves on opposite sides of the DLC dimers [149]. However, recent evidence has suggested that some TcTex1 members may have a non-canonical binding site in addition to the canonical binding groove, potentially allowing for formation of ternary complexes [156]. When analyzing the structure of Tda2, the canonical binding groove is partly occupied by the N-terminus of Tda2, which is extended in *S. cerevisiae* compared to the structures of TcTex1 from higher eukaryotes, suggesting an interaction between Tda2 and Aim21 in a canonical fashion is hindered [83, 148, 149]. In line with this, mutations to a hydrophobic pocket away from the canonical binding groove greatly affected the Tda2-Aim21 interaction, while mutations along the canonical binding groove had little effect. This suggests that the canonical binding mode for TcTex1 interactions is not conserved from yeast to mammals. Previously, DLCs associated with the dynein motor complex have

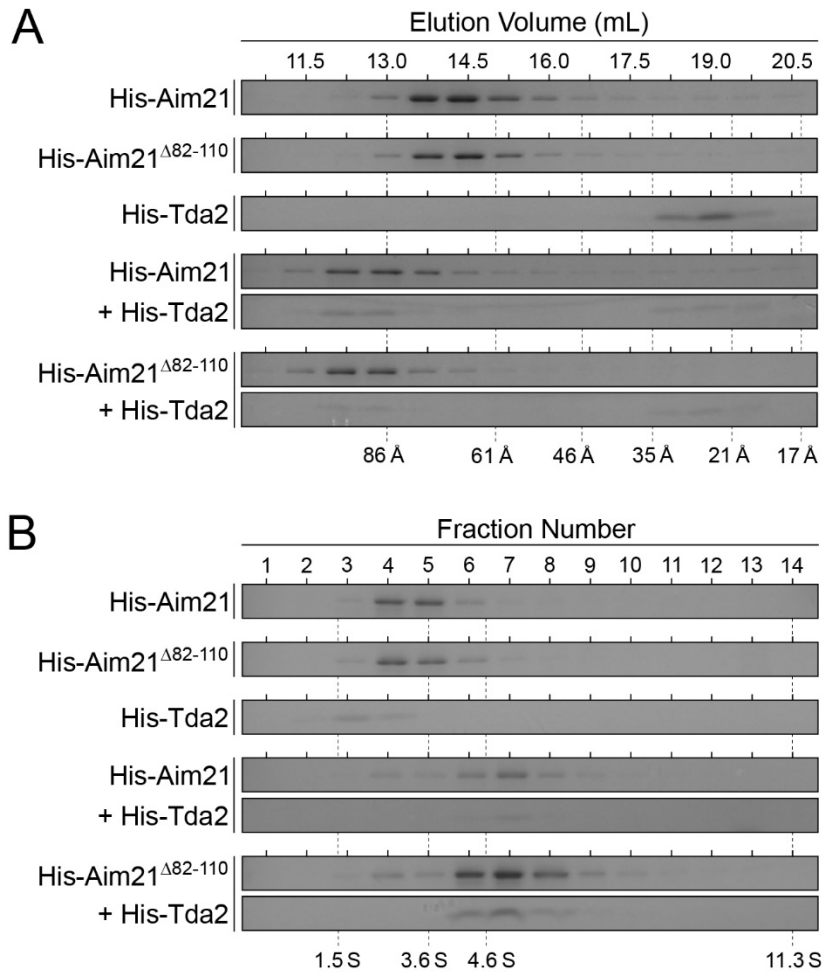


**Figure 2.15: Aim21 residues 82-110 with potential to form a coiled coil are not necessary for complex formation.** (A) Purified recombinant His-Aim21 and His-Aim21<sup>Δ82-110</sup> were incubated with buffer alone or His-Tda2 and fractionated by size-exclusion chromatography on a Superose 6 column. Fractions were analyzed by SDS-PAGE. Stokes radii of six standard proteins are shown at the bottom. Reconstitution of the Tda2-Aim21 complex does not depend on Aim21 residues 82-110. (B) Purified recombinant His-Aim21 and His-Aim21<sup>Δ82-110</sup> were incubated with buffer alone or His-Tda2 and fractionated in a 5-20% (w/v) linear sucrose gradient. Fractions were analyzed by SDS-PAGE. Sedimentation coefficients of four standard proteins are shown at the bottom. Reconstitution of the Tda2-Aim21 complex does not depend on Aim21 residues 82-110.

been proposed to function as cargo adaptors, with one binding site interacting with cargo and the other with the dynein intermediated chain. However, thermodynamic arguments oppose this function as the already dimeric DLCs would likely favor a dimeric binding partner [149, 151]. If a second binding site similar to the hydrophobic site of Tda2 were present in other TcTex1 DLCs, a cargo adaptor function would be plausible.

Is the Tda2-Aim21 complex constitutively assembled or dynamically assembled and disassembled *in vivo*? We previously performed gel filtration fractionation analysis of wild type yeast cytosol and observed two peaks for Tda2 [83]. The first peak corresponds to a cohort of Tda2 in complex with Aim21 and the second peak to the Tda2 homodimer. Deficiency of one subunit of a constitutively associated protein complex often results in destabilization of the other complex subunits. In contrast, we observed that deletion of *TDA2* did not destabilize Aim21 and, conversely, deletion of *AIM21* did not destabilize Tda2 as determined by immunoblotting of total cell extracts [83] (see also Figure S4). These results suggest Tda2-Aim21 may not necessarily form a constitutively associated complex. Further work will be needed to test this possibility and to elucidate any mechanism potentially regulating complex assembly/disassembly.

Our data suggest dimerization of Aim21 is not only critical for its proper localization during CME, but also its function. However, dimerization is only part of the equation, as dimerization of Aim21 specifically at the Tda2 binding region appears to be necessary for the full function of Aim21. While chemically induced dimerization of Aim21 at its C-terminus partially rescued the Abp1 defect in *tda2Δ* cells, dimerization at the Tda2 binding region of Aim21 resulted in a full rescue. Similarly, artificial dimerization of Aim21 at its C-terminus allowed for a weak interaction with CP *in vitro*, whereas artificial dimerization at residue 535 resulted in a stronger interaction. How could dimerization of

Aim21 be facilitating an efficient interaction with CP? First, it could be through an avidity effect. Given the proximity of the Tda2 binding region and CPI motif, dimerization of Aim21 would put two CPI motifs nearby, resulting in a bivalent ligand for CP. When CP dissociates from one of the Aim21 binding sites, the nearby binding site could subsequently rebind CP, limiting its diffusion, and resulting in an increased functional affinity. This possibility is supported by the increased affinity of CP for FITC-Aim21<sup>CPI+TBR</sup> in the presence of Tda2. Second, autoinhibition of Aim21 could prevent the Aim21-CP interaction, with Tda2-induced dimerization relieving the inhibition. This mechanism would require the Tda2-Aim21 interaction to be regulated on the same way. Lastly, Tda2 dimerization of Aim21 could lead to formation of secondary structure, which may be necessary for the Aim21-capping protein interaction. Opposing this idea, CPI motifs from higher eukaryotes are believed to be disordered in the absence of capping protein, and the CPI segment binds to the capping protein complex in an extended conformation that does not have any regular secondary structure. Regardless of the method, the idea that the CP-CPI motif interaction can be altered through allosteric regulation of the CPI motif had not previously been shown.

In mammalian cells, regulation of CP by a family of proteins containing CPI motifs has been demonstrated [101]. In addition to allosterically regulating the affinity of CP for the barbed end of actin filaments, some CPI motif containing-proteins have been shown to aid in localization of CP [102]. Given the relative simplicity of the yeast actin network, it was previously unknown whether CPI motifs were present in yeast. Our discovery of a functional CPI motif in Aim21 supports the notion that the binding of CP to actin filaments is a regulated event in yeast. Further supporting this idea, twinfilin, a protein involved in CME and conserved from yeast to humans, interacts with CP and was recently shown to contain a CPI motif in mice [123, 124, 126]. Given the experimentally tractable yeast endocytic actin network, the study of these CPI motif containing proteins in *S. cerevisiae* could help shed light on remaining questions about CP regulation. For instance, how twinfilin regulates CP is a subject of debate, with one report

proposing mammalian twinfilin has a pro-capping function while other studies provide evidence for uncapping function [126, 127, 157]. However, the function of twinfilin is complex as, at least *in vitro*, it can directly regulate filament barbed end dynamics independent of CP and either increase or decrease depolymerization rate depending on the nucleotide state of the barbed end actin subunits (ADP-P<sub>i</sub> vs. ADP) [158]. Additionally, our data with the Aim21 CPI motif mutant showing a decreased CP levels at endocytic sites supports the idea that Aim21 aids in recruitment of CP to the actin network at CME sites, similar to the role of CARMIL in higher eukaryotes at other cellular membranes [102]. Interestingly, besides regulation of CP to CME sites, Aim21 may also have a direct effect inhibiting actin filament barbed end elongation [85]. However, the fact that the increased Abp1-GFP levels at endocytic sites are not higher in *aim21*Δ cells compared with *aim21*<sup>504,507,509E</sup> cells suggests the main mechanism for Aim21 capping of actin filament barbed end is through CP. While our data support that the CPI motif of Aim21 is critical for its function and contributes to CP recruitment to sites of endocytosis, more work will be needed to fully understand how exactly it is regulating CP.

In conclusion, we have uncovered the molecular function of Tda2 as a dimerization engine for Aim21 during clathrin-mediated endocytosis in *S. cerevisiae*. Formation of the Tda2-Aim21 complex is essential for its interaction with, and regulation of capping protein, supporting the idea that regulation of capping protein through CPI motifs is conserved from yeast to humans.

## 2.5 Materials and Methods

### 2.5.1 Plasmids and yeast strains

All cloning was performed using the In-fusion HD Cloning System (Takara Bio Inc.). Plasmids for yeast two-hybrid analysis of Aim21 fragments were generated by PCR amplification of the corresponding DNA fragments of *AIM21* and cloned into pGBT9. Generation of pGAD424-Tda2 was described previously [83]. Generation of plasmids for bacterial expression of recombinant GST-Aim21 and His-Tda2 was described previously [83]. The plasmid for expression of recombinant GST-Aim21<sup>510-555</sup> was generated by PCR amplification of the corresponding *AIM21* DNA sequence and cloned into pGEX-5X-1. The plasmids for expression of recombinant His-Aim21, His-Cap1 and His-Cap2 were generated by PCR amplification of the corresponding DNA sequences of *AIM21*, *CAP1* and *CAP2* and cloned into pET30a(+). Plasmids for expression of recombinant Aim21 tagged at the C-terminus with GST (Aim21-GST) were generated by amplification of the GST encoding sequence from pGEX-5X-1 and cloned into pET30a(+)-*AIM21*, resulting in an N-terminal 6-histidine tagged and a C-terminal GST tagged protein. For fair comparison in this experiment, a 6-histidine tag was cloned into pGEX-5X-1-Aim21 at its C-terminus. All plasmids encoding mutant recombinant proteins were engineered by PCR-based mutagenesis using the In-fusion system. All constructs were verified by DNA sequencing.

For plasmids designed to integrate mutations into the *S. cerevisiae* genome, fragments containing the full ORF of either *AIM21* or *TDA2* plus 100 base pairs upstream and downstream were generated by PCR amplification from yeast genomic DNA and cloned into pUC18. PCR-based mutagenesis of pUC18-*AIM21* and pUC18-*TDA2* yielded the template for genetic manipulation. Plasmids for FKBP integration into the yeast genome were generated by PCR amplification of the DNA sequence encoding Aim21-GFP from the corresponding yeast GFP library strain (Invitrogen), then cloned into pUC18. Subsequently, the FKBP encoding sequence

was amplified from a gene block and cloned into pUC18-*AIM21-GFP* between the Aim21 and GFP encoding sequences.

The background *S. cerevisiae* strain BY4741 (*MATa*, *his3Δ1*, *leu2Δ0*, *met15Δ0*, *ura3Δ0*) was used throughout this study. Wild-type GFP-expressing strains (Tda2-GFP, Aim21-GFP, Cap1-GFP and Abp1-GFP) were obtained from the yeast GFP library (Invitrogen). Integration of mutant alleles was performed using a two-step gene replacement approach described previously [159]. As an example, SDY1297 (*MATa*, *his3Δ1*, *leu2Δ0*, *met15Δ0*, *ura3Δ0*, *TDA2-GFP::HIS3*, *aim21<sup>533,536A</sup>*) was created from the Tda2-GFP library strain (*MATa*, *his3Δ1*, *leu2Δ0*, *met15Δ0*, *ura3Δ0*, *TDA2-GFP::HIS3*). In step one, *URA3* was amplified from pRS316 [160] using primers that impart 50 base pairs of homology to the sequences directly upstream and downstream of the *AIM21* ORF, then transformed [161] into the Tda2-GFP library strain to generate intermediate strain SDY1291 (*MATa*, *his3Δ1*, *leu2Δ0*, *met15Δ0*, *ura3Δ0*, *TDA2-GFP::HIS3*, *aim21Δ::URA3*). Second, the intermediate strain SDY1291 was transformed with a DNA fragment containing the mutant allele *aim21<sup>533,536A</sup>*. Cells were grown overnight on plates containing rich media, then replica plated onto plates containing 5-fluoroorotic acid (5-FOA). Colonies that grew on plates containing 5-FOA represented cells in which the *aim21<sup>533,536A</sup>* allele replaced *URA3*. For FKBP strains used in the chemical induced dimerization experiment, BY4741 cells were first subjected to mCherry tagging of the *ABP1* ORF by PCR amplification of pFA6a-mCherry-HIS3MX6 and homologous recombination, followed by marker-less integration of *AIM21-FKBP-GFP* fragments using the two-step approach described. All integrants were verified by PCR of genomic DNA.

### 2.5.2 *Yeast two-hybrid assay*

AH109 cells were co-transformed with pGBT9 and pGAD424 vectors (Takara Bio Inc.) and grown on synthetic dropout media lacking leucine and tryptophan. Successful co-transformants were grown overnight in synthetic dropout media lacking leucine and tryptophan. The following day, cells were diluted to an O.D. 600 of 0.2 in sterile water. Diluted cells were spotted on synthetic dropout media lacking leucine and tryptophan (control), or lacking histidine in addition. 3-amino-1,2,4-triazole (3AT) was used to test for increased binding stringency.

### 2.5.3 *Biochemical Methods*

Recombinant 6-histidine (His) and GST fusion proteins were expressed in BL21 codon plus *E. coli* and purified using HisPur Cobalt Resin (Thermo Scientific) or Glutathione Sepharose 4 Fast Flow (GE Healthcare) as previously described [162]. Recombinant Aim21 proteins tagged with both His and GST at either terminus were first purified using Glutathione Sepharose 4 Fast Flow, and subsequently purified using HisPur Cobalt Resin. All proteins were dialyzed in PBS (137mM NaCl, 2.7mM KCl, 10mM Na<sub>2</sub>HPO<sub>4</sub>, 2mM KH<sub>2</sub>PO<sub>4</sub>)

GST pulldown assays were performed as previously described [163]. In short, recombinant GST-tagged proteins (10 µg) were incubated with glutathione Sepharose resin for 30 minutes at 4°C. Equimolar His-tagged protein was added and incubated for an additional 30 minutes. Resin was washed 3 times in PBS containing Triton X-100 (0.1-0.5%) and boiled in Laemmli sample buffer. Bound proteins were analyzed by SDS-PAGE and Coomassie staining and/or immunoblotting with anti-6xHis (Sigma). All pulldowns were repeated in an independent experiment to ensure reproducibility, and in 3 independent experiments if quantification was included. For quantification of pulldown experiments, ImageJ software was used for determining the intensity of protein bands. His-tagged protein band intensities were first normalized to the intensity of the immobilized GST protein, and next to the wild-type condition, depicted as a black

bar in figures. Statistical significance between groups was determined using an unpaired Student's *t* test (GraphPad Prism Software).

Fluorescence polarization assays were performed as previously described [59]. Briefly, 10nM of FITC-labelled Aim21 peptide was titrated with various concentrations of His-Tda2, His-Tda2 mutants and His-Cap1/2 in experiment buffer (137mM NaCl, 2.7mM KCl, 10mM Na<sub>2</sub>HPO<sub>4</sub>, 2mM KH<sub>2</sub>PO<sub>4</sub>, 0.01% Triton X-100, 2mM DTT). For the stoichiometry experiment (Figure 2C), 10μM FITC-Aim21 was utilized. FITC-Labelled Aim21 peptides FITC-KIEIFNNWNVS (FITC-Aim21), FITC-KIEAANNWNVS (FITC-Aim21\*) and FITC-KTGPLGGTRRGRGPRGRKLPKVASVEKIEEDDNTNKIEIFNNWNVS (FITC-Aim21<sup>CPI+TBR</sup>) were purchased from Thermo Fisher, Biomatik and GenScript, respectively. Data were collected using 384-well non-binding polystyrene microplates (Greiner Bio-one) in a Victor<sup>3</sup> V microplate reader (PerkinElmer) at room temperature following a 30-minute incubation. Three technical replicates were performed per experiment and each experiment was performed 3 independent times. The dissociation constants for each independent experiment were determined by curve fitting the data to either one-site or two-site binding isotherms using GraphPad Prism Software. The reported dissociation constants correspond to the average (and SEM) of values obtained in the 3 independent experiments.

Total yeast extracts were obtained as previously described [164]. Immunoblotting of cell extract was performed using anti-GFP (Sigma). For Aim21-GFP immunoblotting, transfer buffer was supplemented with 0.1% SDS for increased transfer efficiency of Aim21-GFP.

Size-exclusion chromatography for analysis of Tda2 and Tda2 mutants was performed on a Superdex 75 Increase 10/300 GL column (GE Healthcare) connected to a fast protein liquid chromatography system (GE Healthcare). The column was

equilibrated with PBS at 4°C, and elution of 0.5mg/mL protein sample was performed at a flow rate of 0.5 mL/min. Size-exclusion chromatography for analysis of the Tda2-Aim21 Complex was performed on a Superose 6 10/300 GL column (GE Healthcare) connected to a fast protein liquid chromatography system (GE Healthcare). The column was equilibrated with PBS at 4°C, and elution was performed at a flow rate of 0.4 mL/min with fractions collected every 750 µL. His-Aim21 was used at a concentration of 0.5mg/mL, and His-Tda2 was matched at an equimolar concentration. Fractions were mixed with Laemmli sample buffer and analyzed by SDS. The column was calibrated using blue dextran and a set of standard protein of known Stokes radii: cytochrome c (17 Å, 12kDa), carbonic anhydrase (21 Å, 29kDa), bovine serum albumin (35 Å, 66kDa), alcohol dehydrogenase (46 Å, 150kDa), apoferritin (61 Å, 443kDa) and thyroglobulin (86 Å, 669kDa). A standard curve was used for estimation of experimental Stokes radii.

Sucrose density linear gradients (5-20% w/v) were formed using a Gradient Master (BioComp). 200 µL of protein sample was layered on top of the gradient, and the samples were centrifuged in a SW 41 Ti rotor (Beckman Coulter) at 39,000 RPM for 18h at 4°C. 500 µL fractions were collected from the top of the test tube using a Piston Gradient Fractionator (BioComp Instruments). Fractions were analyzed by SDS-PAGE and Coomassie staining.

A set of standard proteins of known sedimentation coefficients (S) were analyzed for comparison: cytochrome c (1.5 S, 12kDa), ovalbumin (3.6S, 43 kDa), bovine serum albumin (4.6S, 66 kDa), bovine catalase (11.3S, 250 kDa). A standard curve was used for estimation of experimental sedimentation coefficients.

#### 2.5.4 *Fluorescence Microscopy*

Fluorescence microscopy was performed as previously described using an IX81 spinning-disk confocal microscope (Olympus) with a Cascade II camera (Photometrics) and a 100X 1.40 NA objective [164]. Briefly, cells grown overnight were diluted in synthetic complete

media and grown to early logarithmic phase, then imaged at room temperature. Time-lapse videos were generated by collecting an image each second for 90 seconds. Slidebook 6 software (Intelligent Imaging Innovations) was used for quantification of patch intensities and lifetimes. For Cap1-GFP, Abp1-GFP and Abp1-mCherry analysis, time-lapse videos were used for quantification of peak patch intensities and patch lifetimes. To avoid issues with photobleaching, Aim21-GFP analysis of patches was done using still images. For quantification of peak patch/cytosol ratios, masks were drawn over individual endocytic sites to track the average fluorescence of the patch over time. Average patch intensity, average cytosol intensity and average background intensity were recorded for the frame in which the average patch intensity was at its maximum. After subtracting the average background from both values, the values were divided to give the peak patch/cytosol ratio. For quantification of patch lifetimes, masks were drawn over individual endocytic patches to track the maximum fluorescence of each patch over time. Prior to quantification, a threshold fluorescence value was established for each fluorescently tagged protein to establish a start and finish value for the endocytic event. The patch lifetime was determined by counting the number of frames in which the maximum patch fluorescence was above the threshold value. Patch/cytosol ratios were calculated in the same manner as peak/patch cytosol ratios, but using still images. Statistical significance between groups was determined using a Mann-Whitney test for all microscopy data (GraphPad Prism Software). Representative images for groups that were directly compared were displayed with equal brightness and contrast settings.

The B/B homodimerizer AP20187 (Takara Bio Inc.) was utilized in a similar fashion as described previously. Briefly, cells were grown overnight in synthetic complete media. The following day, cells were diluted into fresh synthetic complete

media, and grown to early log phase. 90 minutes prior to imaging, 5  $\mu$ M AP20187 or an equal volume of EtOH was added to the cultures, and cells were imaged as described.

## CHAPTER 3

### CPI MOTIF PROTEINS REGULATE ACTIN CAPPING PROTEIN DURING YEAST ENDOCYTOSIS

#### 3.1 Summary

In budding yeast, clathrin-mediated endocytosis is dependent on the polymerization of a branched actin network to provide the force necessary for membrane invagination. A key regulator in branched actin network formation is actin capping protein (CP), which binds to the barbed end of actin filaments to prevent the addition or loss of actin subunits. CP is regulated by a diverse group of protein containing CP-interacting (CPI) motifs, but how these proteins work together to regulate CP is poorly understood. Here, we show that the yeast endocytic factors Aim21 and Bsp1 work together to recruit CP to the cortical actin network through their CPI motifs. In contrast, the well-conserved actin disassembly factor twinfilin works downstream of CP binding to barbed ends, regulated the turnover of CP through its unconventional CPI motif. Together, our findings provide insight on how three CPI motif proteins work together to regulate CP in a step-wise fashion during yeast CME.

#### 3.2 Introduction

Endocytosis is the process by which cells collect cargo along the plasma membrane, invaginate the surrounding membrane and pinch off the invagination as a vesicle inside of the cell [165]. It is critical for processes such as nutrient uptake, signal transduction and remodeling of the plasma membrane [133]. Clathrin-mediated endocytosis (CME) is the best-studied form of endocytosis, and an essential endocytic pathway in all eukaryotic cells [132, 133]. CME is highly

conserved in protein components, progression and function from yeast to mammals, making the budding yeast *S. cerevisiae* an attractive model system for the study of CME in cells [33, 132]. During CME, over 60 endocytic proteins assemble dynamically at endocytic sites along the plasma membrane to drive membrane invagination and vesicle formation [9, 48]. In yeast, CME is dependent on polymerization of an Arp2/3-derived branched actin network to drive membrane invagination [8, 14]. To form the branched actin network, nearly 30 endocytic factors arrive at CME sites within 5-10 second of each other to nucleate new actin filaments, cap the growing ends of elongating filaments and turnover the actin network [48, 140]. The result is a dense meshwork of actin filaments averaging only ~50 nm in length, or 20 actin subunits [45]. While the function of many endocytic factors involved in the actin polymerization phase of CME is known, there are many others whose function have not been elucidated [6, 81].

One important component in branched actin network assembly is actin capping protein (CP). CP binds the fast-growing barbed end of actin filaments with sub-nanomolar affinity, preventing the addition or loss of actin subunits [88-90]. Actin filament capping is critical for creating short and stiff actin filaments that are effective at pushing against the plasma membrane and preserving the pool of actin monomers [98, 166, 167]. CP is a well-conserved heterodimer consisting of an  $\alpha$  and  $\beta$  subunit. In budding yeast, the *CAP1* and *CAP2* genes encode the ~30 kDa  $\alpha$  and  $\beta$  subunits, respectively [63, 128]. Deletion of either *CAP1* or *CAP2* results in an abnormally large cortical actin network and defects in CME progression [9, 63]. The CP complex has a characteristic mushroom shape, with a cap region responsible for capping actin filaments, and a stalk region that is subject to regulation by a diverse group of proteins containing capping protein-interacting (CPI) motifs [112-115]. CPI motifs facilitate interaction with-, and allosteric regulation of CP, decreasing the affinity of CP for barbed ends and removing CP bound to barbed ends *in vitro* [101, 116]. The best studied CPI motif-containing proteins are the CARMIL family of proteins, large multi-domain proteins important for actin-

based motility [119]. Given the 'uncapping' activity displayed by CPI motifs *in vitro*, they were hypothesized to function downstream of CP binding to barbed ends, working to uncap actin filaments [116]. However, more recent cell biological findings suggest that CPI motif proteins are required for the proper localization of CP to actin networks, thus working upstream of CP binding barbed ends [102, 120].

Until recently, CPI motif proteins had not been identified in yeast. As such, the binding of CP to barbed ends was assumed to be an unregulated process in yeast, with CP freely diffusing through the cytosol to cap actin filaments. Contrary to this assumption, mathematical modeling of cortical actin patch kinetics in fission yeast indicated that *in vivo* capping of actin filaments occurred 10 times faster than in *in vitro* studies, suggesting the process may be regulated [168]. In accord, the yeast CME factor Aim21 (Altered Inheritance of Mitochondria 1) was recently discovered to contain a CPI motif that facilitated a direct interaction with CP [130]. Aim21 forms a complex with Tda2 which functions during the actin polymerization phase of CME [83, 85]. Together with its binding partner Tda2, Aim21 binds to CP with nanomolar affinity [130]. Mutation of the Aim21 CPI motif causes a defect in CP recruitment to cortical actin patches, providing support for CPI motif proteins functioning to localize CP [130]. Despite these findings on Aim21, many questions remain about how it regulates CP. While CPI motifs allosterically inhibit CP *in vitro*, this has not been demonstrated for Aim21. Additionally, mutating the CPI motif of Aim21 results in only a partial defect in CP recruitment to CME sites, suggesting CPI motifs may not be critical for CP localization in yeast.

Twinfilin is a well-conserved actin regulator that was initially identified and characterized in budding yeast [77]. It is a member of the actin depolymerization factor-homology (ADFH) domain family of proteins, which includes the actin severing protein cofilin [169, 170]. The physiological function of twinfilin has remained enigmatic due to a multitude of functions displayed in *in vitro* assays, as twinfilin has been described as an actin monomer sequestering

protein [77, 171, 172], a barbed end capping protein [173, 174], and an actin depolymerization factor [125, 158, 175]. Early experiments in yeast linked twinfilin directly to CP and barbed ends, as it interacted directly with CP and required CP for localization to cortical actin patches [123, 124]. Recently, the interaction between twinfilin and CP was shown to occur through an unconventional CPI motif in the C-terminal tail of twinfilin [126]. Unlike conventional CPI motifs, the CPI motif of Twinfilin does not allosterically inhibit CP, despite sharing a binding site on CP with CARMIL-type CPI motifs [126, 127, 157]. Given this, twinfilin was categorized as a 'pro-capper', preventing CARMIL-type CPI motifs from binding to and inhibiting/uncapping CP [117]. In contrast, cell biological data suggests twinfilin is largely responsible for uncapping CP, with its CPI motif necessary for localization to barbed ends [127]. Thus, the function of twinfilin in cells remains unclear in both yeast and higher eukaryotes.

In this study, we identify the little-studied yeast endocytic factor, Bsp1, as a novel CPI motif-containing protein. Bsp1 works together with Aim21 to recruit CP to the actin network during CME. In contrast, Twf1 works downstream of CP recruitment, likely working to turnover CP from actin filament barbed ends. Together, our findings shed light on how CPI motifs regulate CP in a step-wise manner during yeast endocytosis.

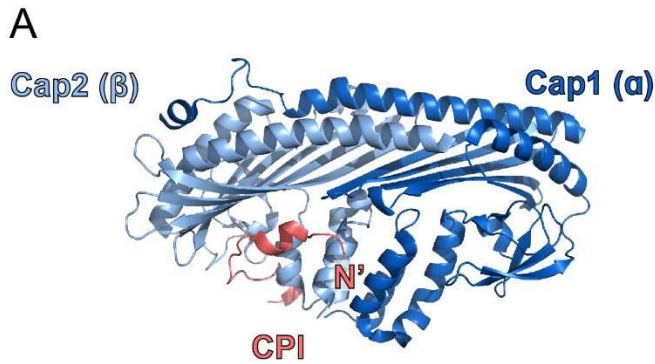
### **3.3 Results**

#### **3.3.1 *Aim21, Bsp1 and Twf1 contain CPI motifs***

While it has been established that Aim21 and twinfilin (Twf1) contain CPI motifs that facilitate interaction with CP, it's unclear whether any additional yeast proteins contain CPI motifs. In order to identify novel CPI motif-containing yeast factors, we performed a sequence alignment of the Aim21 and Twf1 CPI motifs against the *S. cerevisiae* proteome. While alignment of the Twf1 CPI motif resulted in no clear hits for proteins involved in endocytosis or

with the actin network, alignment using the Aim21 CPI motif resulted in hits for two potential CPI motif-containing proteins involved in CME (**Figure 3.1A**). Bsp1 (Binding of Synaptojanin Protein 1) is a little-studied 65 kDa protein that was initially identified as a binding partner for the yeast CME factors Inp52 and Inp53 [86]. Inp51 (Inositol -polyphosphate 5-Phosphatase 1) is a ~108 kDa synaptojanin-like protein that is important for the regulation of membrane phospholipids during CME [176, 177]. To test whether either of these proteins interact with CP, a GST pulldown experiment was performed with glutathione-S-transferase (GST) fused to the potential CPI motifs of Bsp1 and Inp51. In addition, GST was fused to the CPI motifs of Aim21 and Twf1, the known CP interactors. For this experiment and all future *in vitro* binding experiments, the CPI motif sequence of Aim21 also includes its Tda2-binding region (TBR), located just downstream of its CPI motif, which facilitates interaction with Tda2 and greatly increases the affinity between Aim21 and CP [130]. In these cases, 6-histidine-tagged Tda2 (His-Tda2) is included in reactions to allow for formation of the Tda2-Aim21 complex. GST-fusions were immobilized on glutathione resin, and subsequently incubated with 6-histidine-tagged CP (His-Cap1/2). While GST and GST-Inp51 failed to pulldown His-Cap1/2, each of GST-Aim21<sup>CPI</sup>, GST-Bsp1<sup>CPI</sup> and GST-Twf1<sup>CPI</sup> showed strong interactions with His-Cap1/2 (**Figure 3.1B**). While GST-Aim21<sup>CPI</sup> and GST-Twf1<sup>CPI</sup> were able to pulldown similar amounts of His-Cap1/2, GST-Bsp1<sup>CPI</sup> displayed the most robust interaction with His-Cap1/2 (**Figure 1B**).

To determine the binding affinity between CP and the CPI motifs of Aim21, Bsp1 and Twf1, a series of fluorescence polarization assays were performed. FITC-labelled CPI motif peptides (FITC-Aim21<sup>CPI</sup>, FITC-Bsp1<sup>CPI</sup> and FITC-Twf1<sup>CPI</sup>) were titrated with a range of concentrations of His-Cap1/2 (CP), and fluorescence polarization values were measured (**Figure 3.1C, 3.1D, 3.1E, 3.2A, 3.2B, 3.2C**). The data were fit to a one-site binding model to determine dissociation constants (**Figure 3.1F**). FITC-Aim21<sup>CPI</sup> and FITC-Twf1<sup>CPI</sup> displayed comparable  $K_d$  values of  $307 \pm 23$  nM and  $271 \pm 23$  nM, respectively (**Figure 3.1F**). Consistent



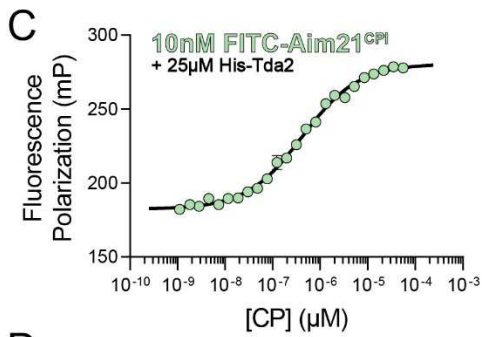
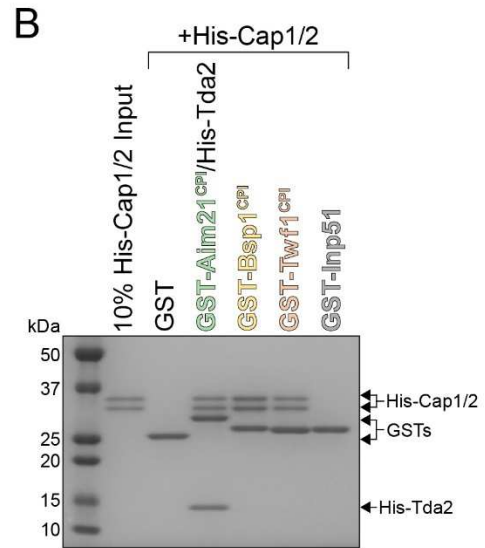
CPI      LxHxTxxRPKxxxxxxP

**Aim21** 495 GPLGGTRRGRGPRGRKLP SKV 515

**Bsp1** 555 KPLVHPNKNRTRGPRRKL PTR 575

**Twf1** 313 PNKSNLKFNPKGPLRKR RT\* 332

**Inp51** 878 PTHSPTPIPEPKRGRKL PPS 898



**F**

CPI	$K_d$ (nM)
Aim21 <sup>CPI</sup>	307 $\pm$ 23
Bsp1 <sup>CPI</sup>	34 $\pm$ 3
Twf1 <sup>CPI</sup>	271 $\pm$ 23

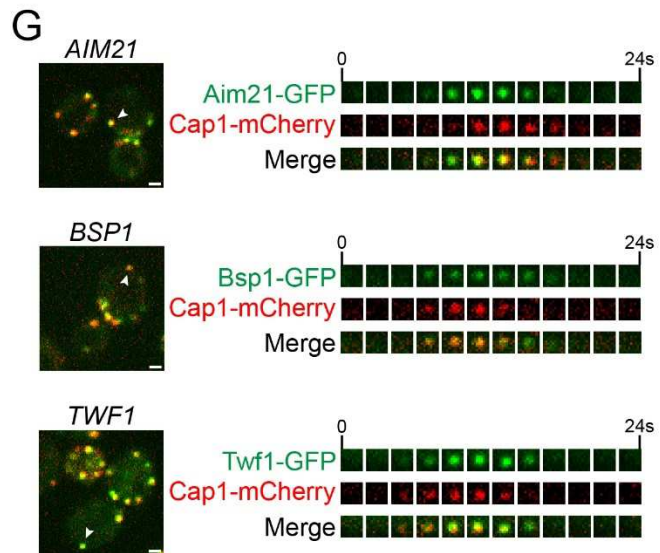
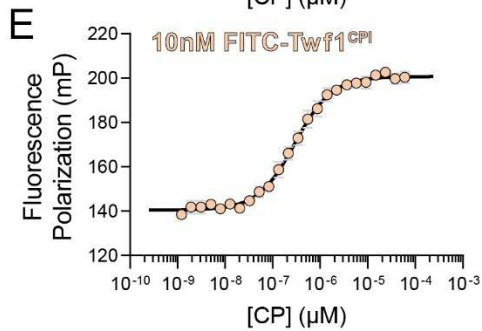
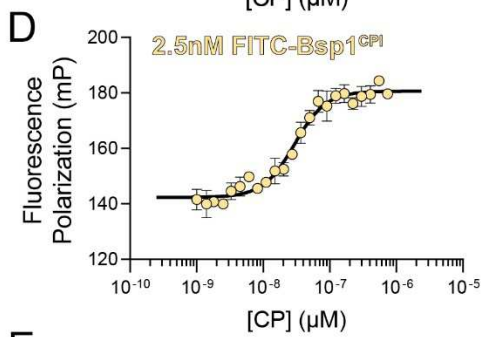


**Figure 3.1: Aim21, Bsp1 and Twf1 contain CPI motifs.** (A, top) Crystal structure of the chicken CP complex bound to the CPI motif of human CD2AP (PDB Entry 3AA6). The  $\alpha$ -subunit (Cap1) is displayed in dark blue, the  $\beta$ -subunit (Cap2) in light blue and the CPI motif of CD2AP is displayed in red. The N-terminus of the CPI motif is denoted with N'. (Bottom) The amino acid sequences of the *S. cerevisiae* proteins containing potential CPI motifs are shown. For Twf1, \* denotes the stop codon. For comparison, the consensus CPI motif sequence that has been previously described is shown above. (B) A GST-pulldown assay was performed with GST fused to fragments of Aim21 (491-545), Bsp1 (552-576), Twf1 (308-332) or Inp51 (874-900). Each GST fusion protein was incubated with His-Cap1/2, with Aim21 incubated with His-Tda2 additionally to form the Tda2/Aim21 complex. Bound proteins were analyzed by SDS-PAGE and Coomassie staining. The fragments of Aim21, Bsp1 and Twf1 demonstrated interaction with His-Cap1/2, while the fragment of Inp51 and GST alone did not. (C) A fluorescence polarization assay was performed using 10 nM FITC-Labelled Aim21 peptide spanning amino acids 493-540 (FITC-Aim21<sup>CPI</sup>) and various concentrations of His-Cap1/2 (CP). Reactions included 25  $\mu$ M His-Tda2 to form the Tda2-Aim21 complex. Data points represent the average and standard deviation from a single experiment performed in 3 technical replicates fit to a one-site binding isotherm. Note that error is too small for many data points to produce an error bar larger than the symbol and are therefore not visible. (D) A fluorescence polarization assay was performed as in 1C using 2.5 nM FITC-Labelled Bsp1 peptide spanning amino acids 552-576 (FITC-Bsp1<sup>CPI</sup>) and various concentrations of His-Cap1/2 (CP). (E) A fluorescence polarization assay was performed as in 1C using 10 nM FITC-Labelled Twf1 peptide spanning amino acids 308-332 (FITC-Twf1<sup>CPI</sup>) and various concentrations of His-Cap1/2 (CP). (F) Dissociation constants of CP and Aim21<sup>CPI</sup>, Bsp1<sup>CPI</sup> or Twf1<sup>CPI</sup>, respectively. Dissociation constants represent the mean  $\pm$  SEM from 3 independent experiments each fit to a one-site binding isotherm. (G, top) Live-cell fluorescence microscopy showing strong colocalization of Aim21-GFP with Cap1-mCherry, (Middle) Bsp1-GFP with Cap1-mCherry and (Bottom) Twf1-GFP with Cap1-mCherry at endocytic patches (SDY1518, SDY1520, SDY1522). Endocytic patches used for construction of kymographs to right are indicated by arrowheads. Scale bars, 1  $\mu$ m.

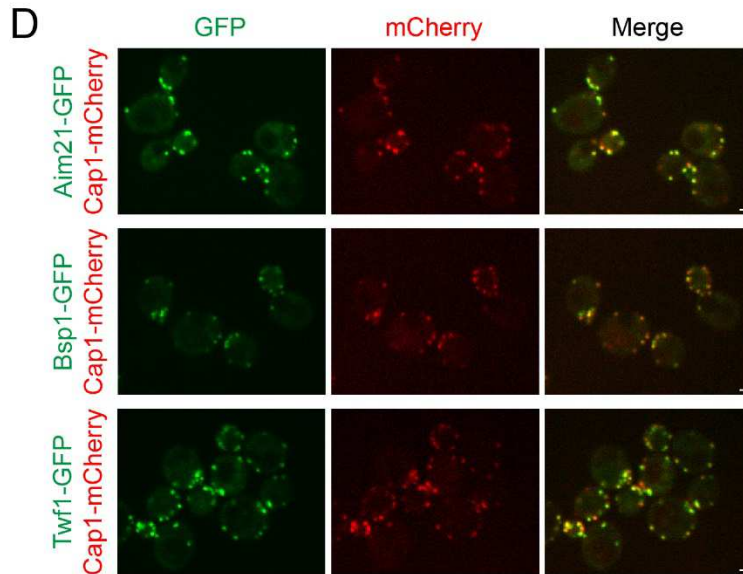
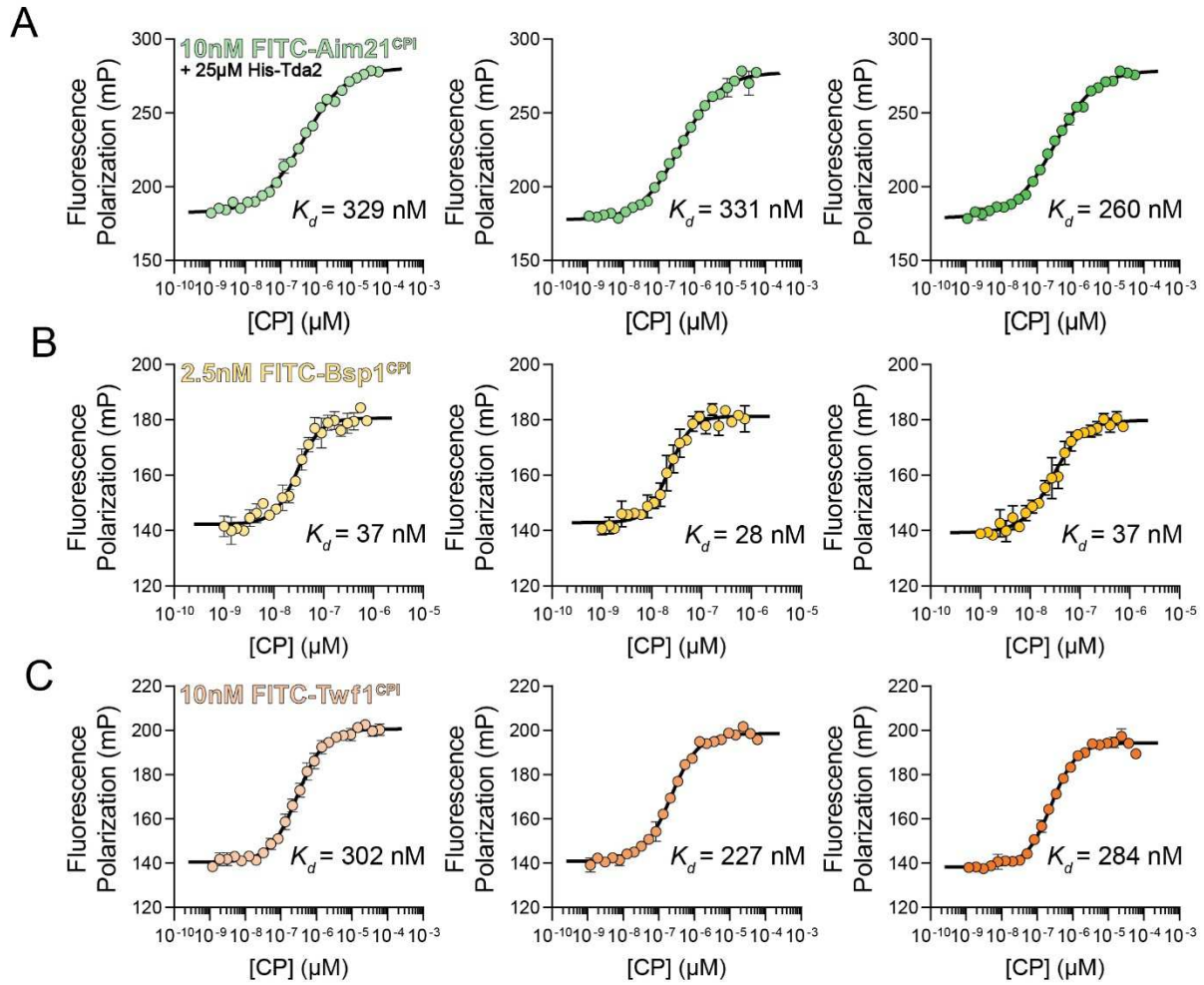


**Figure 3.2: Aim21, Bsp1 and Twf1 contain CPI motifs.** (A) Three Independent fluorescence polarization assays were performed using 10 nM FITC-Labelled Aim21 peptide spanning amino acids 493-540 (FITC-Aim21<sup>CPI</sup>) and various concentrations of His-Cap1/2 (CP). Reactions included 25  $\mu$ M His-Tda2 to form the Tda2-Aim21 complex. Data points represent the average and standard deviation from a single experiment performed in 3 technical replicates fit to a one-site binding isotherm. Note that error is too small for many CP concentration data points to produce an error bar larger than the symbol. The dissociation constant determined for individual experiments is listed at the lower right of each graph. (B) Three independent fluorescence polarization assays were performed as in 1SA using 2.5 nM FITC-Labelled Bsp1 peptide spanning amino acids 552-576 (FITC-Bsp1<sup>CPI</sup>) and various concentrations of His-Cap1/2 (CP). (C) Three independent fluorescence polarization assays were performed as in 1SA using 10 nM FITC-Labelled Twf1 peptide spanning amino acids 308-332 (FITC-Twf1<sup>CPI</sup>) and various concentrations of His-Cap1/2 (CP). (D) Fluorescence microscopy images taken with 1 second exposure times of cells expressing Cap1-mCherry along with either Aim21-GFP, Bsp1-GFP or Twf1-GFP. Aim21-GFP and Twf1-GFP are expressed at higher levels than Bsp1-GFP based on fluorescence intensity levels.

with the GST-pulldown experiment, FITC-Bsp1<sup>CPI</sup> had the most robust interaction with CP, with a  $K_d$  of  $34 \pm 23$  nM (**Figure 3.1B, 3.1F**).

To assess the dynamics of the CPI motif-containing proteins during CME, yeast strains were constructed to express Cap1-mCherry together with a GFP-tagged CPI motif protein from their corresponding endogenous loci. Two-color live-cell fluorescence microscopy showed that Aim21-GFP and Cap1-mCherry share nearly identical dynamics during CME, arriving at endocytic patches and leaving in unison (**Figure 3.1G, top**). Strains expressing Bsp1-GFP or Twf1-GFP, respectively, showed similar dynamics, demonstrating that all three proteins work during the actin polymerization phase of CME along with CP (**Figure 3.1G**). Still images taken with equal exposure times suggest Aim21-GFP and Twf1-GFP are expressed at similar levels, while Bsp1-GFP is expressed at a lower level (**Figure 3.2D**). Together, these findings establish Bsp1 as a novel CPI motif-containing protein in yeast, and suggest that the three endocytic factors could potentially regulate CP during CME.

### 3.3.2 *CPI motifs are essential for the function of Aim21, Bsp1 and Twf1*

CPI motifs are enriched in basic residues, which participate in electrostatic interactions with acidic residues along the CPI motif binding site of CP. Previously, we were able to abolish the interaction between Aim21 and CP by mutating three basic residues within the Aim21 CPI motif to glutamate [130]. Similar to the CPI motif of Aim21, the CPI motifs of Bsp1 are enriched in basic residues (**Figure 3.3A**). To determine if Bsp1 and Twf1 have a similar reliance on electrostatic interactions for their binding to CP, a GST-pulldown experiment was performed with GST fused to CPI motifs harboring three basic-to-acidic mutations within the CPI motif (**Figure 3.3A**). GST-fusions were immobilized on glutathione resin, and subsequently incubated with His-Cap1/2. Each of the wild-type CPI-fusion displayed a robust interaction with His-Cap1/2

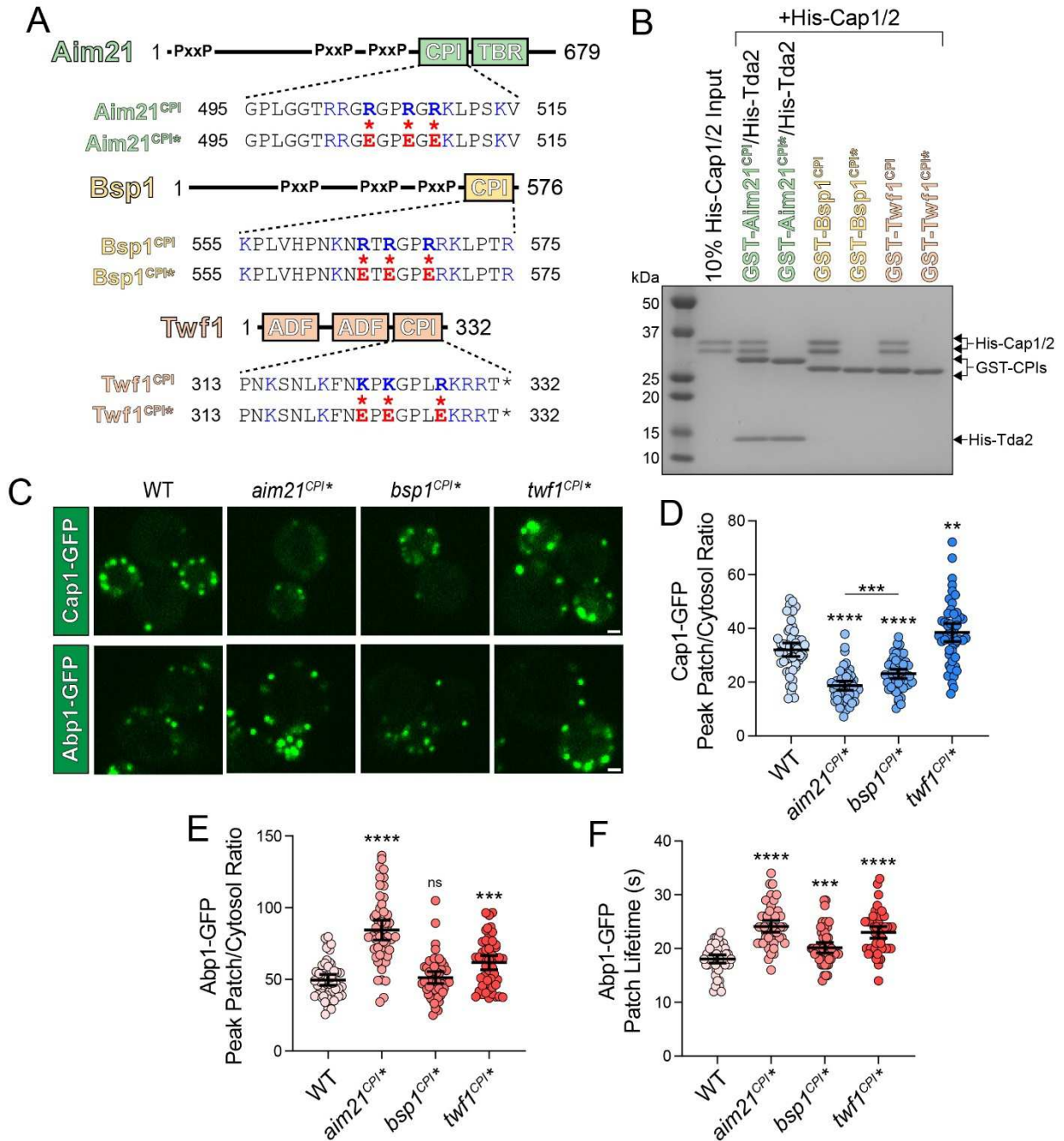


**Figure 3.3: CPI motifs are essential for the function of Aim21, Bsp1 and Twf1.** (A) Organization of Aim21, Bsp1 and Twf1 Domains. PxxP = Polyproline motif-rich region. CPI = capping protein interacting motif. TBR = Tda2 binding region. ADF= Actin depolymerization factor-homology. The sequences of the CPI motifs for each of Aim21, Bsp1 and Twf1 are displayed, with the three basic-to-acidic point mutations to the CPI motifs that will be used throughout the work shown in red. Aim21<sup>CPI\*</sup> = Aim21<sup>504,507,509E</sup>. Bsp1<sup>CPI\*</sup> = Bsp1<sup>564,566,569E</sup>. Twf1<sup>CPI\*</sup> = Twf1<sup>322,324,328E</sup>. (B) A GST-pulldown assay was performed with GST fused to the CPI motifs of Aim21, Bsp1 or Twf1. The GST-CPI fusions either contained no mutations (CPI) or three point mutations to the CPI motif (CPI\*), as indicated in Figure 2A. Each GST fusion protein

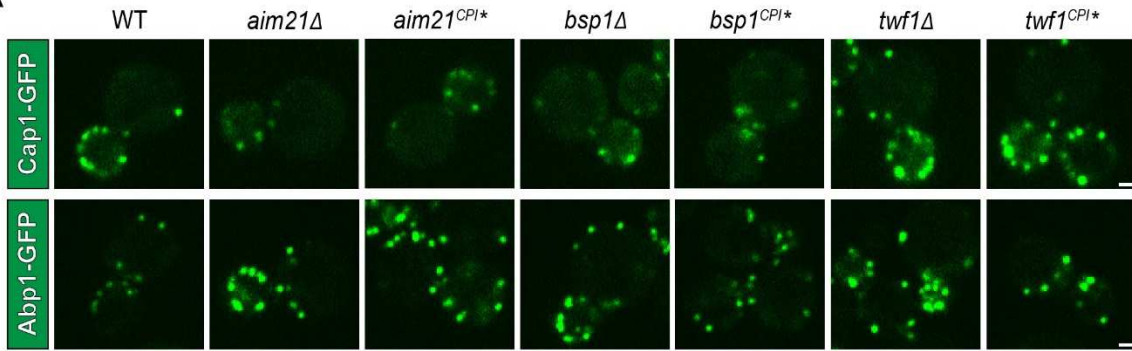
was incubated with His-Cap1/2, with Aim21 incubated with His-Tda2 additionally to form the Tda2/Aim21 complex. Bound proteins were analyzed by SDS-PAGE and Coomassie staining. The mutations to each CPI motif abolished the interaction with His-Cap1/2. (C, top) Live-cell fluorescence microscopy showing reduced recruitment of Cap1-GFP to endocytic sites in cells with the CPI motifs of Aim21 or Bsp1 mutated (SDY1474, SDY1512). In contrast, cells with the CPI motif of Twf1 mutated display an increase in Cap1-GFP patch intensity (SDY1513). (Bottom) Live-cell fluorescence microscopy showing increased recruitment of Abp1-GFP to endocytic sites in cells with the CPI motif of Aim21, Bsp1 or Twf1 mutated (SDY1434, SDY1514, SDY1515). Scale bars, 1  $\mu\text{m}$ . (D) Quantification of Cap1-GFP peak fluorescence intensity at endocytic patches in wild-type (WT), *aim21*<sup>CPI\*</sup>, *bsp1*<sup>CPI\*</sup> and *twf1*<sup>CPI\*</sup> cells. From left to right, mean peak patch/cytosol ratio = 32.08, 18.73, 23.13, 38.49 and n = 50 for all groups. Error bars, mean with 95% CI. \*\**P* ≤ 0.01, \*\*\**P* ≤ .001, \*\*\*\**P* ≤ .0001. (E) Quantification of Abp1-GFP peak fluorescence intensity at endocytic patches in wild-type (WT), *aim21*<sup>CPI\*</sup>, *bsp1*<sup>CPI\*</sup> and *twf1*<sup>CPI\*</sup> cells. From left to right, mean peak patch/cytosol ratio = 49.63, 84.36, 51.25, 61.68 and n = 50 for all groups. Error bars, mean with 95% CI. ns=not significant, \*\*\**P* ≤ 0.001, \*\*\*\**P* ≤ .0001. (F) Quantification of Abp1-GFP patch lifetime at endocytic patches in wild-type (WT), *aim21*<sup>CPI\*</sup>, *bsp1*<sup>CPI\*</sup> and *twf1*<sup>CPI\*</sup> cells. From left to right, mean patch lifetime = 18.06, 24.12, 20.14, 23.02 and n = 50 for all groups. Error bars, mean with 95% CI. \*\*\**P* ≤ 0.001, \*\*\*\**P* ≤ 0.0001.

(**Figure 3.3B**). In contrast, each of the mutant CPI motif fusion proteins, GST-Aim21<sup>CPI\*</sup>, GST-Bsp1<sup>CPI\*</sup> and GST-Twf1<sup>CPI\*</sup>, displayed no interaction with His-Cap1/2 (**Figure 3.3B**).

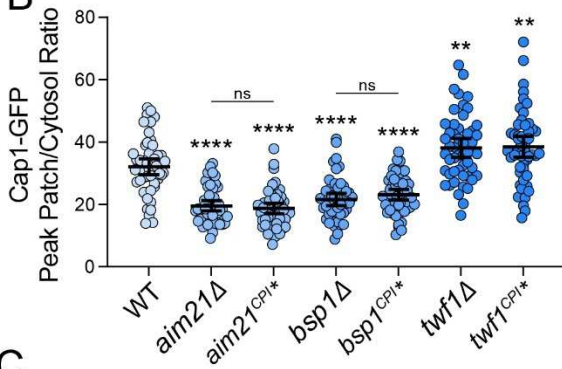
Having identified mutations that disrupt each of the CP:CPI interactions *in vitro*, we next wanted to assess whether the CPI motifs were functionally relevant *in vivo*. We first assessed how mutating the CPI motifs affected recruitment of CP to CME sites. As we reported previously, *aim21<sup>CPI\*</sup>* cells displayed a reduction in Cap1-GFP recruitment to CME sites compared to wild-type (WT) cells, consistent with the idea that it aids in the recruitment of CP to CME sites (**Figure 3.3C top, 3.3D**) [130]. Similar to *aim21<sup>CPI\*</sup>* cells, *bsp1<sup>CPI\*</sup>* cells had a slight defect in Cap1-GFP recruitment, albeit less so than *aim21<sup>CPI\*</sup>* cells (**Figure 3.3C top, 3.3D**). Conversely, *twf1<sup>CPI\*</sup>* cells had significantly elevated levels of Cap1-GFP at endocytic sites (**Figure 3.3C top, 3.3D**). To determine the efficiency with which the mutated CPI motifs disrupted the interaction with CP, we compared the phenotypes of CPI motif mutant cells to gene knockout cells. Cells carrying a deletion of the *AIM21* gene (*aim21Δ*) displayed a comparable reduction in the recruitment of Cap1-GFP to CME sites as *aim21<sup>CPI\*</sup>* cells (**Figure 3.4A top, 3.4B**). Similarly, *bsp1Δ* and *twf1Δ* showed comparable phenotypes to *bsp1<sup>CPI\*</sup>* and *twf1<sup>CPI\*</sup>* cells, respectively (**Figure 3.4A top, 3.4B**). Importantly, the defect in Cap1-GFP recruitment seen in *aim21Δ*, *aim21<sup>CPI\*</sup>*, *bsp1Δ* and *bsp1<sup>CPI\*</sup>* cells was not due to reduced expression of Cap1-GFP (**Figure 3.4E**).

Cells with a defect in CP function show increased levels of the filamentous actin binding protein Abp1 at CME sites, likely due to an overgrown actin network [9, 129]. To determine the effect of CPI motif mutations on the actin network at CME sites, the mutant CPI alleles *aim21<sup>CPI\*</sup>*, *bsp1<sup>CPI\*</sup>* and *twf1<sup>CPI\*</sup>* were integrated into cells expressing Abp1-GFP at their endogenous loci. While *aim21<sup>CPI\*</sup>* and *twf1<sup>CPI\*</sup>* cells had significantly increased levels of Abp1-GFP at CME sites, *bsp1<sup>CPI\*</sup>* cells had levels comparable to wild-type cells (**Figure 3.3C bottom, 3.3E**). Despite *bsp1<sup>CPI\*</sup>* cells not causing a significant increase in Abp1-GFP recruitment, each

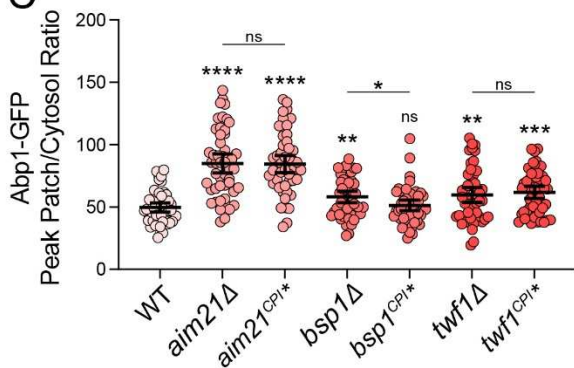
**A**



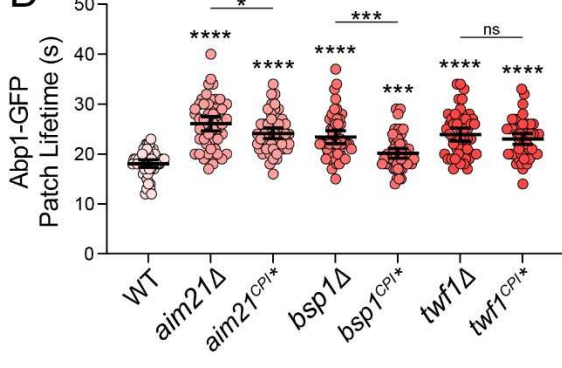
**B**



**C**



**D**



**E**

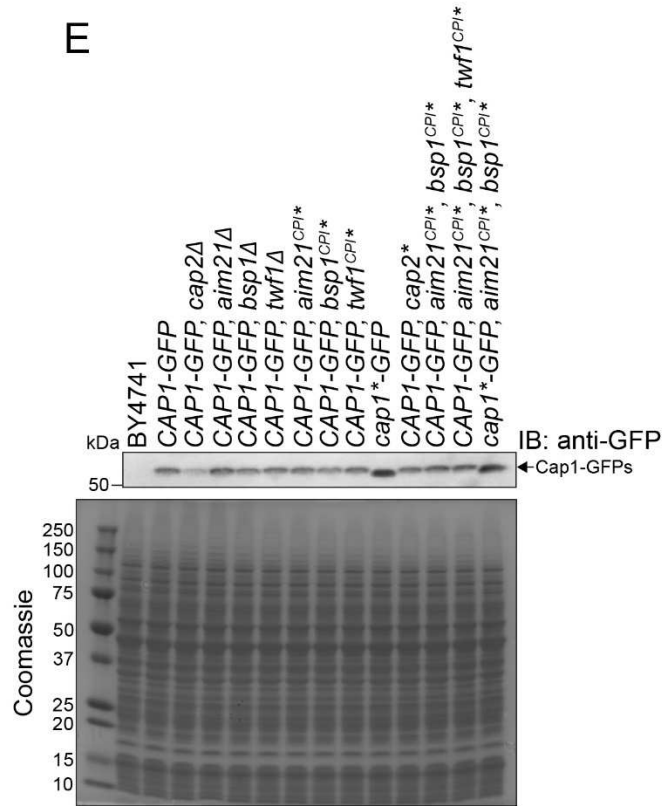


**Figure 3.4: CPI motifs are essential for the function of Aim21, Bsp1 and Twf1.** (A, top) Live-cell fluorescence microscopy showing reduced recruitment of Cap1-GFP to endocytic sites in cells lacking Aim21 or Bsp1 (SDY1292, SDY1350), or with the CPI motifs of Aim21 and Bsp1 mutated (SDY1474, SDY1512). In contrast, cells lacking Twf1 or with the CPI motif of Twf1 mutated display an increase in Cap1-GFP patch intensity (SDY1433, SDY1515). (Bottom) Live-cell fluorescence microscopy showing increased recruitment of Abp1-GFP to endocytic sites in cells lacking Aim21, Bsp1 or Twf1 (SDY1294, SDY1432, SDY1433), or with the CPI motifs of Aim21, Bsp1 or Twf1 mutated (SDY1434, SDY1514, SDY1515). Scale bars, 1  $\mu$ m. (B) Quantification of Cap1-GFP peak fluorescence intensity at endocytic patches in wild-type (WT), *aim21* $\Delta$ , *aim21*<sup>CPI\*</sup>, *bsp1* $\Delta$ , *bsp1*<sup>CPI\*</sup>, *twf1* $\Delta$ , and *twf1*<sup>CPI\*</sup> cells. From left to right, mean peak patch/cytosol ratio = 32.08, 19.56, 18.73, 21.60, 23.13, 38.11, 38.49 and n = 50 for all groups. Error bars, mean with 95% CI. ns=not significant, \*\**P*  $\leq$  0.01, \*\*\*\**P*  $\leq$  .0001. (C) Quantification of Abp1-GFP peak fluorescence intensity at endocytic patches in wild-type (WT), *aim21* $\Delta$ , *aim21*<sup>CPI\*</sup>, *bsp1* $\Delta$ , *bsp1*<sup>CPI\*</sup>, *twf1* $\Delta$ , and *twf1*<sup>CPI\*</sup> cells. From left to right, mean peak patch/cytosol ratio = 49.63, 84.96, 84.36, 58.10, 51.25, 59.71, 61.68 and n = 50 for all groups. Error bars, mean with 95% CI. ns=not significant, \**P*  $\leq$  0.05, \*\**P*  $\leq$  0.01, \*\*\**P*  $\leq$  0.001, \*\*\*\**P*  $\leq$  .0001. (D) Quantification of Abp1-GFP patch lifetime at endocytic patches in wild-type (WT), *aim21* $\Delta$ , *aim21*<sup>CPI\*</sup>, *bsp1* $\Delta$ , *bsp1*<sup>CPI\*</sup>, *twf1* $\Delta$  and *twf1*<sup>CPI\*</sup> cells. From left to right, mean patch lifetime = 18.06, 26.06, 24.12, 22.17, 20.14, 22.61, 23.02 and n = 50 for all groups. Error bars, mean with 95% CI. ns=not significant, \**P*  $\leq$  0.05, \*\*\**P*  $\leq$  0.001, \*\*\*\**P*  $\leq$  .0001. (E) Cell extracts from Cap1-GFP strains used for fluorescence microscopy (Figure 2C, S2A, 4C, 6A, 7C) were analyzed by immunoblotting (IB) using antibodies to the GFP tag (anti-GFP). The parent strain, BY4741, is shown as a negative control. (Bottom) Coomassie-stained gel of extracts show equal loading. The strains display comparable expression of Cap1-GFP with the exception of the *cap2* $\Delta$  strain, which was expected.

of the mutant CPI motif alleles caused a significant increase in the patch lifetime of Abp1-GFP, indicative of a defect in the actin polymerization phase of CME (**Figure 3.3C bottom, 3.3F**). While *aim21<sup>CPI\*</sup>* and *bsp1<sup>CPI\*</sup>* had a noticeable Abp1-GFP phenotype, the phenotypes seen in *aim21 $\Delta$*  and *bsp1 $\Delta$*  cells were more severe, hinting that the proteins likely have functions outside of their interaction with CP (**Figure 3.4A bottom, 3.4C, 3.4D**). Conversely, *twf1<sup>CPI\*</sup>* and *twf1 $\Delta$*  cells had indistinguishable Abp1-GFP and Cap1-GFP phenotypes, suggesting that the function of Twf1 is wholly dependent on its ability to interact with CP (**Figure 3.4A, 3.4B, 3.4C, 3.4D**). Thus, the CPI motifs of Aim21, Bsp1 and Twf1 are all important for the regulation of capping protein *in vivo*, although they likely regulate CP in different ways.

### 3.3.3 CPI motifs differentially affect the capping function of CP

Conventional CPI motifs have the ability to bind to and allosterically regulate CP, resulting in a CP that has reduced affinity for barbed ends [111, 112, 121]. However, the recent discovery of the unconventional CPI motif in Twinfilin, which does not affect the capping function of CP, has challenged the notion that inhibiting the capping function of CP is a hallmark characteristic of CPI motifs [126, 127, 157]. While it is expected that the CPI motif of yeast Twf1 functions like twinfilin in higher eukaryotes, this has not been demonstrated experimentally. To determine how the CPI motifs of Aim21, Bsp1 and Twf1 affect the capping function of CP, a series of pyrene actin polymerization assays were performed. Polymerization of pyrene-labelled actin was induced by the addition of polymerization buffer (Poly) in the presence or absence of His-Cap1/2 (CP). In the presence of CP, the polymerization rate of actin was severely reduced (**Figure 3.5A, 3.5B**). However, when CP was incubated with an unlabeled Aim21 CPI motif peptide (Aim21<sup>CPI</sup>) prior to actin polymerization, the polymerization rate increased substantially compared to CP alone (**Figure 3.5A, 3.5B, 3.6A**). Similarly, the addition of Bsp1<sup>CPI</sup> to CP resulted in a significant increase in the polymerization rate (**Figure 3.5A, 3.5B, 3.6B**). While not

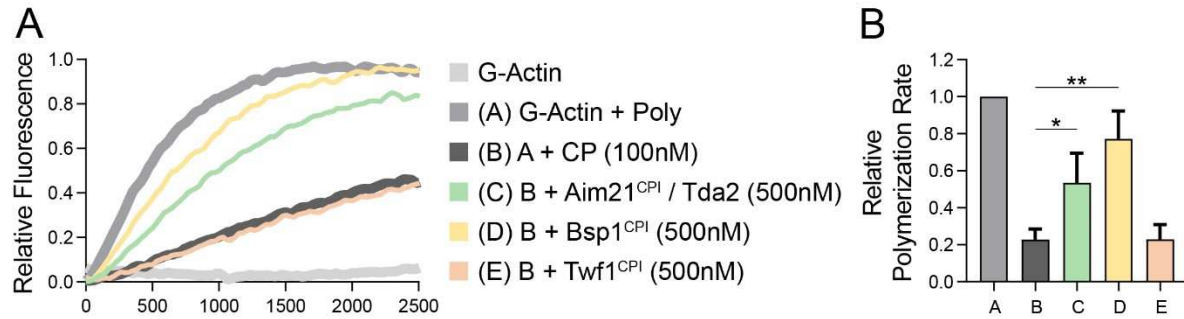


**Figure 3.5: CPI motifs differentially affect the capping function of CP.** (A) Pyrene-labelled rabbit actin (1  $\mu$ M, 20% labelled) was polymerized in the absence or presence of His-Cap1/2 (CP, 100 nM). In addition, reactions were performed with either 500 nM of unlabeled Aim21<sup>CPI</sup>, Bsp1<sup>CPI</sup> or Twf1<sup>CPI</sup> peptides. His-Tda2 was included in the Aim21<sup>CPI</sup> reaction to allow for formation of the Tda2-Aim21 complex. While the CPI motifs of Aim21 and Bsp1 partially inhibited the capping function of CP, the CPI motif of Twf1 has no effect. (B) Quantification of the relative polymerization rate from three independent pyrene actin polymerization assays. From left to right, mean relative polymerization rate = 1.00, 0.23, 0.54, 0.77, 0.23. Error bars, mean  $\pm$  SD. \* $P \leq 0.05$ , \*\* $P \leq .01$ .

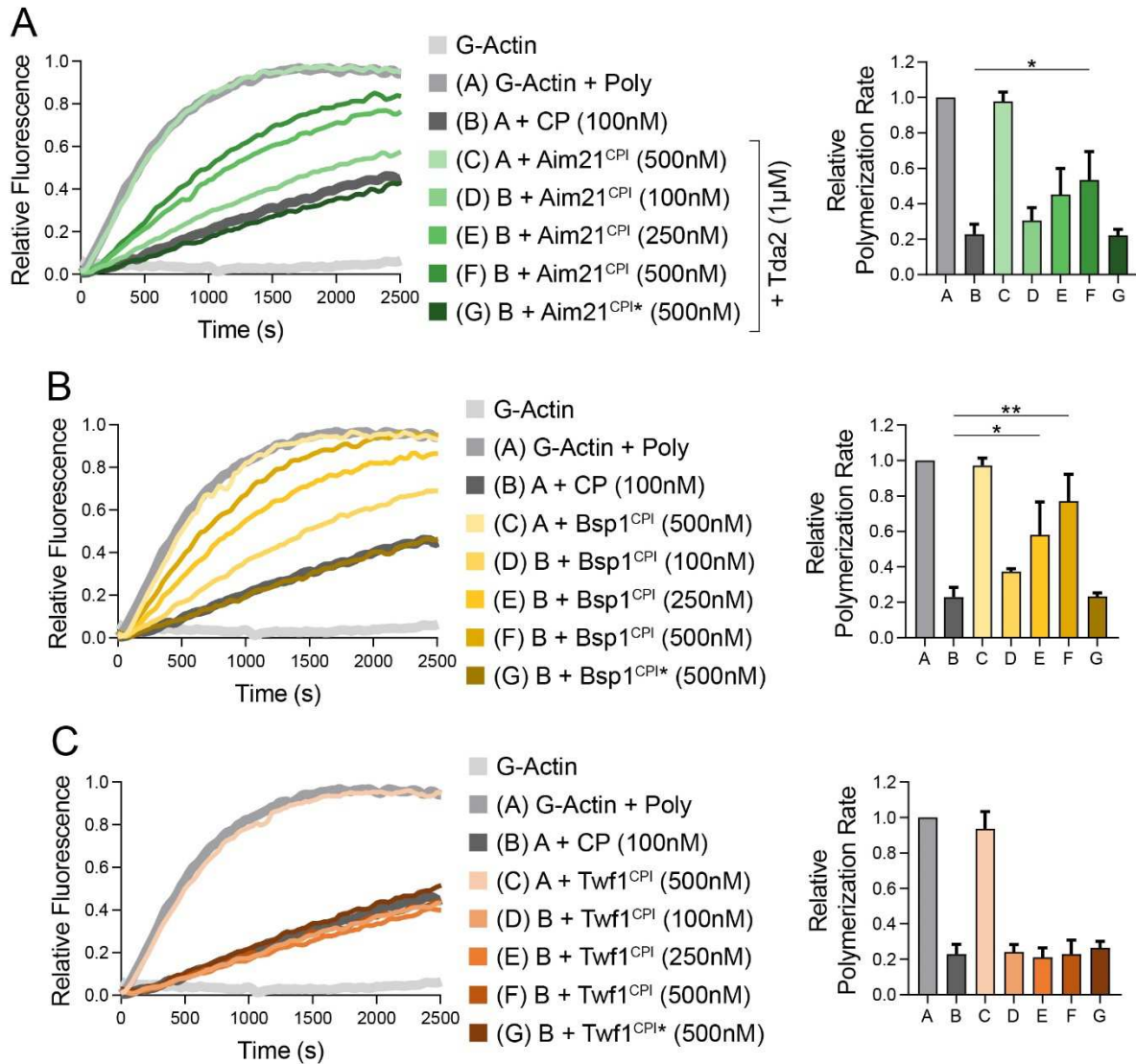


**Figure 3.6: CPI motifs differentially affect the capping function of CP.** (A, left) Pyrene-labelled rabbit actin (1  $\mu$ M, 20% labelled) was polymerized in the absence or presence of His-Cap1/2 (CP, 100 nM). In addition, reactions were performed with various concentrations of either unlabeled Aim21<sup>CPI</sup> or Aim21<sup>CPI\*</sup> peptides. His-Tda2 was included to allow for formation of the Tda2-Aim21 complex. While Aim21<sup>CPI</sup> partially inhibited the capping function of CP at high concentrations, Aim21<sup>CPI\*</sup> had no effect. (Right) Quantification of the relative polymerization rate from three independent pyrene actin polymerization assays in Figure S3A. From left to right, mean relative polymerization rate = 1.00, 0.23, 0.98, 0.31, 0.45, 0.54, 0.22. Error bars, mean  $\pm$  SD. \* $P \leq 0.05$ . (B, left) Pyrene actin polymerization assays were performed as in S3A with various concentrations of either unlabeled Bsp1<sup>CPI</sup> or Bsp1<sup>CPI\*</sup> peptides. While Bsp1<sup>CPI</sup> inhibited the capping function of CP at high concentrations, Bsp1<sup>CPI\*</sup> had no effect. (Right) Quantification of the relative polymerization rate from three independent pyrene actin polymerization assays in Figure S3C. From left to right, mean relative polymerization rate = 1.00, 0.23, 0.97, 0.37, 0.58, 0.77, 0.23. Error bars, mean  $\pm$  SD. \* $P \leq 0.05$ , \*\* $P \leq 0.01$ . (C, left) Pyrene actin polymerization assays were performed as in S3A with various concentrations of either unlabeled Twf1<sup>CPI</sup> or

Twf1<sup>CPI\*</sup> peptides. Twf1<sup>CPI</sup> had no effect on the capping function of CP, even at high concentrations. (Right) Quantification of the relative polymerization rate from three independent pyrene actin polymerization assays in Figure S3E. From left to right, mean relative polymerization rate = 1.00, 0.23, 0.94, 0.24, 0.21, 0.23, 0.26. Error bars, mean  $\pm$  SD.

statistically significant, Bsp1<sup>CPI</sup> appeared to have a larger inhibitory effect on CP than Aim21<sup>CPI</sup> (**Figure 3.5A, 3.5B**). In contrast, the Twf1<sup>CPI</sup> peptide had no effect on the capping function of CP, even at high concentrations (**Figure 3.5A, 3.5B, 3.6C**).

While Aim21<sup>CPI</sup> and Bsp1<sup>CPI</sup> both had inhibitory effects on CP, this effect was not seen using the mutant peptides Aim21<sup>CPI\*</sup> and Bsp1<sup>CPI\*</sup>, indicating that the inhibitory effect requires the CP:CPI interaction (**Figure 3.6A, 3.6B**). Importantly, the CPI motifs alone had no effect on the polymerization of actin (**Figure 3.6A, 3.6B, 3.6C**). Thus, the CPI motifs of Aim21 and Bsp1 function like conventional CPI motifs, partially inhibiting the capping function of CP, while the CPI motif of Twf1 has an unconventional function, in-line with Twinfilin CPI motifs from higher eukaryotes.

### 3.3.4 CP:CPI interactions occur through an overlapping binding site

Numerous crystal structures of CPI motifs in complex with CP have shown that CPI motifs interact with the stalk region of CP, opposite the barbed end binding surface (**Figure 3.7A**). Of interest, the Cap2 ( $\beta$ ) subunit of CP has an extended binding interface with the CPI motif (**Figure 3.7A**). To determine if yeast CPI motifs interact with CP in a similar manner, a series of GST pulldown assays were performed using mutant Cap1/2 complexes. Given the large binding interface on the Cap2 subunit, and the reliance of the CPI motifs on basic residues for interaction with CP, we targeted acidic residues on the stalk region of Cap2 for mutation. Four different CP mutants were tested for interaction with CPI motifs: His-Cap1/2<sup>D44A</sup>, His-Cap1/2<sup>D64A</sup>, His-Cap1/2<sup>D88A</sup> and a mutant combining all three of the mutations, His-Cap1/2<sup>44,64,88A</sup>. GST-fused CPI motifs were immobilized on glutathione resin, and subsequently incubated with CP or CP mutants. Each of the CP mutants displayed different degrees of binding with the CPI motifs (**Figure 3.7B**). GST-Aim21<sup>CPI</sup> pulled down normal levels of His-Cap1/2<sup>D44A</sup>, but pulled down less His-Cap1/2<sup>D64A</sup> and His-Cap1/2<sup>D88A</sup> than wild-type CP (**Figure**

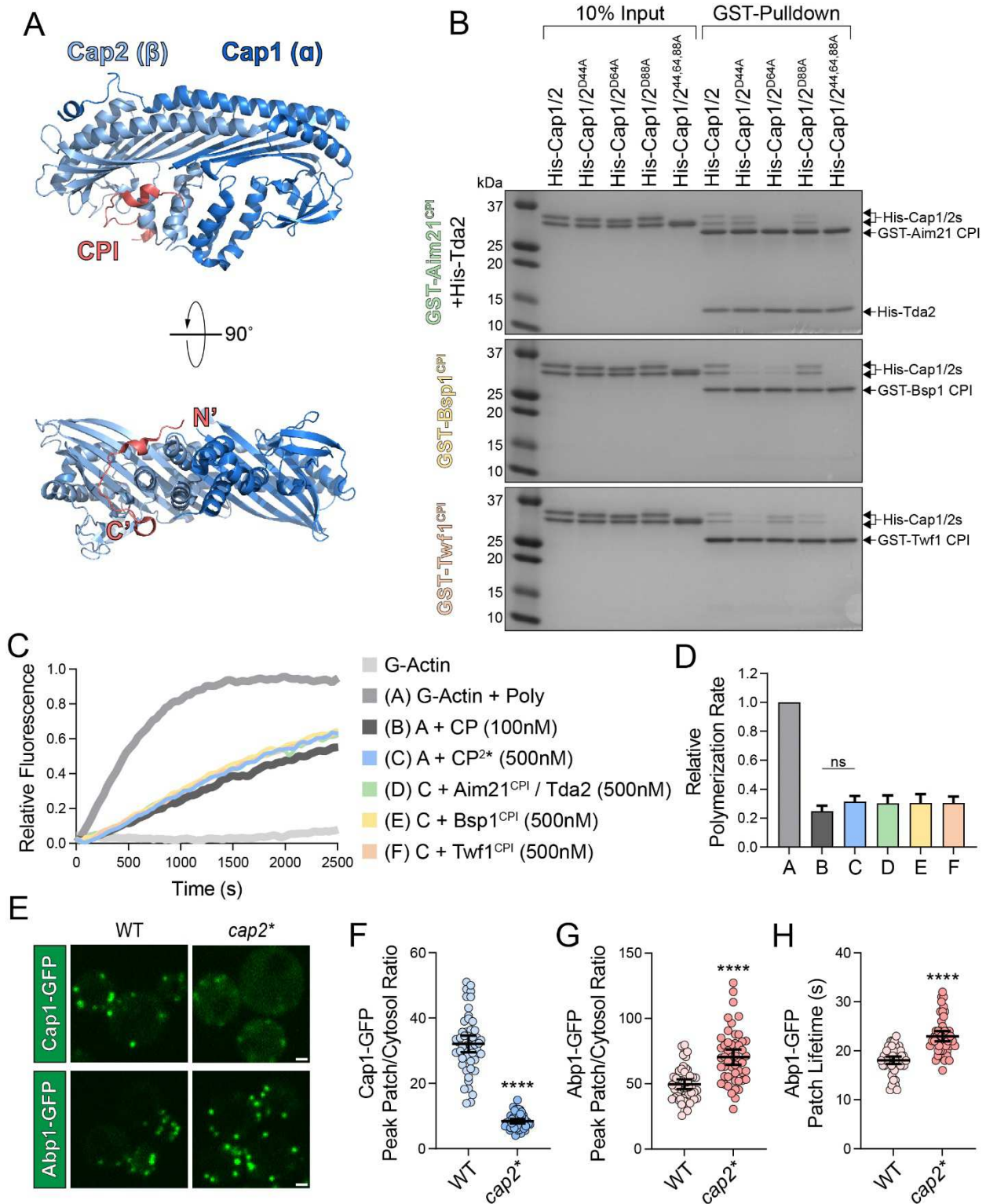


**Figure 3.7: CP:CPI interactions occur through an overlapping binding site.** (A, top) Crystal structure of chicken CP bound to the CPI motif of human CD2AP (PDB Entry 3AA6). The  $\alpha$ -subunit (Cap1) is displayed in dark blue, the  $\beta$ -subunit (Cap2) in light blue, and the CPI motif of

CD2AP is shown in red. (Bottom) The CP complex is rotated 90° for a view of the underside of CP, or the stalk region. The N-terminus and C-terminus of the CPI motif are labelled N' and C', respectively. The CP:CPI interaction occurs largely through a binding interface on the  $\beta$ -subunit. (B) A GST-pulldown assay was performed with GST fused to the CPI motifs of Aim21 (top), Bsp1 (middle) or Twf1 (bottom). Each GST fusion protein was incubated with either His-Cap1/2 or with a CP containing a mutated version of the Cap2 subunit. Aim21 was incubated with His-Tda2 additionally to form the Tda2/Aim21 complex. Bound proteins were analyzed by SDS-PAGE and Coomassie staining. The mutations to Cap2 affect the interaction with the GST-CPI motif fusions in varying ways, and abolish the interaction when combined. (C) Pyrene actin (1 $\mu$ M, 20% labelled) was polymerized in the absence or presence of His-Cap1/2 (CP, 100nM) or His-Cap1/2\* (CP<sup>2\*</sup>, 100nM). In addition, reactions were performed with either 500 nM of unlabeled Aim21<sup>CPI</sup>, Bsp1<sup>CPI</sup> or Twf1<sup>CPI</sup> peptides. His-Tda2 was included in the Aim21<sup>CPI</sup> reaction to allow for formation of the Tda2-Aim21 complex. CP<sup>2\*</sup> displayed an equivalent capping ability to CP, and the capping function of CP<sup>2\*</sup> was not affected by any of the CPI motifs. (D) Quantification of the relative polymerization rate from three independent pyrene actin polymerization assays in Figure 4C. From left to right, mean relative polymerization rate = 1.00, 0.25, 0.32, 0.30, 0.31, 0.31. Error bars, mean  $\pm$  SD. ns=not significant. (E, top) Live-cell fluorescence microscopy showing reduced recruitment of Cap1-GFP to endocytic sites in cells with the CPI motif binding site of Cap2 mutated (SDY1596). (Bottom) Live-cell fluorescence microscopy showing increased recruitment of Abp1-GFP to endocytic sites in cells with the CPI motif binding site of Cap2 mutated (SDY1599). Scale bars, 1  $\mu$ m. (F) Quantification of Cap1-GFP peak fluorescence intensity at endocytic patches in wild-type (WT) and *cap2\** cells. From left to right, mean peak patch/cytosol ratio = 32.08, 8.44 and n = 50 for all groups. Error bars, mean with 95% CI. \*\*\*\**P*  $\leq$  .0001. (G) Quantification of Abp1-GFP peak fluorescence intensity at endocytic patches in wild-type (WT) and *cap2\** cells. From left to right, mean peak patch/cytosol ratio = 49.63, 70.40 and n = 50 for all groups. Error bars, mean with 95% CI. \*\*\*\**P*  $\leq$  .0001. (H) Quantification of Abp1-GFP patch lifetime at endocytic patches in wild-type (WT) and *cap2\** cells. From left to right, mean patch lifetime = 18.06, 22.96 and n = 50 for all groups. Error bars, mean with 95% CI. \*\*\*\**P*  $\leq$  0.0001.

**3.7B**). GST-Bsp1<sup>CPI</sup> displayed a weakened interaction with His-Cap1/2<sup>D44A</sup> and His-Cap1/2<sup>D64A</sup>, but pulled down His-Cap1/2<sup>D88A</sup> at levels comparable to His-Cap1/2 (**Figure 3.7B**). GST-Twf1<sup>CPI</sup> pulled down less His-Cap1/2<sup>D44A</sup> and His-Cap1/2<sup>D88A</sup> than wild-type CP, but normal levels of His-Cap1/2<sup>D64A</sup> (**Figure 3.7B**). For each of the CPI motif-fusions, the triple mutant CP, His-Cap1/2<sup>44,64,88A</sup>, abolished the CP:CPI interaction (**Figure 3.7B**). Together, these results suggest that CPI motifs interact with the stalk region of CP, as has been shown in higher eukaryotes.

Having identified mutations to the Cap2 subunit of CP that would disrupt the interaction with all three CPI motif proteins, we next wanted to see the endocytic phenotype produced when the mutations were integrated into the yeast genome. Before doing so, we needed to ensure that the CP mutant retained its capping function. When pyrene actin polymerization was induced in the presence of His-Cap1/2 (CP) or the triple mutant His-Cap1/2<sup>44,64,88A</sup> (CP<sup>2\*</sup>), the rate of polymerization was reduced to comparable levels, indicating the mutations to Cap2 that abolish binding to CP motifs did not affect the ability of CP<sup>2\*</sup> to cap barbed ends (**Figure 3.7C, 3.7D**). Additionally, adding Aim21<sup>CPI</sup> or Bsp1<sup>CPI</sup> to CP<sup>2\*</sup> prior to inducing actin polymerization did not result in inhibition of CP<sup>2\*</sup> as it did with wild-type CP, providing further proof that the mutations disrupt the CP:CPI interaction (**Figure 3.5A, 3.5B, 3.7C, 3.7D**).

To determine the endocytic phenotype produced when all three CPI motifs are unable to interact with CP, we integrated the mutant *cap2*<sup>44,64,88A</sup> (*cap2*<sup>\*</sup>) allele at the endogenous *CAP2* locus, initially in cells expressing Cap1-GFP. Cap1-GFP recruitment was severely impaired in *cap2*<sup>\*</sup> cells compared to wild-type cells (**Figure 3.7E top, 3.7F**). Interestingly, this defect was significantly larger in *cap2*<sup>\*</sup> cells than in either *aim21*<sup>CPI\*</sup> or *bsp1*<sup>CPI\*</sup> cells, with peak patch/cytosol ratios of 8.44, 18.73 and 23.13, respectively (**Figure 3.3D, 3.7E top, 3.7F**). The recruitment defect was not due to a decrease in expression of Cap1-GFP, as Cap1-GFP was expressed at comparable levels in wild-type and *cap2*<sup>\*</sup> cells (**Figure 3.4E**). As expected with a defect in CP recruitment, Abp1-GFP levels were significantly elevated in *cap2*<sup>\*</sup> cells and had an

increased patch lifetime, indicative of an enlarged actin network (**Figure 3.7E bottom, 3.7G, 3.7H**).

### 3.3.5 *Twf1* requires interaction with CP for proper localization to CME sites

Next, we wanted to determine how the CPI motif proteins were being recruited to endocytic sites. Aim21 is predicted to be a largely disordered protein. In addition to its CPI motif, it contains a motif for binding Tda2 (TBR) just downstream of the CPI motif, as well as three regions which are enriched in polyproline (PxxP) motifs (**Figure 3.8A**). Similar, to Aim21, Bsp1 is predicted to be largely disordered, and contains three regions enriched in polyproline motifs (**Figure 3.8A**). While Bsp1 has been shown to interact with synaptojanin proteins that participate in CME, these interactions have not been mapped. In contrast, Twf1 is a well-folded multi-domain protein consisting of twin actin depolymerization factor-homology domains (ADF), followed by a C-terminal tail containing the CPI motif (**Figure 3.8A**). To determine if the CPI motif-containing proteins are reliant on their interaction with CP for localization to CME sites, we looked at their recruitment to CME sites in cells with their CPI motifs mutated or cells lacking CP (*cap1Δ*). When mutations to disrupt the Aim21 CPI motif were integrated into the genome of *AIM21-GFP* cells (*aim21<sup>CPI\*</sup>*), Aim21<sup>CPI\*</sup>-GFP was recruited to endocytic sites at higher levels than wild-type cells (**Figure 3.8B top, 3.8C, 3.9A**). The corresponding phenotype was seen in *cap1Δ* cells, but with even higher levels of Aim21-GFP recruitment (**Figure 3.8B top, 3.8C**). Similarly, Bsp1<sup>CPI\*</sup>-GFP and Bsp1-GFP had a significant increase in recruitment to CME sites in *bsp1<sup>CPI\*</sup>* and *cap1Δ* cells, respectively (**Figure 3.8B middle, 3.8D, 3.9B**). In contrast, Twf1<sup>CPI\*</sup>-GFP was diffuse in the cytosol in *twf1<sup>CPI\*</sup>* cells and the same phenotype was seen for Twf1-GFP in *cap1Δ* cells (**Figure 3.8B bottom, 3.8E**). This is consistent with previous findings, and together show that Twf1 is reliant on its CP:CPI interaction for localization to endocytic sites [123, 124].

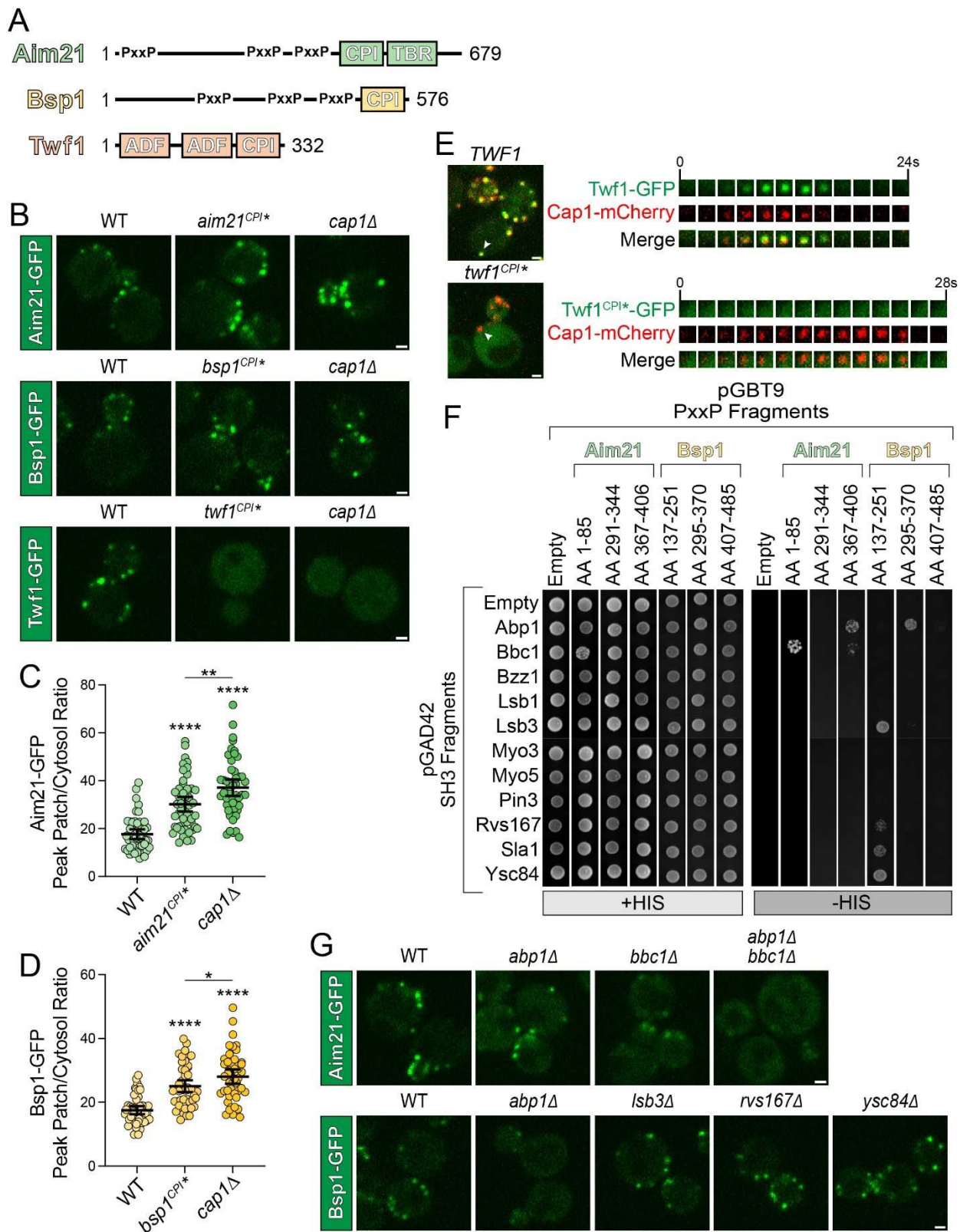


**Figure 3.8: Twf1 requires interaction with CP for proper localization to CME sites.** (A) Organization of Aim21, Bsp1 and Twf1 Domains. PxxP = Polyproline motif-rich region. CPI = capping protein interacting motif. TBR = Tda2 binding region. ADF= Actin depolymerization factor-homology. (B, top) Live-cell fluorescence microscopy showing increased recruitment of Aim21-GFP to endocytic sites in cells with the CPI motif of Aim21 mutated (SDY1472), or cells lacking Cap1 (SDY1478). (Middle) Live-cell fluorescence microscopy showing increased recruitment of Bsp1-GFP to endocytic sites in cells with the CPI motif of Bsp1 mutated (SDY1516), or cells lacking Cap1 (SDY1570). (Bottom) Live-cell fluorescence microscopy showing no recruitment of Twf1-GFP to endocytic sites in cells with the CPI motif of Twf1 mutated (SDY1517), or cells lacking Cap1 (SDY1572). Scale bars, 1  $\mu$ m. (C) Quantification of Aim21-GFP peak fluorescence intensity at endocytic patches in wild-type (WT), *aim21<sup>CPI\*</sup>* and *cap1* $\Delta$  cells. From left to right, mean peak patch/cytosol ratio = 17.61, 30.18, 37.07 and n = 50 for all groups. Error bars, mean with 95% CI. **\*\* $P \leq .01$ , \*\*\*\* $P \leq .0001$ .** (D) Quantification of Bsp1-GFP peak fluorescence intensity at endocytic patches in wild-type (WT), *bsp1<sup>CPI\*</sup>* and *cap1* $\Delta$  cells. From left to right, mean peak patch/cytosol ratio = 17.50, 25.02, 28.06 and n = 50 for all groups. Error bars, mean with 95% CI. **\* $P \leq .05$ , \*\*\*\* $P \leq .0001$ .** (E, top) Live-cell fluorescence microscopy showing strong colocalization of Twf1-GFP with Cap1-mCherry at endocytic patches (SDY1522). (Bottom) Live-cell fluorescence microscopy showing no localization of Twf1<sup>CPI\*</sup>-GFP with Cap1-mCherry at endocytic patches (SDY1523). Endocytic patches used for construction of kymographs to right are indicated by arrowheads. Scale bars, 1  $\mu$ m. (F) Yeast two-hybrid analysis of cells co-transformed with plasmids expressing the GAL4 activation (pGAD424) and binding (pGBT9) domains fused to the SH3 domain of various endocytic factors and polyproline motif-rich regions of Aim21 or Bsp1, respectively. Cells were spotted onto plates containing histidine (+HIS, control) or selective medium lacking histidine (-HIS). Cell growth, indicative of an interaction between proteins, was detected for Aim21 with Abp1 and Bbc1, and for Bsp1 with Abp1, Lsb3, Rvs167, Sla1 and Ysc84. (G, top) Live-cell fluorescence microscopy showing decreased recruitment of Aim21-GFP to endocytic sites in cells lacking Abp1, Bbc1 or both Abp1 and Bbc1 (SDY1011, SDY1658, SDY1663). (Bottom) Live-cell fluorescence microscopy showing decreased recruitment of Bsp1-GFP to endocytic sites in cells with lacking Abp1 (SDY1659). In contrast, cells lacking Lsb3, Rvs167 or Ysc84 display an increase in Bsp1-GFP patch intensity (SDY1660, SDY1700, SDY1661).

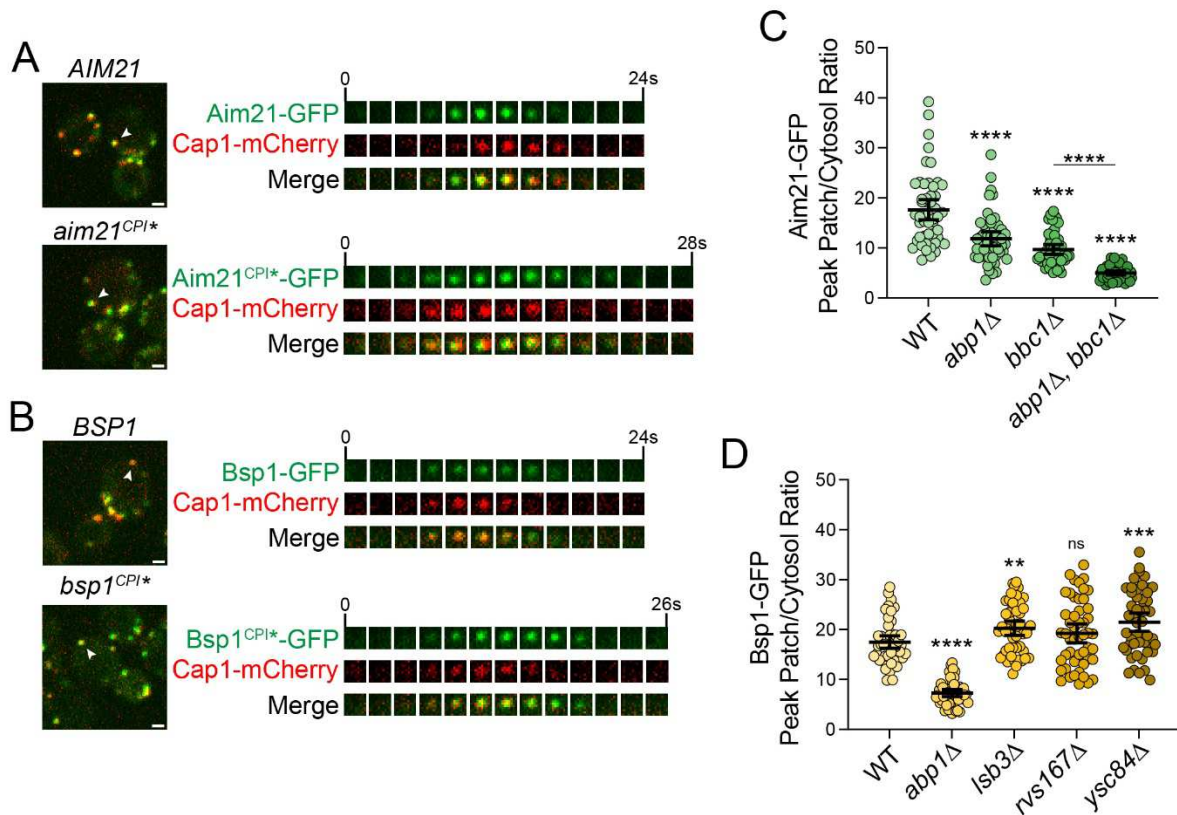


**Figure 3.9: Twf1 requires interaction with CP for proper localization to CME sites.** (A) Live-cell fluorescence microscopy showing strong colocalization of Aim21-GFP with Cap1-mCherry at endocytic patches (SDY1518). (Bottom) Live-cell fluorescence microscopy of Aim21<sup>CPI\*</sup>-GFP with Cap1-mCherry at endocytic patches (SDY1519). Endocytic patches used for construction of kymographs to right are indicated by arrows. Scale bars, 1  $\mu$ m. (B) Live-cell fluorescence microscopy showing strong colocalization of Bsp1-GFP with Cap1-mCherry at endocytic patches (SDY1520). (Bottom) Live-cell fluorescence microscopy of Bsp1<sup>CPI\*</sup>-GFP with Cap1-mCherry at endocytic patches (SDY1521). Endocytic patches used for construction of kymographs to right are indicated by arrowheads. Scale bars, 1  $\mu$ m. (C) Quantification of Aim21-GFP peak fluorescence intensity at endocytic patches in wild-type (WT), *abp1* $\Delta$ , *bbc1* $\Delta$  and *abp1* $\Delta$ /*bbc1* $\Delta$  cells. From left to right, mean peak patch/cytosol ratio = 17.61, 11.82, 9.70, 4.56 and  $n = 50$  for all groups. Error bars, mean with 95% CI. \*\*\*\* $P \leq .0001$ . (D) Quantification of Bsp1-GFP peak fluorescence intensity at endocytic patches in wild-type (WT), *abp1* $\Delta$ , *Isb3* $\Delta$  and *rvs167* $\Delta$  and *ysc84* $\Delta$  cells. From left to right, mean peak patch/cytosol ratio = 17.50, 7.29, 20.26, 19.24, 21.49 and  $n = 50$  for all groups. Error bars, mean with 95% CI. ns=not significant, \*\* $P \leq 0.01$ , \*\*\* $P \leq 0.001$ , \*\*\*\* $P \leq .0001$ .

Src homology 3 (SH3) domains are prevalent among many CME factors and facilitate interaction with polyproline motifs [178]. We previously demonstrated that Aim21 is largely dependent on an interaction between its PxxP motif-rich regions and the SH3 domain of the endocytic factor Bbc1 for recruitment to endocytic sites [83]. As Bsp1 is enriched in PxxP motifs like Aim21, we reasoned Bsp1 could also be reliant on a PxxP:SH3 interaction for localization to CME sites. To determine if the PxxP motif-rich regions of Aim21 and Bsp1 interacted with an SH3 domain of a CME factor, we used a yeast two-hybrid analysis to test binding of Aim21 and Bsp1 fragments to a library of SH3 domains. The PxxP motif-rich fragment of Aim21 spanning amino acids 1-85 interacted with the Bbc1 SH3, while the 367-406 fragment interacted with the Abp1 SH3, and to a lesser extent with the Bbc1 SH3 (**Figure 3.8F**). For the Bsp1 analysis, the 137-251 fragment interacted with the SH3 domains of Lsb3, Rvs167, Sla1 and Ysc84, and the 295-370 fragment displayed an interaction with the Abp1 SH3 domain (**Figure 3.8F**). In both *abp1* $\Delta$  and *bbc1* $\Delta$  cells, Aim21-GFP localization was reduced, and in cells combining the gene deletions, *abp1* $\Delta$ /*bbc1* $\Delta$ , there was a drastic recruitment defect, suggesting both proteins are important for the localization of Aim21 (**Figure 3.8G, 3.9C**). Bsp1-GFP only displayed a recruitment defect in *abp1* $\Delta$  cells, however, this recruitment defect was severe (**Figure 3.8G, 3.9D**). As *sla1* $\Delta$  cells grew slowly and appeared unhealthy, they were not included in the analysis. Thus, Twf1 relies on its interaction with CP, while Aim21 and Bsp1 are largely dependent on interactions with SH3 domain proteins, for proper localization.

### 3.3.6 *The CPI motifs of Aim21 and Bsp1 are requires for proper recruitment of CP to CME sites*

Given the similarities between the phenotypes seen in *aim21*<sup>CPI\*</sup> and *bsp1*<sup>CPI\*</sup> cells, combined with the large Cap1-GFP recruitment defect seen in *cap2*\* cells, we hypothesized that Aim21 and Bsp1 shared redundant roles in recruiting CP to CME sites. In line with this

hypothesis, *aim21<sup>CPI\*</sup>/bsp1<sup>CPI\*</sup>* cells had a significantly larger Cap1-GFP recruitment defect than either *aim21<sup>CPI\*</sup>* or *bsp1<sup>CPI\*</sup>* cells (**Figure 3.10A top, 3.10B, 3.10C**). While still present at endocytic sites at low levels, Cap1-GFP became largely diffuse in the cytosol in *aim21<sup>CPI\*</sup>/bsp1<sup>CPI\*</sup>* cells (**Figure 3.10A top, 3.10B**). Importantly, this defect was not due to a change in expression, as Cap1-GFP was expressed at comparable levels in wild-type and *aim21<sup>CPI\*</sup>/bsp1<sup>CPI\*</sup>* cells (**Figure 3.4D**). While Abp1-GFP levels at endocytic sites were similar in *aim21<sup>CPI\*</sup>* and *aim21<sup>CPI\*</sup>/bsp1<sup>CPI\*</sup>* cells, the patch lifetime was significantly longer in *aim21<sup>CPI\*</sup>/bsp1<sup>CPI\*</sup>* cells, suggesting a heightened defect in the actin polymerization stage of CME (**Figure 3.10A bottom, 3.10B, 3.10D, 3.10E**). In agreement with the reliance of Twf1 on CP for its localization, Twf1-GFP recruitment to CME sites was significantly impaired in *aim21<sup>CPI\*</sup>/bsp1<sup>CPI\*</sup>* cells. Together these findings point to a shared function of Aim21 and Bsp1 in recruiting CP to endocytic sites.

### 3.3.7 CPs ability to cap barbed ends is required for its localization and function

While our data support that the CPI motifs of Aim21 and Bsp1 are critical for CP localization to CME sites, a low level of CP was still present at CME sites in *aim21<sup>CPI\*</sup>/bsp1<sup>CPI\*</sup>* cells. We reasoned that the low level of CP still present could be from freely diffusing CP, which localizes to CME sites by freely binding actin filament barbed ends. The capping function of CP is largely dependent on the  $\alpha$ -tentacle at the C-terminus of the  $\alpha$ -subunit (Cap1) (**Figure 3.11A**). To abolish the capping function of CP, we utilized previously described mutations to the  $\alpha$ -tentacle that disrupt the capping function of yeast CP [129] (**Figure 3.11A**). Before integrating the mutations into the yeast genome, we wanted to ensure they would produce a large defect in the capping function of CP. When pyrene actin was polymerized in the presence of His-Cap1<sup>239,240A</sup>/Cap2 (CP<sup>1\*</sup>), the rate of polymerization was indistinguishable from a reaction with actin alone (**Figure 3.11B, 3.12A**). Importantly, CP<sup>1\*</sup> was pulled down by GST-CPI fusions with

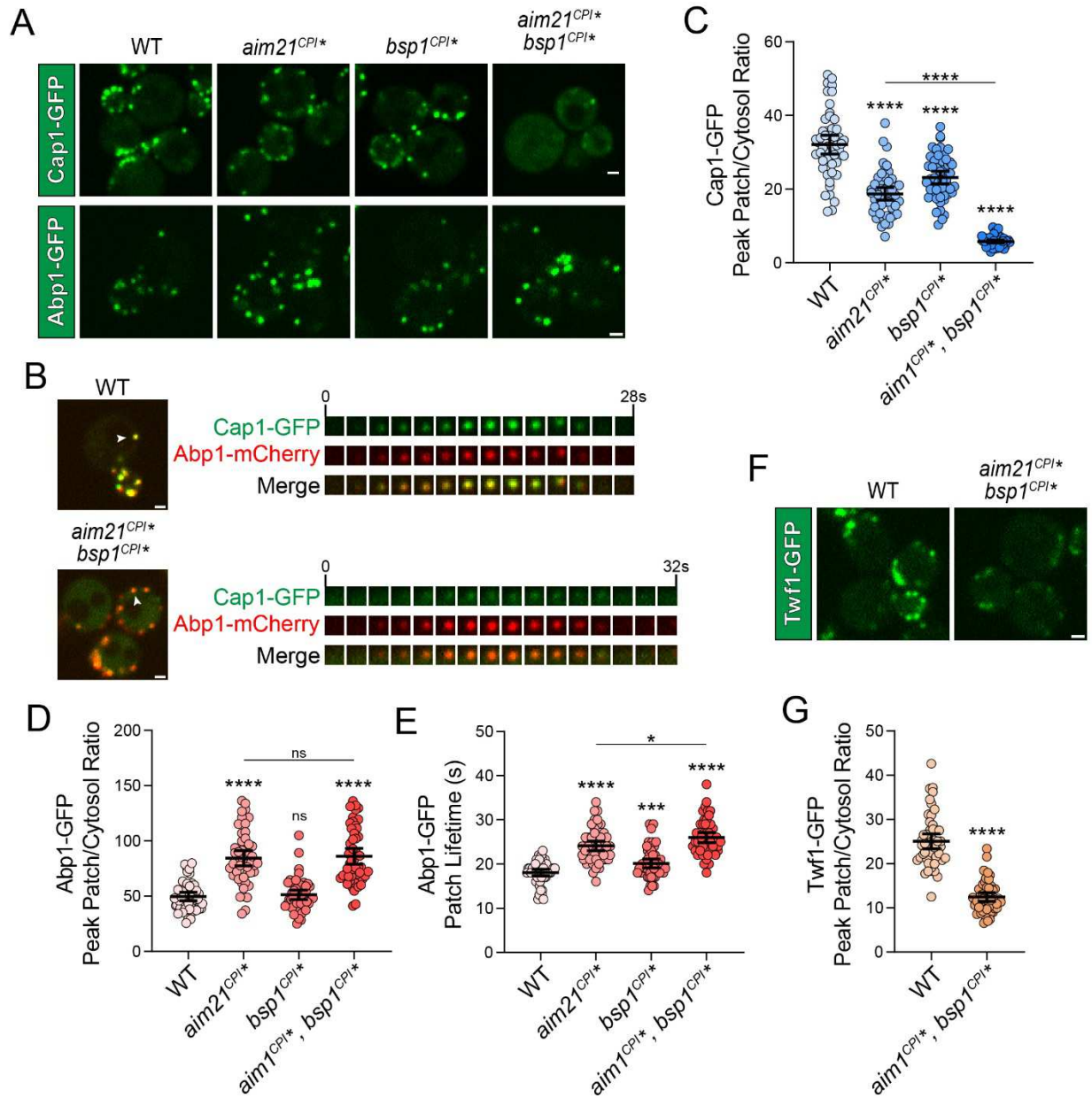


**Figure 3.10: The CPI motifs of Aim21 and Bsp1 are required for proper recruitment of CP to CME sites.** (A, top) Live-cell fluorescence microscopy showing reduced recruitment of Cap1-GFP to endocytic sites in cells with the CPI motifs of Aim21 or Bsp1 mutated (SDY1474, SDY1512), or in cells with the mutations combined (SDY1604). (Bottom) Live-cell fluorescence microscopy showing increased recruitment of Abp1-GFP to endocytic sites in cells with the CPI motif of Aim21 or Bsp1 mutated (SDY1434, SDY1514), or with the mutations combined (SDY1610). Scale bars, 1  $\mu$ m. (B, top) Live-cell fluorescence microscopy showing strong colocalization of Cap1-GFP with Abp1-mCherry at endocytic patches (SDY1698). (Bottom) Live-cell fluorescence microscopy showing reduced recruitment of Cap1-GFP and increased recruitment of Abp1-mCherry to endocytic patches in cells with the CPI motifs of Aim21 and Bsp1 mutated (SDY1702). Endocytic patches used for construction of kymographs to right are

indicated by arrows. Scale bars, 1  $\mu\text{m}$  (C) Quantification of Cap1-GFP peak fluorescence intensity at endocytic patches in wild-type (WT), *aim21<sup>CPI\*</sup>*, *bsp1<sup>CPI\*</sup>* and *aim21<sup>CPI\*</sup>/bsp1<sup>CPI\*</sup>* cells. From left to right, mean peak patch/cytosol ratio = 32.08, 18.73, 23.13, 5.75 and n = 50 for all groups. Error bars, mean with 95% CI. \*\*\*\* $P \leq .0001$ . (D) Quantification of Abp1-GFP peak fluorescence intensity at endocytic patches in wild-type (WT), *aim21<sup>CPI\*</sup>*, *bsp1<sup>CPI\*</sup>* and *aim21<sup>CPI\*</sup>/bsp1<sup>CPI\*</sup>* cells. From left to right, mean peak patch/cytosol ratio = 49.63, 84.36, 51.25, 86.12 and n = 50 for all groups. Error bars, mean with 95% CI. ns=not significant, \*\*\*\* $P \leq .0001$ . (E) Quantification of Abp1-GFP patch lifetime at endocytic patches in wild-type (WT), *aim21<sup>CPI\*</sup>*, *bsp1<sup>CPI\*</sup>* and *aim21<sup>CPI\*</sup>/bsp1<sup>CPI\*</sup>* cells. From left to right, mean patch lifetime = 18.06, 24.12, 20.14, 26.02 and n = 50 for all groups. Error bars, mean with 95% CI. \* $P \leq 0.05$ , \*\*\* $P \leq 0.001$ , \*\*\*\* $P \leq 0.0001$ . (F) Live-cell fluorescence microscopy showing reduced recruitment of Twf1-GFP to endocytic sites in cells with the CPI motifs of Aim21 and Bsp1 mutated (SDY1611). Scale bar, 1  $\mu\text{m}$ . (G) Quantification of Twf1-GFP peak fluorescence intensity at endocytic patches in wild-type (WT) and *aim21<sup>CPI\*</sup>/bsp1<sup>CPI\*</sup>* cells. From left to right, mean peak patch/cytosol ratio = 25.06, 12.49 and n = 50 for all groups. Error bars, mean with 95% CI. \*\*\*\* $P \leq .0001$ .

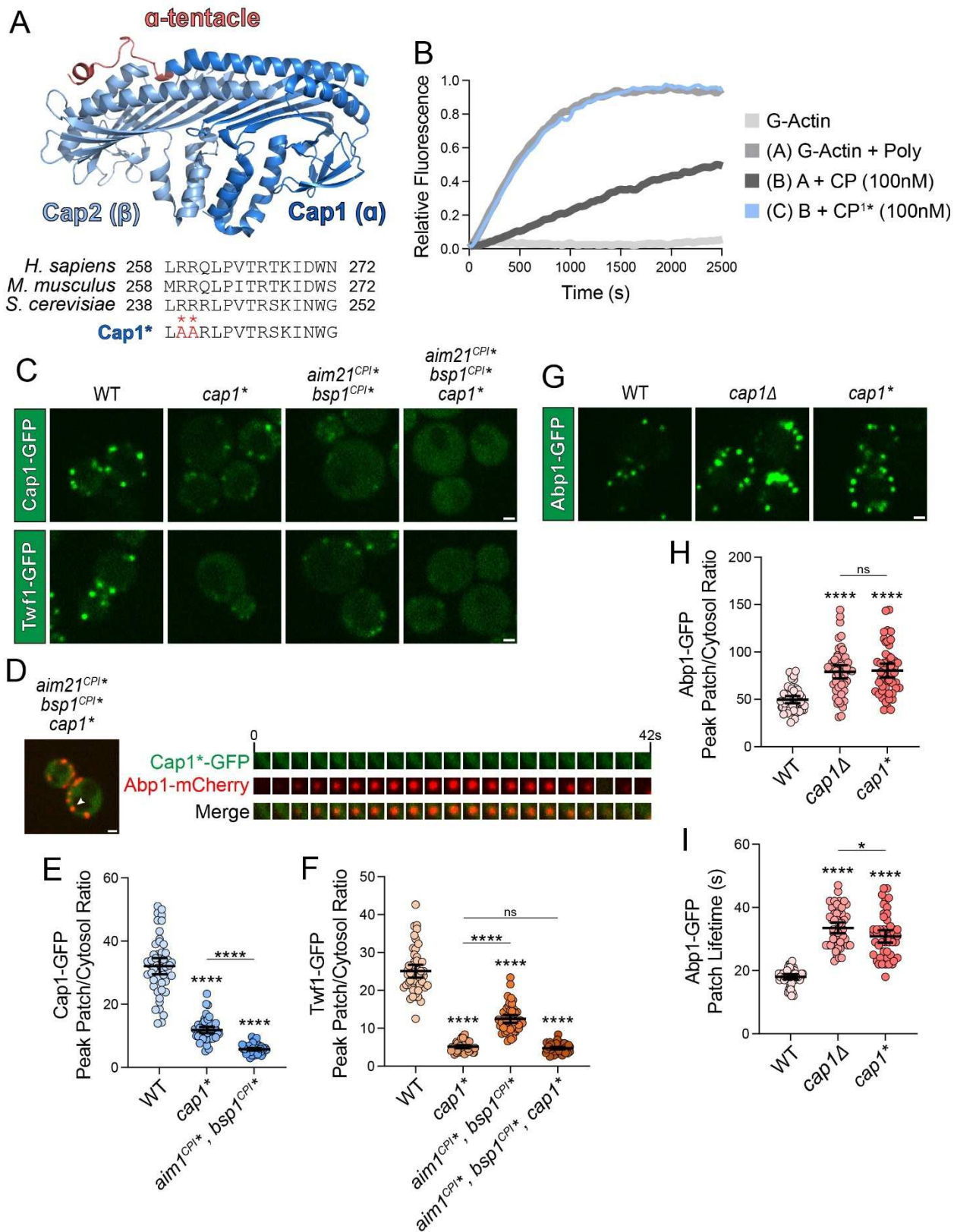


**Figure 3.11: CPs ability to cap barbed ends is required for its localization and function.**

(A, top) Crystal structure of the chicken actin capping protein complex (PDB Entry 3AA7) displayed with the  $\alpha$ -subunit (Cap1) in dark blue and the  $\beta$ -subunit (Cap2) in light blue. The  $\alpha$ -tentacle, which is critical for the capping function of CP, is shown in red. (Bottom) Alignment of the *S. cerevisiae*  $\alpha$ -tentacle sequence with homologs from *H. sapiens* and *M. musculus*. The mutations to Cap1 (Cap1\*) that will be used throughout Figure 7 are displayed in red. (B) Pyrene actin (1 $\mu$ M, 20% labelled) was polymerized in the absence or presence of His-Cap1/2 (CP, 100nM) or His-Cap1\*/2 (CP1\*, 100nM). CP1\* showed no ability to cap actin filaments. (C, top) Live-cell fluorescence microscopy showing reduced recruitment of Cap1-GFP to endocytic sites in cells with the  $\alpha$ -tentacle of Cap1 mutated (SDY1582), the CPI motifs of Aim21 and Bsp1 mutated (SDY1604), or with the mutations combined (SDY1608). (Bottom) Live-cell fluorescence microscopy showing decreased recruitment of Twf1-GFP to endocytic sites in cells with the  $\alpha$ -tentacle of Cap1 mutated (SDY1588), the CPI motifs of Aim21 and Bsp1 mutated (SDY1611), or with the mutations combined (SDY1627). Scale bars, 1  $\mu$ m. (D) Live-cell fluorescence microscopy showing no localization of Cap1\*-GFP with Abp1-mCherry at endocytic patches in cells with the CPI motifs of Aim21 and Bsp1 mutated (SDY1703). Endocytic patch used for construction of kymograph to right is indicated by arrow. Scale bar, 1  $\mu$ m (E) Quantification of Cap1-GFP peak fluorescence intensity at endocytic patches in wild-type (WT), *cap1\** and *aim21<sup>CPI\*</sup>/bsp1<sup>CPI\*</sup>* cells. From left to right, mean peak patch/cytosol ratio = 32.08, 11.86, 5.75 and n = 50 for all groups. Error bars, mean with 95% CI. \*\*\*\**P*  $\leq$  .0001. (F) Quantification of Twf1-GFP peak fluorescence intensity at endocytic patches in wild-type (WT), *cap1\**, *aim21<sup>CPI\*</sup>/bsp1<sup>CPI\*</sup>* and *aim21<sup>CPI\*</sup>/bsp1<sup>CPI\*</sup>/cap1\** cells. From left to right, mean peak patch/cytosol ratio = 25.06, 5.15, 12.49, 4.43 and n = 50 for all groups. Error bars, mean with 95% CI. ns=not significant, \*\*\*\**P*  $\leq$  .0001. (G) Live-cell fluorescence microscopy showing increased recruitment of Abp1-GFP to endocytic sites in cells lacking Cap1 (SDY1480) or with the  $\alpha$ -tentacle of Cap1 mutated (SDY1580), Scale bars, 1  $\mu$ m. (H) Quantification of Abp1-GFP peak fluorescence intensity at endocytic patches in wild-type (WT), *cap1 $\Delta$*  and *cap1\** cells. From left to right, mean peak patch/cytosol ratio = 49.63, 79.03, 80.27 and n = 50 for all groups. Error bars, mean with 95% CI. ns=not significant, \*\*\*\**P*  $\leq$  .0001. (I) Quantification of Abp1-GFP patch lifetime at endocytic patches in wild-type (WT), *cap1 $\Delta$*  and *cap1\** cells. From left to right, mean patch lifetime = 18.06, 33.52, 30.82 and n = 50 for all groups. Error bars, mean with 95% CI. \**P*  $\leq$  0.05, \*\*\*\**P*  $\leq$  0.0001.

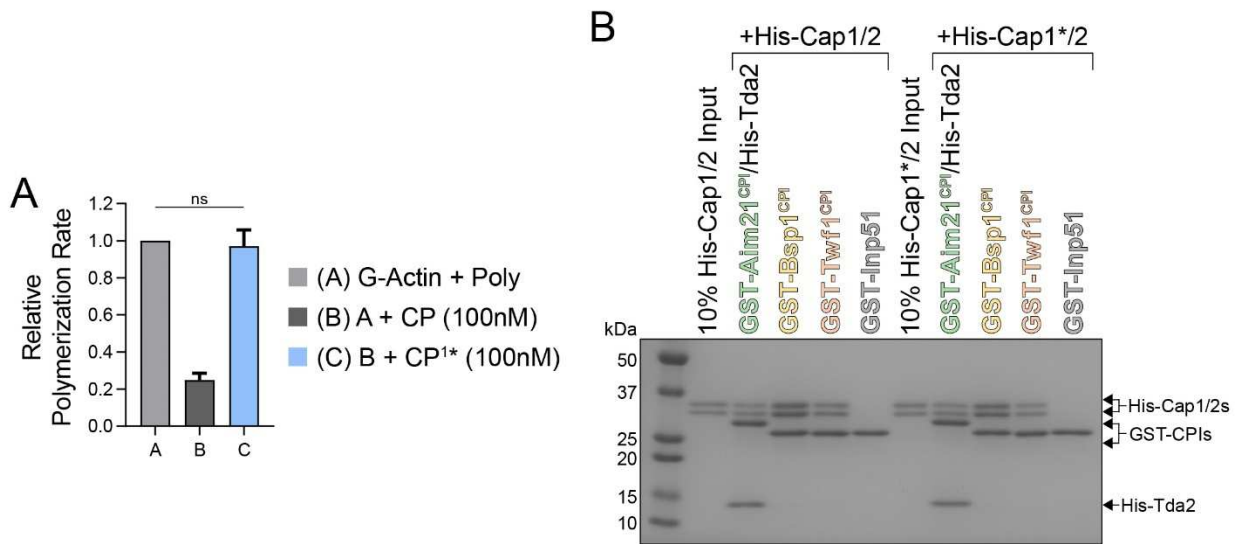


**Figure 3.12: CPs ability to cap barbed ends is required for its localization and function.**

(A) Quantification of the relative polymerization rate from three independent pyrene actin polymerization assays in Figure 7B. From left to right, mean relative polymerization rate = 1.00, 0.25, 0.97. Error bars, mean  $\pm$  SD. ns=not significant. (B) A GST-pulldown assay was performed with GST fused to the CPI motifs of Aim21, Bsp1 and Twf1 or a fragment of Inp51. Each GST fusion protein was incubated with either wild-type CP (His-Cap1/2) or a CP with a mutated His-Cap1 subunit  $\alpha$ -tentacle (His-Cap1\*/2), as indicated in Figure 7A. Aim21 was incubated with His-Tda2 additionally to form the Tda2/Aim21 complex. Bound proteins were analyzed by SDS-PAGE and Coomassie staining. The mutations to His-Cap1\* do not affect the interaction between the CPI motifs and His-Cap1\*/2.

the same efficiency as wild-type CP in a GST pulldown assay, indicating the mutations did not affect the CP:CPI interactions (**Figure 3.12B**).

When the mutant *cap1*<sup>239,240A</sup> (*cap1*<sup>\*</sup>) allele was integrated into the genome of *CAP1*-GFP cells, there was a large recruitment defect in Cap1<sup>\*</sup>-GFP (**Figure 3.11C top, 3.11E**). However, this defect was not as severe as the defect seen in *aim21*<sup>CPI\*</sup>/*bsp1*<sup>CPI\*</sup> cells (**Figure 3.11C top, 3.11E**). When the three mutant alleles were combined in *aim21*<sup>CPI\*</sup>/*bsp1*<sup>CPI\*</sup>/*cap1*<sup>\*</sup> cells, Cap1<sup>\*</sup>-GFP was no longer visible at CME sites, becoming diffuse in the cytosol (**Figure 3.11C top, 3.11D**). While Twf1-GFP recruitment levels were decreased in *aim21*<sup>CPI\*</sup>/*bsp1*<sup>CPI\*</sup> cells compared to wild-type cells, the decrease was more substantial in *cap1*<sup>\*</sup> cells (**Figure 3.11C bottom, 3.11F**). Moreover, the Twf1-GFP recruitment defect in *cap1*<sup>\*</sup> was comparable to that in *aim21*<sup>CPI\*</sup>/*bsp1*<sup>CPI\*</sup>/*cap1*<sup>\*</sup> cells, demonstrating that the ability for CP to cap actin filaments is essential for Twf1 localization (**Figure 3.11C bottom, 3.11F**). To determine if the capping function of CP was essential to the for its function during CME, Abp1-GFP was imaged in cells lacking the CP complex (*cap1* $\Delta$ ) and cells with defective capping (*cap1*<sup>\*</sup>). Indeed, the increase in recruitment of Abp1-GFP was comparable between the cells, and Abp1-GFP persisted at endocytic patches for a similar, increased time period (**Figure 3.11G, 3.11H, 3.11I**). While the patch lifetime of Abp1-GFP in *cap1* $\Delta$  was significantly longer than in *cap1*<sup>\*</sup> cells, both were increased substantially from wild-type cells, with average patch lifetimes of 18.06, 33.52 and 30.82 seconds for wild-type, *cap1* $\Delta$  and *cap1*<sup>\*</sup> cells, respectively (**Figure 3.11I**). Thus, while CPI motif-based recruitment is necessary for proper CP localization, the ability for CP to bind barbed ends is essential for its function at endocytic sites.

### 3.4 Discussion

Until the recent discovery of the Aim21 CPI motif, CP regulators were not thought to be present in yeast. Here, we uncovered a novel CPI motif-containing protein, Bsp1, and demonstrate that it has a redundant function with Aim21 in recruiting CP to CME sites. In contrast, the unconventional CPI motif on twinfilin is not important for recruitment of CP, but for twinfilin itself to localize to CME sites. Cells with a defective twinfilin CPI motif have a phenotype consistent with a defect in the turnover of CP. Together, our findings begin to shed light on how multiple CPI motifs can be working at the same subcellular location to regulate CP activity.

CPI motif proteins have been demonstrated to aid in the localization of CP to endocytic sites in mammalian cells [102, 120]. Our data support a conserved function for the yeast CME factors Aim21 and Bsp1, helping to recruit CP to cortical actin patches. While disrupting the CPI motif of Aim21 and Bsp1 separately causes a mild yet measurable CP localization defect, the defect when neither Bsp1 nor Aim21 can interact with CP is severe. Moreover, this defect appears to be physiologically important, as the actin polymerization stage of CME is slowed considerably in *aim21<sup>CPI\*</sup>/bsp1<sup>CPI\*</sup>* cells compared to wild-type cells. Given that the Bsp1 CPI motif has a ~10-fold higher affinity for capping protein than Aim21, it's a mild surprise that the CP recruitment defect is weaker in *bsp1<sup>CPI\*</sup>* cells than *aim21<sup>CPI\*</sup>* cells. However, our fluorescence microscopy imaging suggests Aim21-GFP is expressed at considerably higher levels than Bsp1-GFP, suggesting that the difference in phenotypes could be due to having more Aim21 in the cell. Taken together, the similarities between Aim21 and Bsp1 in their regulation of CP, along with the mild defect seen in CP localization when the CPI motif of either is mutated separately, supports Aim21 and Bsp1 having a largely redundant function in localizing CP to cortical actin patches.

Our *in vitro* actin polymerization assays suggested that Aim21 and Bsp1 could potentially be acting as filament uncapping proteins, a function that has been hypothesized for

CPI motifs [126]. However, our cell biological data argues against this. With a defect in uncapping, increased levels of CP at endocytic sites would be expected, as CP continues to accumulate as actin polymerizes. Moreover, the longer patch lifetime should begin to deplete the cytosol of CP. As the phenotype we see in *aim21<sup>CPI\*</sup>/bsp1<sup>CPI\*</sup>* cells is opposite this, it's unlikely that Aim21 or Bsp1 function physiologically as filament uncapping proteins. Given that Aim21 and Bsp1 display a partial inhibition of CP *in vitro*, it's likely that Aim21 and Bsp1 recruit CP as a transiently active capper. More work will need to be done to determine if this inhibition is important for the *in vivo* regulation of CP.

While *aim21<sup>CPI\*</sup>/bsp1<sup>CPI\*</sup>* cells do not have a phenotype consistent with a filament uncapping function, twinfilin does. In cells with a mutated twinfilin CPI motif, CP accumulates at high levels at CME sites and is depleted from the cytosol, both consistent with a defect in turnover of CP. While the CPI motif of twinfilin did not show activity consistent with uncapping in our actin polymerization assays, the twin ADF-H domains could be responsible for filament uncapping. Accordingly, solving the crystal structure of twinfilin bound to capping protein and two ADP-bound actin monomers led to the suggestion that twinfilin alters the conformation of the two closest actin subunits to CP, placing the monomers in a conformation that would induce severing of the filament [157]. Together, our data support the twinfilin CPI motif functioning to target twinfilin to CME sites, and specifically barbed ends, where it likely works to turnover CP. More work will be needed to understand the mechanism of twinfilin-induced uncapping.

### **3.5 Materials and Methods**

#### *3.5.1 Plasmids and yeast strains*

All cloning was performed using the In-fusion HD Cloning System (Takara Bio Inc.). Plasmids for bacterial expression of recombinant glutathione-S-transferase (GST)

CPI motif fusion proteins were generated through PCR amplification of the corresponding *AIM21*, *BSP1*, *TWF1* or *INP51* DNA sequence from yeast genomic DNA and cloned into pGEX-5X-1. Generation of plasmids for bacterial expression of recombinant His-Tda2, His-Cap1 and His-Cap2 was described previously [130]. Plasmids for yeast two-hybrid analysis of Bsp1 fragments were generated by PCR amplification of the corresponding DNA fragments of *BSP1* and cloned into pGBT9. Generation of pGBT9-Aim21 fusions and the pGAD424-SH3 domain fusion library was described previously [83]. All plasmids encoding mutant recombinant proteins were engineered by PCR-based mutagenesis using the In-fusion system. All constructs were verified by DNA sequencing.

For plasmids designed to integrate mutations into the *S. cerevisiae* genome, fragments containing the full ORF of either *AIM21*, *BSP1*, *CAP1*, *CAP2*, *TWF1* plus 100 base pairs upstream and downstream were generated by PCR amplification from yeast genomic DNA and cloned into pUC18. PCR-based mutagenesis of pUC18-*AIM21*, pUC18-*BSP1*, pUC18-*CAP1*, pUC18-*CAP2* and pUC18-*TWF1* yielded the templates for genetic manipulation.

The background *S. cerevisiae* strain BY4741 (*MATa*, *his3Δ1*, *leu2Δ0*, *met15Δ0*, *ura3Δ0*) was used throughout this study. Wild-type GFP-expressing strains (Aim21-GFP, Abp1-GFP, Bsp1-GFP, Cap1-GFP and Twf1-GFP) were obtained from the yeast GFP library (Invitrogen). Integration of mutant alleles into the yeast genome was performed using a two-step gene replacement approach described previously [159]. As an example, SDY1474 (*MATa*, *his3Δ1*, *leu2Δ0*, *met15Δ0*, *ura3Δ0*, *CAP1-GFP::HIS3*, *aim21<sup>504,507,509E</sup>*) was created from the Cap1-GFP library strain (*MATa*, *his3Δ1*, *leu2Δ0*, *met15Δ0*, *ura3Δ0*, *CAP1-GFP::HIS3*). In step one, *URA3* was amplified from pRS316 [160] using primers that impart 50 base pairs of homology to the sequences directly upstream and downstream of the *AIM21* ORF, then transformed [161] into the Cap1-GFP library strain to generate intermediate strain SDY1292 (*MATa*, *his3Δ1*, *leu2Δ0*, *met15Δ0*, *ura3Δ0*, *CAP1-GFP::HIS3*, *aim21Δ::URA3*). Second, the intermediate strain SDY1292 was transformed with a DNA fragment containing the mutant allele *aim21<sup>604,507,509E</sup>*.

Cells were grown overnight on plates containing rich media, then replica plated onto plates containing 5-fluoroorotic acid (5-FOA). Colonies that grew on plates containing 5-FOA represented cells in which the *aim21*<sup>505,507,509E</sup> allele replaced *URA3*. C-terminal tagging of the *ABP1*, *CAP1* and *MYO1* ORFs with mCherry was accomplished through PCR amplification of pFA6a-mCherry-KANMX6 and homologous recombination. All integrants were verified by PCR amplification of genomic DNA and DNA sequencing of the purified PCR product. All yeast strains generated in this study are listed in Table. Numerous strains utilized in this study were generated previously [130].

### 3.5.2 Biochemical Methods

Recombinant 6-histidine (His) and GST fusion proteins were expressed in BL21 codon plus *E. coli* and purified using HisPur Cobalt Resin (Thermo Scientific) or Glutathione Sepharose 4 Fast Flow (GE Healthcare) as previously described [162]. All proteins were dialyzed in PBS (137mM NaCl, 2.7mM KCl, 10mM Na<sub>2</sub>HPO<sub>4</sub>, 2mM KH<sub>2</sub>PO<sub>4</sub>). Protein concentrations were determined using absorbance at 280 nm and the corresponding extinction coefficient.

GST pulldown assays were performed as previously described [163]. In short, recombinant GST-tagged proteins (10 µg) were incubated with glutathione Sepharose resin for 30 minutes at 4°C. Equimolar His-tagged protein was added and incubated for an additional 30 minutes. Resin was washed 3 times in PBS containing Triton X-100 (0.1-0.5%) and boiled in Laemmli sample buffer. Bound proteins were analyzed by SDS-PAGE and Coomassie staining. All pulldowns were repeated in an independent experiment to ensure reproducibility.

Total yeast extracts were obtained as previously described [159]. Immunoblotting of cell extract was performed using anti-GFP (Sigma). For Aim21-GFP immunoblotting,

transfer buffer was supplemented with 0.1% SDS for increased transfer efficiency of Aim21-GFP.

All peptides utilized in fluorescence polarization and pyrene actin polymerization assays were purchased from GenScript. The sequences of peptides were as followed: (FITC-Aim21<sup>CPI</sup>) FITC-KTGPLGGTRRGRGPRGRKLPKVASVEKIEEDDNTNKIEIFNNWNVSS, (Aim21<sup>CPI</sup>) KTGPLGGTRRGRGPRGRKLPKVASVEKIEEDDNTNKIEIFNNWNVSS, (Aim21<sup>CPI\*</sup>) KTGPLGGTRRGEGPEGEKLPKVASVEKIEEDDNTNKIEIFNNWNVSS, (FITC-Bsp1<sup>CPI</sup>) FITC-KETKPLVHPNKNRTRGPRRKLPTRV, (Bsp1<sup>CPI</sup>) KETKPLVHPNKNRTRGPRRKLPTRV, (Bsp1<sup>CPI\*</sup>) KETKPLVHPNKNETEGPERKLPTRV, (FITC-Twf1<sup>CPI</sup>) FITC-SNPDLPNKSNLKFNPKGPLRKRRT, (Twf1<sup>CPI</sup>) SNPDLPNKSNLKFNPKGPLRKRRT, (Twf1<sup>CPI\*</sup>) SNPDLPNKSNLKFNEPEGLEKRRT. Peptide concentrations were determined using absorbance at 205 nm.

### 3.5.3 Fluorescence polarization assays

Fluorescence polarization assays were performed as previously described [59]. Briefly, FITC-labelled peptides were titrated with a 24-point dilution series of His-Cap1/2 in experiment buffer (137 mM NaCl, 2.7 mM KCl, 10 mM Na<sub>2</sub>HPO<sub>4</sub>, 2 mM KH<sub>2</sub>PO<sub>4</sub>, 0.01% Triton X-100, 2 mM DTT). For Aim21 and Twf1, 10nM of FITC labelled peptide was utilized, while 2.5nM of FITC labelled peptide was used for Bsp1. His-Tda2 was included at a final concentration of 25  $\mu$ M for all experiments using the Aim21 peptide. Data were collected using 384-well non-binding polystyrene microplates (Greiner Bio-one) in a Victor<sup>3</sup> V microplate reader (PerkinElmer) at room temperature following a 30-minute incubation. Three technical replicates were performed per experiment and each experiment was performed independently 3 times. The dissociation constants for each independent experiment were determined by curve fitting the data to a one-site binding isotherm using GraphPad Prism Software. The reported dissociation constants correspond to the average (and SEM) of values obtained in the 3 independent experiments.

#### 3.5.4 *Pyrene actin polymerization assays*

All pyrene actin polymerization assays were performed using rabbit skeletal muscle actin (Cytoskeleton, Denver, CO). Unlabeled-actin and Pyrene-actin were diluted to a concentration of 0.5 mg/mL in G-buffer (5 mM Tris-HCl pH 8, 0.2 mM CaCl<sub>2</sub>, 0.2 mM ATP, 0.5 mM DTT) and left on ice to allow for actin depolymerization. Actin was subsequently centrifuged at 100,000 x g in a TLA100.3 rotor (Beckman Coulter) at 4°C for 1 h. A 2.5 μM stock of 20% pyrene-labelled actin was prepared as described [179]. Reactions were performed with a final volume of 100 μL in 96-well non-binding polystyrene microplates (Greiner Bio-one). 10 μL of exchange buffer (5 mM Tris, 10 mM EGTA, 1 mM MgCl<sub>2</sub>) was added to 40 μL of actin stock in a 96-well plate and incubated at room temperature for 10 minutes. To induce polymerization, a 50 μL mix containing the proteins of interest and 10 μL of 10x Polymerization buffer (Final concentration 50 mM KCl, 2 mM MgCl<sub>2</sub>, 1mM ATP, 1mM EGTA) was added to the 96-well plate. Polymerization was measured over time using a Victor<sup>3</sup> V microplate reader (Perkin Elmer-Cetus, Waltham, MA) with excitation and emission wavelengths of 365 nm and 406 nm, respectively. Actin polymerization rates were calculated from the slope of the linear portion of assembly curves (25–50% polymerization), and normalized to the Actin with polymerization buffer rate. Statistical significance between groups was determined using an unpaired t test (GraphPad Prism Software).

#### 3.5.5 *Fluorescence microscopy*

Fluorescence microscopy was performed as previously described using an IX81 spinning-disk confocal microscope (Olympus) with an Andor iXon Ultra camera (Oxford Instruments) and a 100X 1.40 NA objective [164]. Briefly, cells grown overnight were diluted in synthetic complete media and grown to early logarithmic phase, then imaged at room temperature. Time-

lapse videos were generated by collecting an image each second for 90 seconds for single-color microscopy, and every 2 seconds for 60 seconds for two-color microscopy. Slidebook 6 software (Intelligent Imaging Innovations) was used for quantification of patch intensities and lifetimes. For quantification of peak patch/cytosol ratios, masks were drawn over individual endocytic sites to track the fluorescence of the patch over time. Patch intensity, average cytosol intensity and average background intensity were recorded for the frame in which the patch intensity was at its maximum. After subtracting the average background from both values, the values were divided to give the peak patch/cytosol ratio. For quantification of patch lifetimes, masks were drawn over individual endocytic patches to track the maximum fluorescence of each patch over time. Prior to quantification, a threshold fluorescence value was established for each fluorescently tagged protein to establish a start and finish value for the endocytic event. The patch lifetime was determined by the number of frames in which the maximum patch fluorescence was above the threshold value. Statistical significance between groups was determined using an unpaired t test for all microscopy data (GraphPad Prism Software). Representative images for groups that were directly compared were displayed with equal brightness and contrast settings.

### 3.5.6 *Yeast two-hybrid assay*

AH109 cells were co-transformed with pGBT9 and pGAD424 vectors (Takara Bio Inc.) and grown on synthetic dropout media lacking leucine and tryptophan. Successful co-transformants were grown overnight in synthetic dropout media lacking leucine and tryptophan. The following day, cells were diluted to an O.D. 600 of 0.2 in sterile water. Diluted cells were spotted on synthetic dropout media lacking leucine and tryptophan (control), or lacking leucine, tryptophan and histidine.

## REFERENCES

1. Roth, T.F. and K.R. Porter, *Yolk protein uptake in the oocyte of the mosquito Aedes aegypti*. L. The Journal of cell biology, 1964. **20**(2): p. 313-332.
2. Pearse, B.M., *Clathrin: a unique protein associated with intracellular transfer of membrane by coated vesicles*. Proceedings of the National Academy of Sciences, 1976. **73**(4): p. 1255-1259.
3. Crowther, R.A. and B.M. Pearse, *Assembly and packing of clathrin into coats*. J Cell Biol, 1981. **91**(3 Pt 1): p. 790-7.
4. Raths, S., et al., *end3 and end4: two mutants defective in receptor-mediated and fluid-phase endocytosis in Saccharomyces cerevisiae*. The Journal of cell biology, 1993. **120**(1): p. 55-65.
5. Wendland, B., et al., *A novel fluorescence-activated cell sorter-based screen for yeast endocytosis mutants identifies a yeast homologue of mammalian eps15*. The Journal of cell biology, 1996. **135**(6): p. 1485-1500.
6. Farrell, K.B., C. Grossman, and S.M. Di Pietro, *New Regulators of Clathrin-Mediated Endocytosis Identified in Saccharomyces cerevisiae by Systematic Quantitative Fluorescence Microscopy*. Genetics, 2015. **201**(3): p. 1061-70.
7. Munn, A.L. and H. Riezman, *Endocytosis is required for the growth of vacuolar H (+)-ATPase-defective yeast: identification of six new END genes*. The Journal of cell biology, 1994. **127**(2): p. 373-386.
8. Kaksonen, M., Y. Sun, and D.G. Drubin, *A pathway for association of receptors, adaptors, and actin during endocytic internalization*. Cell, 2003. **115**(4): p. 475-87.
9. Kaksonen, M., C.P. Toret, and D.G. Drubin, *A modular design for the clathrin- and actin-mediated endocytosis machinery*. Cell, 2005. **123**(2): p. 305-20.
10. Carroll, S.Y., et al., *Analysis of yeast endocytic site formation and maturation through a regulatory transition point*. Mol Biol Cell, 2012. **23**(4): p. 657-68.
11. Reider, A. and B. Wendland, *Endocytic adaptors--social networking at the plasma membrane*. J Cell Sci, 2011. **124**(Pt 10): p. 1613-22.
12. Boettner, D.R., et al., *The F-BAR protein Syp1 negatively regulates WASp-Arp2/3 complex activity during endocytic patch formation*. Curr Biol, 2009. **19**(23): p. 1979-87.
13. Gagny, B., et al., *A novel EH domain protein of Saccharomyces cerevisiae, Ede1p, involved in endocytosis*. J Cell Sci, 2000. **113** ( Pt 18): p. 3309-19.
14. Galletta, B.J., O.L. Mooren, and J.A. Cooper, *Actin dynamics and endocytosis in yeast and mammals*. Curr Opin Biotechnol, 2010. **21**(5): p. 604-10.
15. Winter, D., et al., *The complex containing actin-related proteins Arp2 and Arp3 is required for the motility and integrity of yeast actin patches*. Curr Biol, 1997. **7**(7): p. 519-29.
16. Sun, Y., A.C. Martin, and D.G. Drubin, *Endocytic internalization in budding yeast requires coordinated actin nucleation and myosin motor activity*. Dev Cell, 2006. **11**(1): p. 33-46.
17. Friesen, H., et al., *Characterization of the yeast amphiphysins Rvs161p and Rvs167p reveals roles for the Rvs heterodimer in vivo*. Mol Biol Cell, 2006. **17**(3): p. 1306-21.
18. Peter, B.J., et al., *BAR domains as sensors of membrane curvature: the amphiphysin BAR structure*. Science, 2004. **303**(5657): p. 495-9.
19. Idrissi, F.Z., et al., *Distinct acto/myosin-I structures associate with endocytic profiles at the plasma membrane*. J Cell Biol, 2008. **180**(6): p. 1219-32.

20. Smaczynska-de Rooij, I.I., et al., *A role for the dynamin-like protein Vps1 during endocytosis in yeast*. J Cell Sci, 2010. **123**(Pt 20): p. 3496-506.
21. Nannapaneni, S., et al., *The yeast dynamin-like protein Vps1:vps1 mutations perturb the internalization and the motility of endocytic vesicles and endosomes via disorganization of the actin cytoskeleton*. Eur J Cell Biol, 2010. **89**(7): p. 499-508.
22. Kaksonen, M. and A. Roux, *Mechanisms of clathrin-mediated endocytosis*. Nat Rev Mol Cell Biol, 2018. **19**(5): p. 313-326.
23. Sekiya-Kawasaki, M., et al., *Dynamic phosphoregulation of the cortical actin cytoskeleton and endocytic machinery revealed by real-time chemical genetic analysis*. The Journal of cell biology, 2003. **162**(5): p. 765-772.
24. Cope, M.J.T.V., et al., *Novel protein kinases Ark1p and Prk1p associate with and regulate the cortical actin cytoskeleton in budding yeast*. The Journal of cell biology, 1999. **144**(6): p. 1203-1218.
25. Zeng, G. and M. Cai, *Regulation of the actin cytoskeleton organization in yeast by a novel serine/threonine kinase Prk1p*. The Journal of cell biology, 1999. **144**(1): p. 71-82.
26. Watson, H.A., et al., *In vivo role for actin-regulating kinases in endocytosis and yeast epsin phosphorylation*. Molecular Biology of the Cell, 2001. **12**(11): p. 3668-3679.
27. Toret, C.P., et al., *Multiple pathways regulate endocytic coat disassembly in Saccharomyces cerevisiae for optimal downstream trafficking*. Traffic, 2008. **9**(5): p. 848-859.
28. Sun, Y., et al., *PtdIns (4, 5) P2 turnover is required for multiple stages during clathrin- and actin-dependent endocytic internalization*. The Journal of cell biology, 2007. **177**(2): p. 355-367.
29. Pishvaei, B., et al., *A yeast DNA J protein required for uncoating of clathrin-coated vesicles in vivo*. Nat Cell Biol, 2000. **2**(12): p. 958-63.
30. Aghamohammadzadeh, S. and K.R. Ayscough, *Differential requirements for actin during yeast and mammalian endocytosis*. Nat Cell Biol, 2009. **11**(8): p. 1039-42.
31. Basu, R., E.L. Munteanu, and F. Chang, *Role of turgor pressure in endocytosis in fission yeast*. Mol Biol Cell, 2014. **25**(5): p. 679-87.
32. Merrifield, C.J., et al., *Imaging actin and dynamin recruitment during invagination of single clathrin-coated pits*. Nat Cell Biol, 2002. **4**(9): p. 691-8.
33. Taylor, M.J., D. Perrais, and C.J. Merrifield, *A high precision survey of the molecular dynamics of mammalian clathrin-mediated endocytosis*. PLoS Biol, 2011. **9**(3): p. e1000604.
34. Merrifield, C.J., D. Perrais, and D. Zenisek, *Coupling between clathrin-coated-pit invagination, cortactin recruitment, and membrane scission observed in live cells*. Cell, 2005. **121**(4): p. 593-606.
35. Saffarian, S., E. Cocucci, and T. Kirchhausen, *Distinct dynamics of endocytic clathrin-coated pits and coated plaques*. PLoS Biol, 2009. **7**(9): p. e1000191.
36. Huang, F., et al., *Analysis of clathrin-mediated endocytosis of epidermal growth factor receptor by RNA interference*. J Biol Chem, 2004. **279**(16): p. 16657-61.
37. Motley, A., et al., *Clathrin-mediated endocytosis in AP-2-depleted cells*. J Cell Biol, 2003. **162**(5): p. 909-18.
38. Newpher, T.M. and S.K. Lemmon, *Clathrin is important for normal actin dynamics and progression of Sla2p-containing patches during endocytosis in yeast*. Traffic, 2006. **7**(5): p. 574-88.
39. Water, R.D., J.R. Pringle, and L.J. Kleinsmith, *Identification of an actin-like protein and of its messenger ribonucleic acid in Saccharomyces cerevisiae*. J Bacteriol, 1980. **144**(3): p. 1143-51.
40. Bretscher, A., *Polarized growth and organelle segregation in yeast: the tracks, motors, and receptors*. J Cell Biol, 2003. **160**(6): p. 811-6.

41. Bi, E., et al., *Involvement of an actomyosin contractile ring in Saccharomyces cerevisiae cytokinesis*. J Cell Biol, 1998. **142**(5): p. 1301-12.
42. Tolliday, N., L. VerPlank, and R. Li, *Rho1 directs formin-mediated actin ring assembly during budding yeast cytokinesis*. Curr Biol, 2002. **12**(21): p. 1864-70.
43. Ayscough, K.R., et al., *High rates of actin filament turnover in budding yeast and roles for actin in establishment and maintenance of cell polarity revealed using the actin inhibitor latrunculin-A*. J Cell Biol, 1997. **137**(2): p. 399-416.
44. Lin, M.C., et al., *Overlapping and distinct functions for cofilin, coronin and Aip1 in actin dynamics in vivo*. J Cell Sci, 2010. **123**(Pt 8): p. 1329-42.
45. Young, M.E., J.A. Cooper, and P.C. Bridgman, *Yeast actin patches are networks of branched actin filaments*. J Cell Biol, 2004. **166**(5): p. 629-35.
46. Kaksonen, M., C.P. Toret, and D.G. Drubin, *Harnessing actin dynamics for clathrin-mediated endocytosis*. Nat Rev Mol Cell Biol, 2006. **7**(6): p. 404-14.
47. Akamatsu, M., et al., *Principles of self-organization and load adaptation by the actin cytoskeleton during clathrin-mediated endocytosis*. Elife, 2020. **9**.
48. Goode, B.L., J.A. Eskin, and B. Wendland, *Actin and endocytosis in budding yeast*. Genetics, 2015. **199**(2): p. 315-58.
49. Moseley, J.B. and B.L. Goode, *The yeast actin cytoskeleton: from cellular function to biochemical mechanism*. Microbiol Mol Biol Rev, 2006. **70**(3): p. 605-45.
50. Sept, D. and J.A. McCammon, *Thermodynamics and kinetics of actin filament nucleation*. Biophys J, 2001. **81**(2): p. 667-74.
51. Welch, M.D., et al., *The human Arp2/3 complex is composed of evolutionarily conserved subunits and is localized to cellular regions of dynamic actin filament assembly*. J Cell Biol, 1997. **138**(2): p. 375-84.
52. Mullins, R.D., J.A. Heuser, and T.D. Pollard, *The interaction of Arp2/3 complex with actin: nucleation, high affinity pointed end capping, and formation of branching networks of filaments*. Proc Natl Acad Sci U S A, 1998. **95**(11): p. 6181-6.
53. Winter, D.C., E.Y. Choe, and R. Li, *Genetic dissection of the budding yeast Arp2/3 complex: a comparison of the in vivo and structural roles of individual subunits*. Proc Natl Acad Sci U S A, 1999. **96**(13): p. 7288-93.
54. Robinson, R.C., et al., *Crystal structure of Arp2/3 complex*. Science, 2001. **294**(5547): p. 1679-84.
55. Welch, M.D., et al., *Interaction of human Arp2/3 complex and the Listeria monocytogenes ActA protein in actin filament nucleation*. Science, 1998. **281**(5373): p. 105-8.
56. Winter, D., T. Lechler, and R. Li, *Activation of the yeast Arp2/3 complex by Bee1p, a WASP-family protein*. Curr Biol, 1999. **9**(9): p. 501-4.
57. Rodal, A.A., et al., *Conformational changes in the Arp2/3 complex leading to actin nucleation*. Nat Struct Mol Biol, 2005. **12**(1): p. 26-31.
58. Rodal, A.A., et al., *Negative regulation of yeast WASp by two SH3 domain-containing proteins*. Curr Biol, 2003. **13**(12): p. 1000-8.
59. Feliciano, D., et al., *A second Las17 monomeric actin-binding motif functions in Arp2/3-dependent actin polymerization during endocytosis*. Traffic, 2015. **16**(4): p. 379-97.
60. Evangelista, M., et al., *A role for myosin-I in actin assembly through interactions with Vrp1p, Bee1p, and the Arp2/3 complex*. J Cell Biol, 2000. **148**(2): p. 353-62.
61. Lechler, T., A. Shevchenko, and R. Li, *Direct involvement of yeast type I myosins in Cdc42-dependent actin polymerization*. J Cell Biol, 2000. **148**(2): p. 363-73.
62. Amatruda, J.F. and J.A. Cooper, *Purification, characterization, and immunofluorescence localization of Saccharomyces cerevisiae capping protein*. J Cell Biol, 1992. **117**(5): p. 1067-76.

63. Amatruda, J.F., et al., *Disruption of the actin cytoskeleton in yeast capping protein mutants*. Nature, 1990. **344**(6264): p. 352-4.
64. Okada, K., et al., *Aip1 and cofilin promote rapid turnover of yeast actin patches and cables: a coordinated mechanism for severing and capping filaments*. Mol Biol Cell, 2006. **17**(7): p. 2855-68.
65. Michelot, A., et al., *Actin filament elongation in Arp2/3-derived networks is controlled by three distinct mechanisms*. Dev Cell, 2013. **24**(2): p. 182-95.
66. Berro, J. and T.D. Pollard, *Synergies between Aip1p and capping protein subunits (Acp1p and Acp2p) in clathrin-mediated endocytosis and cell polarization in fission yeast*. Mol Biol Cell, 2014. **25**(22): p. 3515-27.
67. Planade, J., et al., *Mechanical stiffness of reconstituted actin patches correlates tightly with endocytosis efficiency*. PLoS Biol, 2019. **17**(10): p. e3000500.
68. Karpova, T.S., M.M. Lepetit, and J.A. Cooper, *Mutations that enhance the cap2 null mutant phenotype in Saccharomyces cerevisiae affect the actin cytoskeleton, morphogenesis and pattern of growth*. Genetics, 1993. **135**(3): p. 693-709.
69. Adams, A.E., J.A. Cooper, and D.G. Drubin, *Unexpected combinations of null mutations in genes encoding the actin cytoskeleton are lethal in yeast*. Mol Biol Cell, 1993. **4**(5): p. 459-68.
70. Gandhi, M., et al., *GMF is a cofilin homolog that binds Arp2/3 complex to stimulate filament debranching and inhibit actin nucleation*. Curr Biol, 2010. **20**(9): p. 861-7.
71. Goode, B.L., M.O. Sweeney, and J.A. Eskin, *GMF as an Actin Network Remodeling Factor*. Trends Cell Biol, 2018. **28**(9): p. 749-760.
72. Lappalainen, P. and D.G. Drubin, *Cofilin promotes rapid actin filament turnover in vivo*. Nature, 1997. **388**(6637): p. 78-82.
73. Moon, A.L., et al., *Cofilin is an essential component of the yeast cortical cytoskeleton*. J Cell Biol, 1993. **120**(2): p. 421-35.
74. Galkin, V.E., et al., *Remodeling of actin filaments by ADF/cofilin proteins*. Proc Natl Acad Sci U S A, 2011. **108**(51): p. 20568-72.
75. Rodal, A.A., et al., *Aip1p interacts with cofilin to disassemble actin filaments*. J Cell Biol, 1999. **145**(6): p. 1251-64.
76. Balcer, H.I., et al., *Coordinated regulation of actin filament turnover by a high-molecular-weight Srv2/CAP complex, cofilin, profilin, and Aip1*. Curr Biol, 2003. **13**(24): p. 2159-69.
77. Goode, B.L., D.G. Drubin, and P. Lappalainen, *Regulation of the cortical actin cytoskeleton in budding yeast by twinfilin, a ubiquitous actin monomer-sequestering protein*. J Cell Biol, 1998. **142**(3): p. 723-33.
78. Chaudhry, F., et al., *A central role for the WH2 domain of Srv2/CAP in recharging actin monomers to drive actin turnover in vitro and in vivo*. Cytoskeleton (Hoboken), 2010. **67**(2): p. 120-33.
79. Hess, D.C., et al., *Computationally driven, quantitative experiments discover genes required for mitochondrial biogenesis*. PLoS Genet, 2009. **5**(3): p. e1000407.
80. Huh, W.K., et al., *Global analysis of protein localization in budding yeast*. Nature, 2003. **425**(6959): p. 686-91.
81. Burston, H.E., et al., *Regulators of yeast endocytosis identified by systematic quantitative analysis*. J Cell Biol, 2009. **185**(6): p. 1097-110.
82. Reid, R.J., et al., *Selective ploidy ablation, a high-throughput plasmid transfer protocol, identifies new genes affecting topoisomerase I-induced DNA damage*. Genome Res, 2011. **21**(3): p. 477-86.
83. Farrell, K.B., et al., *Novel function of a dynein light chain in actin assembly during clathrin-mediated endocytosis*. J Cell Biol, 2017. **216**(8): p. 2565-2580.
84. Gavin, A.C., et al., *Proteome survey reveals modularity of the yeast cell machinery*. Nature, 2006. **440**(7084): p. 631-6.

85. Shin, M., et al., *Yeast Aim21/Tda2 both regulates free actin by reducing barbed end assembly and forms a complex with Cap1/Cap2 to balance actin assembly between patches and cables*. *Mol Biol Cell*, 2018. **29**(8): p. 923-936.
86. Wicky, S., S. Frischmuth, and B. Singer-Krüger, *Bsp1p/Ypr171p is an adapter that directly links some synaptojanin family members to the cortical actin cytoskeleton in yeast*. *FEBS Lett*, 2003. **537**(1-3): p. 35-41.
87. Wright, D.J., et al., *The Saccharomyces cerevisiae actin cytoskeletal component Bsp1p has an auxiliary role in actomyosin ring function and in the maintenance of bud-neck structure*. *Genetics*, 2008. **178**(4): p. 1903-14.
88. Isenberg, G., U. Aebi, and T.D. Pollard, *An actin-binding protein from Acanthamoeba regulates actin filament polymerization and interactions*. *Nature*, 1980. **288**(5790): p. 455-9.
89. Casella, J.F., D.J. Maack, and S. Lin, *Purification and initial characterization of a protein from skeletal muscle that caps the barbed ends of actin filaments*. *J Biol Chem*, 1986. **261**(23): p. 10915-21.
90. Cooper, J.A. and D. Sept, *New insights into mechanism and regulation of actin capping protein*. *Int Rev Cell Mol Biol*, 2008. **267**: p. 183-206.
91. Hart, M.C., Y.O. Korshunova, and J.A. Cooper, *Vertebrates have conserved capping protein alpha isoforms with specific expression patterns*. *Cell Motil Cytoskeleton*, 1997. **38**(2): p. 120-32.
92. Schafer, D.A., et al., *Differential localization and sequence analysis of capping protein beta-subunit isoforms of vertebrates*. *J Cell Biol*, 1994. **127**(2): p. 453-65.
93. Caldwell, J.E., et al., *Effects of CapZ, an actin capping protein of muscle, on the polymerization of actin*. *Biochemistry*, 1989. **28**(21): p. 8506-14.
94. Kim, T., J.A. Cooper, and D. Sept, *The interaction of capping protein with the barbed end of the actin filament*. *J Mol Biol*, 2010. **404**(5): p. 794-802.
95. Wear, M.A., et al., *How capping protein binds the barbed end of the actin filament*. *Curr Biol*, 2003. **13**(17): p. 1531-7.
96. Ydenberg, C.A., et al., *Cease-fire at the leading edge: new perspectives on actin filament branching, debranching, and cross-linking*. *Cytoskeleton (Hoboken)*, 2011. **68**(11): p. 596-602.
97. Lai, F.P., et al., *Arp2/3 complex interactions and actin network turnover in lamellipodia*. *EMBO J*, 2008. **27**(7): p. 982-92.
98. Pollard, T.D. and G.G. Borisy, *Cellular motility driven by assembly and disassembly of actin filaments*. *Cell*, 2003. **112**(4): p. 453-65.
99. Schafer, D.A., J.A. Waddle, and J.A. Cooper, *Localization of CapZ during myofibrillogenesis in cultured chicken muscle*. *Cell Motil Cytoskeleton*, 1993. **25**(4): p. 317-35.
100. Yamashita, A., K. Maeda, and Y. Maéda, *Crystal structure of CapZ: structural basis for actin filament barbed end capping*. *EMBO J*, 2003. **22**(7): p. 1529-38.
101. Edwards, M., et al., *Capping protein regulators fine-tune actin assembly dynamics*. *Nat Rev Mol Cell Biol*, 2014. **15**(10): p. 677-89.
102. Edwards, M., et al., *CPI motif interaction is necessary for capping protein function in cells*. *Nat Commun*, 2015. **6**: p. 8415.
103. Bhattacharya, N., et al., *Binding of myotrophin/V-1 to actin-capping protein: implications for how capping protein binds to the filament barbed end*. *J Biol Chem*, 2006. **281**(41): p. 31021-30.
104. Taoka, M., et al., *V-1, a protein expressed transiently during murine cerebellar development, regulates actin polymerization via interaction with capping protein*. *J Biol Chem*, 2003. **278**(8): p. 5864-70.

105. Heiss, S.G. and J.A. Cooper, *Regulation of CapZ, an actin capping protein of chicken muscle, by anionic phospholipids*. *Biochemistry*, 1991. **30**(36): p. 8753-8.
106. Kim, K., et al., *Structure/function analysis of the interaction of phosphatidylinositol 4,5-bisphosphate with actin-capping protein: implications for how capping protein binds the actin filament*. *J Biol Chem*, 2007. **282**(8): p. 5871-9.
107. Narita, A., et al., *Structural basis of actin filament capping at the barbed-end: a cryo-electron microscopy study*. *EMBO J*, 2006. **25**(23): p. 5626-33.
108. Funk, J., et al., *A barbed end interference mechanism reveals how capping protein promotes nucleation in branched actin networks*. *Nat Commun*, 2021. **12**(1): p. 5329.
109. Taoka, M., et al., *Murine cerebellar neurons express a novel gene encoding a protein related to cell cycle control and cell fate determination proteins*. *J Biol Chem*, 1994. **269**(13): p. 9946-51.
110. Zwolak, A., et al., *Structural basis for capping protein sequestration by myotrophin (V-1)*. *J Biol Chem*, 2010. **285**(33): p. 25767-81.
111. Takeda, S., et al., *Two distinct mechanisms for actin capping protein regulation--steric and allosteric inhibition*. *PLoS Biol*, 2010. **8**(7): p. e1000416.
112. Yang, C., et al., *Mammalian CARMIL inhibits actin filament capping by capping protein*. *Dev Cell*, 2005. **9**(2): p. 209-21.
113. Canton, D.A., et al., *The pleckstrin homology domain-containing protein CKIP-1 is involved in regulation of cell morphology and the actin cytoskeleton and interaction with actin capping protein*. *Mol Cell Biol*, 2005. **25**(9): p. 3519-34.
114. Bruck, S., et al., *Identification of a novel inhibitory actin-capping protein binding motif in CD2-associated protein*. *J Biol Chem*, 2006. **281**(28): p. 19196-203.
115. Uruno, T., K. Remmert, and J.A. Hammer, *CARMIL is a potent capping protein antagonist: identification of a conserved CARMIL domain that inhibits the activity of capping protein and uncaps capped actin filaments*. *J Biol Chem*, 2006. **281**(15): p. 10635-50.
116. Hernandez-Valladares, M., et al., *Structural characterization of a capping protein interaction motif defines a family of actin filament regulators*. *Nat Struct Mol Biol*, 2010. **17**(4): p. 497-503.
117. Johnson, B., et al., *Allosteric Coupling of CARMIL and V-1 Binding to Capping Protein Revealed by Hydrogen-Deuterium Exchange*. *Cell Rep*, 2018. **23**(9): p. 2795-2804.
118. Takeda, S., et al., *Structural Insights into the Regulation of Actin Capping Protein by Twinfilin C-terminal Tail*. *J Mol Biol*, 2021. **433**(9): p. 166891.
119. Stark, B.C., M.H. Lanier, and J.A. Cooper, *CARMIL family proteins as multidomain regulators of actin-based motility*. *Mol Biol Cell*, 2017. **28**(13): p. 1713-1723.
120. Zhao, J., et al., *CD2AP links cortactin and capping protein at the cell periphery to facilitate formation of lamellipodia*. *Mol Cell Biol*, 2013. **33**(1): p. 38-47.
121. McConnell, P., et al., *Comparative Analysis of CPI-Motif Regulation of Biochemical Functions of Actin Capping Protein*. *Biochemistry*, 2020. **59**(11): p. 1202-1215.
122. Fujiwara, I., et al., *Capping protein regulatory cycle driven by CARMIL and V-1 may promote actin network assembly at protruding edges*. *Proc Natl Acad Sci U S A*, 2014. **111**(19): p. E1970-9.
123. Palmgren, S., et al., *Interactions with PIP2, ADP-actin monomers, and capping protein regulate the activity and localization of yeast twinfilin*. *J Cell Biol*, 2001. **155**(2): p. 251-60.
124. Falck, S., et al., *Biological role and structural mechanism of twinfilin-capping protein interaction*. *EMBO J*, 2004. **23**(15): p. 3010-9.
125. Hilton, D.M., et al., *Species-Specific Functions of Twinfilin in Actin Filament Depolymerization*. *J Mol Biol*, 2018. **430**(18 Pt B): p. 3323-3336.

126. Johnston, A.B., et al., *A novel mode of capping protein-regulation by twinfilin*. *Elife*, 2018. **7**.
127. Hakala, M., et al., *Twinfilin uncaps filament barbed ends to promote turnover of lamellipodial actin networks*. *Nat Cell Biol*, 2021. **23**(2): p. 147-159.
128. Amatruda, J.F., et al., *Effects of null mutations and overexpression of capping protein on morphogenesis, actin distribution and polarized secretion in yeast*. *J Cell Biol*, 1992. **119**(5): p. 1151-62.
129. Kim, K., et al., *Capping protein binding to actin in yeast: biochemical mechanism and physiological relevance*. *J Cell Biol*, 2004. **164**(4): p. 567-80.
130. Lamb, A.K., et al., *The dynein light chain protein Tda2 functions as a dimerization engine to regulate actin capping protein during endocytosis*. *Mol Biol Cell*, 2021. **32**(16): p. 1459-1473.
131. Lamb, A.K. and S.M. Di Pietro, *Utilizing chemically induced dimerization of FKBP to analyze endocytosis by live-cell imaging in budding yeast*. *STAR protocols*, 2022. **3**(2): p. 101323.
132. Boettner, D.R., R.J. Chi, and S.K. Lemmon, *Lessons from yeast for clathrin-mediated endocytosis*. *Nat Cell Biol*, 2011. **14**(1): p. 2-10.
133. McMahon, H.T. and E. Boucrot, *Molecular mechanism and physiological functions of clathrin-mediated endocytosis*. *Nat Rev Mol Cell Biol*, 2011. **12**(8): p. 517-33.
134. Doyon, J.B., et al., *Rapid and efficient clathrin-mediated endocytosis revealed in genome-edited mammalian cells*. *Nat Cell Biol*, 2011. **13**(3): p. 331-7.
135. Idrissi, F.Z., et al., *Ultrastructural dynamics of proteins involved in endocytic budding*. *Proc Natl Acad Sci U S A*, 2012. **109**(39): p. E2587-94.
136. Kukulski, W., et al., *Plasma membrane reshaping during endocytosis is revealed by time-resolved electron tomography*. *Cell*, 2012. **150**(3): p. 508-20.
137. Avinoam, O., et al., *ENDOCYTOSIS. Endocytic sites mature by continuous bending and remodeling of the clathrin coat*. *Science*, 2015. **348**(6241): p. 1369-72.
138. Newpher, T.M., et al., *In vivo dynamics of clathrin and its adaptor-dependent recruitment to the actin-based endocytic machinery in yeast*. *Dev Cell*, 2005. **9**(1): p. 87-98.
139. Weinberg, J. and D.G. Drubin, *Clathrin-mediated endocytosis in budding yeast*. *Trends Cell Biol*, 2012. **22**(1): p. 1-13.
140. Mooren, O.L., B.J. Galletta, and J.A. Cooper, *Roles for actin assembly in endocytosis*. *Annu Rev Biochem*, 2012. **81**: p. 661-86.
141. Edwards, M., et al., *Physiological role of the interaction between CARMIL1 and capping protein*. *Mol Biol Cell*, 2013. **24**(19): p. 3047-55.
142. Rapali, P., et al., *DYNLL/LC8: a light chain subunit of the dynein motor complex and beyond*. *FEBS J*, 2011. **278**(17): p. 2980-96.
143. Chuang, J.Z., et al., *The dynein light chain Tctex-1 has a dynein-independent role in actin remodeling during neurite outgrowth*. *Dev Cell*, 2005. **9**(1): p. 75-86.
144. Yeh, T.Y., et al., *Regulatory dissociation of Tctex-1 light chain from dynein complex is essential for the apical delivery of rhodopsin*. *Traffic*, 2006. **7**(11): p. 1495-502.
145. Conde, C., et al., *Evidence for the involvement of Lfc and Tctex-1 in axon formation*. *J Neurosci*, 2010. **30**(19): p. 6793-800.
146. Jespersen, N. and E. Barbar, *Emerging Features of Linear Motif-Binding Hub Proteins*. *Trends Biochem Sci*, 2020. **45**(5): p. 375-384.
147. Clark, S.A., et al., *Multivalent IDP assemblies: Unique properties of LC8-associated, IDP duplex scaffolds*. *FEBS Lett*, 2015. **589**(19 Pt A): p. 2543-51.
148. Williams, J.C., H. Xie, and W.A. Hendrickson, *Crystal structure of dynein light chain TcTex-1*. *J Biol Chem*, 2005. **280**(23): p. 21981-6.

149. Williams, J.C., et al., *Structural and thermodynamic characterization of a cytoplasmic dynein light chain-intermediate chain complex*. Proc Natl Acad Sci U S A, 2007. **104**(24): p. 10028-33.
150. Benison, G. and E. Barbar, *NMR analysis of dynein light chain dimerization and interactions with diverse ligands*. Methods Enzymol, 2009. **455**: p. 237-58.
151. Hall, J., P.A. Karplus, and E. Barbar, *Multivalency in the assembly of intrinsically disordered Dynein intermediate chain*. J Biol Chem, 2009. **284**(48): p. 33115-21.
152. Neff, T., et al., *Pharmacologically regulated in vivo selection in a large animal*. Blood, 2002. **100**(6): p. 2026-31.
153. Clackson, T., et al., *Redesigning an FKBP-ligand interface to generate chemical dimerizers with novel specificity*. Proc Natl Acad Sci U S A, 1998. **95**(18): p. 10437-42.
154. Kolos, J.M., et al., *FKBP Ligands-Where We Are and Where to Go?* Front Pharmacol, 2018. **9**: p. 1425.
155. Mionnet, C., S. Bogliolo, and R.A. Arkowitz, *Oligomerization regulates the localization of Cdc24, the Cdc42 activator in Saccharomyces cerevisiae*. J Biol Chem, 2008. **283**(25): p. 17515-30.
156. Merino-Gracia, J., et al., *DYNLT (Tctex-1) forms a tripartite complex with dynein intermediate chain and RagA, hence linking this small GTPase to the dynein motor*. FEBS J, 2015. **282**(20): p. 3945-58.
157. Mwangangi, D.M., E. Manser, and R.C. Robinson, *The structure of the actin filament uncapping complex mediated by twinfilin*. Sci Adv, 2021. **7**(5).
158. Shekhar, S., et al., *Twinfilin bypasses assembly conditions and actin filament aging to drive barbed end depolymerization*. J Cell Biol, 2021. **220**(1).
159. Di Pietro, S.M., et al., *Regulation of clathrin adaptor function in endocytosis: novel role for the SAM domain*. EMBO J, 2010. **29**(6): p. 1033-44.
160. Sikorski, R.S. and P. Hieter, *A system of shuttle vectors and yeast host strains designed for efficient manipulation of DNA in Saccharomyces cerevisiae*. Genetics, 1989. **122**(1): p. 19-27.
161. Ito, H., et al., *Transformation of intact yeast cells treated with alkali cations*. J Bacteriol, 1983. **153**(1): p. 163-8.
162. Feliciano, D. and S.M. Di Pietro, *SLAC, a complex between Sla1 and Las17, regulates actin polymerization during clathrin-mediated endocytosis*. Mol Biol Cell, 2012. **23**(21): p. 4256-72.
163. Bultema, J.J., et al., *Myosin vc interacts with Rab32 and Rab38 proteins and works in the biogenesis and secretion of melanosomes*. J Biol Chem, 2014. **289**(48): p. 33513-28.
164. Tolsma, T.O., L.M. Cuevas, and S.M. Di Pietro, *The Sla1 adaptor-clathrin interaction regulates coat formation and progression of endocytosis*. Traffic, 2018. **19**(6): p. 446-462.
165. Doherty, G.J. and H.T. McMahon, *Mechanisms of endocytosis*. Annu Rev Biochem, 2009. **78**: p. 857-902.
166. Cooper, J.A. and D.A. Schafer, *Control of actin assembly and disassembly at filament ends*. Curr Opin Cell Biol, 2000. **12**(1): p. 97-103.
167. Carlier, M.F. and D. Pantaloni, *Control of actin dynamics in cell motility*. J Mol Biol, 1997. **269**(4): p. 459-67.
168. Berro, J., V. Sirotkin, and T.D. Pollard, *Mathematical modeling of endocytic actin patch kinetics in fission yeast: disassembly requires release of actin filament fragments*. Mol Biol Cell, 2010. **21**(16): p. 2905-15.
169. Lappalainen, P., et al., *The ADF homology (ADF-H) domain: a highly exploited actin-binding module*. Mol Biol Cell, 1998. **9**(8): p. 1951-9.
170. Maciver, S.K. and P.J. Hussey, *The ADF/cofilin family: actin-remodeling proteins*. Genome Biol, 2002. **3**(5): p. reviews3007.

171. Vartiainen, M., et al., *Mouse A6/twinfilin is an actin monomer-binding protein that localizes to the regions of rapid actin dynamics*. Mol Cell Biol, 2000. **20**(5): p. 1772-83.
172. Ojala, P.J., et al., *The two ADF-H domains of twinfilin play functionally distinct roles in interactions with actin monomers*. Mol Biol Cell, 2002. **13**(11): p. 3811-21.
173. Helfer, E., et al., *Mammalian twinfilin sequesters ADP-G-actin and caps filament barbed ends: implications in motility*. EMBO J, 2006. **25**(6): p. 1184-95.
174. Paavilainen, V.O., et al., *Structural basis and evolutionary origin of actin filament capping by twinfilin*. Proc Natl Acad Sci U S A, 2007. **104**(9): p. 3113-8.
175. Johnston, A.B., A. Collins, and B.L. Goode, *High-speed depolymerization at actin filament ends jointly catalysed by Twinfilin and Srv2/CAP*. Nat Cell Biol, 2015. **17**(11): p. 1504-11.
176. Singer-Krüger, B., et al., *Synaptojanin family members are implicated in endocytic membrane traffic in yeast*. J Cell Sci, 1998. **111 ( Pt 22)**: p. 3347-56.
177. Sun, Y., et al., *PtdIns(4,5)P2 turnover is required for multiple stages during clathrin- and actin-dependent endocytic internalization*. J Cell Biol, 2007. **177**(2): p. 355-67.
178. Kurochkina, N. and U. Guha, *SH3 domains: modules of protein-protein interactions*. Biophys Rev, 2013. **5**(1): p. 29-39.
179. Doolittle, L.K., M.K. Rosen, and S.B. Padrick, *Measurement and analysis of in vitro actin polymerization*. Methods Mol Biol, 2013. **1046**: p. 273-93.